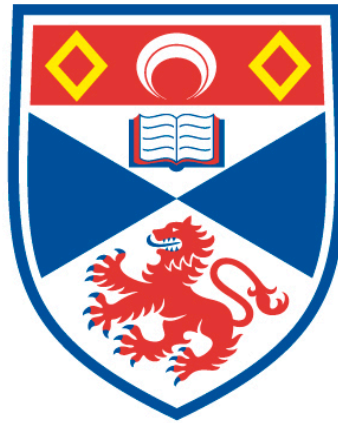


A COMPUTATIONAL INVESTIGATION OF OXYGEN STORAGE
AND MIGRATION IN ENERGY MATERIALS

Gregor David McInnes

A Thesis Submitted for the Degree of PhD
at the
University of St Andrews



2018

Full metadata for this item is available in
St Andrews Research Repository
at:
<http://research-repository.st-andrews.ac.uk/>

Identifiers to use to cite or link to this thesis:
DOI: <https://doi.org/10.17630/10023-16578>
<http://hdl.handle.net/10023/16578>

This item is protected by original copyright

A Computational Investigation of Oxygen Storage and Migration in Energy Materials

Gregor David McInnes



University of
St Andrews

This thesis is submitted in partial fulfilment for the degree of PhD
at the
University of St Andrews

26 September 2017

1. Candidate’s declarations:

I, Gregor David McInnes, hereby certify that this thesis, which is approximately 24,000 words in length, has been written by me, and that it is the record of work carried out by me, or principally by myself in collaboration with others as acknowledged, and that it has not been submitted in any previous application for a higher degree.

I was admitted as a research student in September 2013 and as a candidate for the degree of Doctor of Philosophy. in September 2013; the higher study for which this is a record was carried out in the University of St Andrews between 2013 and 2017.

Date signature of candidate

2. Supervisor’s declaration:

I hereby certify that the candidate has fulfilled the conditions of the Resolution and Regulations appropriate for the degree of Doctor of Philosophy in the University of St Andrews and that the candidate is qualified to submit this thesis in application for that degree.

Date signature of supervisor

3. Permission for publication: (to be signed by both candidate and supervisor)

In submitting this thesis to the University of St Andrews I understand that I am giving permission for it to be made available for use in accordance with the regulations of the University Library for the time being in force, subject to any copyright vested in the work not being affected thereby. I also understand that the title and the abstract will be published, and that a copy of the work may be made and supplied to any bona fide library or research worker, that my thesis will be electronically accessible for personal or research use unless exempt by award of an embargo as requested below, and that the library has the right to migrate my thesis into new electronic forms as required to ensure continued access to the thesis. I have obtained any third-party copyright permissions that may be required in order to allow such access and migration, or have requested the appropriate embargo below.

The following is an agreed request by candidate and supervisor regarding the publication of this thesis:

PRINTED COPY

- a) Embargo on all or part of print copy for a period of 1 years (maximum five) on the following ground(s):
 - Publication would preclude future publication

ELECTRONIC COPY

- a) Embargo on all or part of electronic copy for a period of 1 years (maximum five) on the following ground(s):
- Publication would preclude future publication:

ABSTRACT AND TITLE EMBARGOES

An embargo on the full text copy of your thesis in the electronic and printed formats will be granted automatically in the first instance. This embargo includes the abstract and title except that the title will be used in the graduation booklet.

If you have selected an embargo option indicate below if you wish to allow the thesis abstract and/or title to be published. If you do not complete the section below the title and abstract will remain embargoed along with the text of the thesis.

- | | |
|--|--------|
| a) I agree to the title and abstract being published | YES/NO |
| b) I require an embargo on abstract | YES/NO |
| c) I require an embargo on title | YES/NO |

Date signature of candidate

signature of supervisor

Please note initial embargos can be requested for a maximum of five years. An embargo on a thesis submitted to the Faculty of Science or Medicine is rarely granted for more than two years in the first instance, without good justification. The Library will not lift an embargo before confirming with the student and supervisor that they do not intend to request a continuation. In the absence of an agreed response from both student and supervisor, the Head of School will be consulted. Please note that the total period of an embargo, including any continuation, is not expected to exceed ten years.

Where part of a thesis is to be embargoed, please specify the part and the reason.

Abstract

This thesis describes a computational investigation into the oxygen storage material copper doped ceria and electrolyte material $\text{Ge}_5\text{O}(\text{PO}_4)_6$ for use in Solid Oxide Fuel Cells.

In Chapter 1, a background on fuel cells is given along with explanations and examples of different oxygen migration mechanisms. After this, a background on the materials $\text{Ge}_5\text{O}(\text{PO}_4)_6$ and copper doped ceria is given.

Chapter 2 presents background on the computational techniques used. This includes discussion of first principles techniques and an explanation of the CALPHAD method.

Chapter 3 presents the detailed results of the investigation into copper doped ceria. This investigation concentrated on the stability of copper ceria as well as on the ionic makeup of the material. The main findings of this investigation are that Cu^{1+} and Cu^{2+} ions can be doped into ceria with the maximum doping reaching 0.09 mole fraction Cu.

In Chapter 4 the details of the computation investigation into $\text{Ge}_5\text{O}(\text{PO}_4)_6$ are given. This investigation looked at the possible oxygen migration pathways. From the findings of this investigation we were able to rule out several different possible pathways through the structure.

Chapter 5 gives a brief overview of the findings of each of the projects and provides recommendations on future work that may be carried out on each of the systems.

Appendix A provides supplementary data on the copper doped ceria project, specifically the coding of the thermodynamic database created during the project.

Abbreviations

BET	Brunauer–Emmett–Teller
CALPHAD	Calculation of Phase Diagrams
CEF	Compound energy Formalism
CI-NEB	Climbing Image Nudged Elastic Band
DFPT	Density Functional Perturbation Theory
DFT	Density Functional Theory
HF	Hartree-Fock
HSE	Heyd Scuseria Ernzerhof
NEB	Nudged Elastic Band
NPD	Neutron Powder Diffraction
PBE	Perdue Burke Ernzerhof
OSC	Oxygen Storage Capacity
SOFC	Solid Oxide Fuel Cell
VASP	Vienna Ab initio Simulation Package
XPS	X-ray Photoelectron Spectroscopy
XRD	X-ray Diffraction
YSZ	Yttria – stabilised zirconia

Contents:

Chapter 1: Introduction.....	1
1.1. Background on Fuel Cells.....	1
1.1.1. Fuel Cell Types.....	2
1.1.2. Solid Oxide Fuel Cells.....	4
1.2. Background on Electrolyte Materials.....	4
1.2.1. Solid State Electrolytes.....	5
1.2.2. Conduction Mechanisms.....	6
1.2.3. Oxygen Ion Conductors.....	7
1.2.4. Vacancy Mechanism Ion Conductors.....	8
1.2.5. Interstitial Ion Conductors.....	10
1.2.5.1. Lanthanide silicate.....	10
1.3. The $\text{Ge}_5\text{O}(\text{PO}_4)_6$ Structure.....	13
1.4. Aim of research Project.....	18
1.5. Background on Oxygen Storage Materials.....	19
1.5.1. Uses of Oxygen Storage Materials.....	19
1.5.2. Cerium Oxide.....	19
Chapter 2: Computational Methods.....	27
2.1. First Principles Calculations.....	27
2.1.1. Basic Concepts.....	27
2.1.2. The Born-Oppenheimer Approximations.....	29

2.1.3. Hartree-Fock Method	30
2.1.4. Post Hartree-Fock Methods	33
2.1.5. Density Functional Theory	33
2.1.5.1. Hohenberg-Kohn Theory	34
2.1.5.2. Kohn-Sham Method	35
2.1.5.3. Local Density Approximation	37
2.1.5.4. Generalised Gradient Approximation	37
2.1.5.5. The +U Correction	38
2.1.5.6. Hybrid Functionals	39
2.1.5.7. Dispersion Correction	39
2.1.5.8. Reciprocal Space	40
2.1.5.9. Basis Sets	40
2.1.5.10. Plane Wave Basis Sets	40
2.1.5.11. Pseudopotentials	41
2.1.6. Geometry Optimization	42
2.1.7. Nudged Elastic Band	43
2.1.8. Phonon Calculations	45
2.2. CALPHAD	47
Chapter 3 – Investigation of the Thermodynamic Properties of Copper Doped Ceria	52
3.1. Aim	52
3.2. Creation of Starting Thermodynamic Database	52

3.3. Thermodynamic Modelling of the Copper Doped Ceria Phase	54
3.4. Cation and Vacancy Modelling of the Copper Doped Ceria Phase using reciprocal Relations	56
3.5. Test Calculations	58
3.6. Calculations Relating to Neutral Structures	62
3.7. Calculations Relating to Mixing Enthalpies.....	66
3.8. Other Sources of Thermodynamic Information	68
3.9. Optimization of the Thermodynamic Parameters of the Copper Doped Ceria Phase	70
3.10. Optimization of the Thermodynamic Parameters of the Ceria Doped Copper Oxide Phases.....	74
3.11. Phase Diagrams of the Ce-Cu-O System	75
3.12. Site Fraction Study	77
Chapter 4 - Investigation of Oxygen Migration Mechanisms in $\text{Ge}_5\text{O}(\text{PO}_4)_6$	85
4.1. Aim.....	85
4.2. Experimental activation energies and relationship between $\text{Ge}_5\text{O}(\text{PO}_4)_6$ and Si based alternative structure.....	85
4.3. Method.....	88
4.4. Test Calculations	89
4.5. Investigation of possible mechanisms within $\text{Ge}_5\text{O}(\text{PO}_4)_6$	92
2.5.1. Rotation of Tetrahedron.....	92
2.5.2. Vacancy Mechanisms.....	95

2.5.2.1. Movement O1 to O4	95
2.5.2.2. Movement O4 to O3	98
2.5.2.3. Movement O3 to O3	100
2.5.2.4. Movement O4 to O5	102
2.5.2.5. Movement O2 to O3	104
2.5.2.6. Lowest Energy Full Movement	106
2.5.3. Interstitialcy Mechanism.....	108
4.6. Investigation of Mechanism within Structure II.....	110
2.6.1. Rotation of Tetrahedron.....	110
2.6.2. Vacancy Mechanism	111
2.6.2.1. Movement O1 to O4	112
2.6.2.2. Movement O4 to O3	114
2.6.2.3. Movement O3 to O3	115
2.6.2.4. Movement O4 to O5	118
2.6.2.5. Movement O2 to O3	119
2.6.2.6. Lowest Energy Full Movement	121
2.6.2.7. Interstitialcy Mechanism	122
2.6.3. Conclusion	124
Chapter 5 – Conclusions and Future Work.....	125
References	129
Appendix A: Thermodynamic database of the Ce-Cu-O system.....	136

Appendix B: Optimized unit cell information	153
---	-----

Chapter 1: Introduction

This thesis is concerned with the study of oxygen storage and electrolyte materials for Solid Oxide Fuel Cells (SOFCs). In particular we will investigate the ionic conducting properties of the electrolyte material $\text{Ge}_5\text{O}(\text{PO}_4)_6$ and related materials and investigate general properties of the oxygen storage material copper doped ceria for use as a cathode.

1.1. Background on Fuel Cells

Fuel Cells are devices by which chemical energy can be converted into electrical power. They contain a similar structure to a regular battery, having an anode and cathode that are connected to each other by an electrolyte and by an external circuit but, unlike in a battery which relies on the reaction of chemicals already contained within it, the fuel cell requires a constant source of fuel and oxygen from an external source in order to drive a reaction. Fuel Cell technology was first shown in a primitive cell design in 1839 by W. R. Grove¹ but was not developed further at the time due to material and economic factors.

Fuel Cells are now being developed further with the aim that they will provide a greener method of energy conversion, for example in the automotive industry as a replacement for the internal combustion engine.

1.1.1. Fuel Cell Types

Several different Fuel Cell types exist with each type using the same main components (Anode, Cathode and Electrolyte) but differ in several respects to allow them to run at different temperatures and with different sources of fuel.

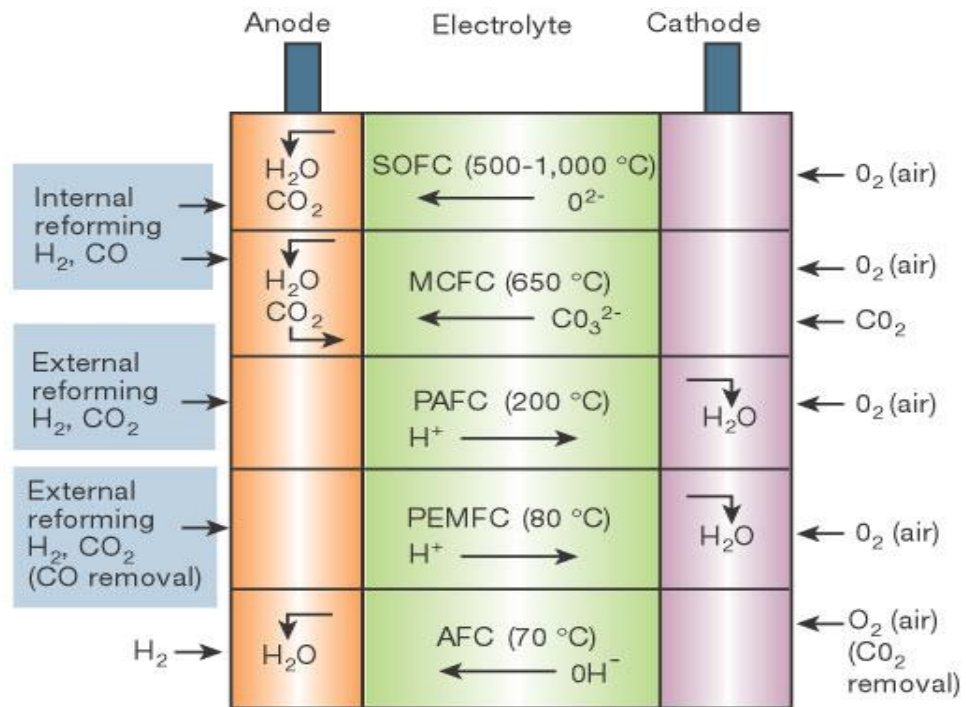


Figure 1. Diagram of the different types of fuel cells in development. Adapted from Steele and Heinzl (Nature, 2001)²

The Alkaline Fuel Cell (AFC) uses an alkaline liquid as an electrolyte which transports oxygen from the cathode to the anode in the form of an hydroxyl ion, it then reacts with hydrogen to produce water and an electron supply for the external circuit. The AFC does suffer drawbacks in that even though it is cheap, the produced cells are poisoned by CO₂, which requires their oxygen supply to be scrubbed which removes any CO₂ from the oxygen supply by flowing the oxygen through a solution or a material to which CO₂ will bind.

The Proton Exchange Membrane Fuel Cell (PEMFC) uses a solid state electrolyte which acts as a selective membrane. Hydrogen molecules are catalytically split at the anode and hydrogen ions pass through the electrolyte to the cathode where they react with the oxygen supply to form water. This type of Fuel Cell can only use hydrogen as a fuel source.

The Phosphoric Acid Fuel Cell (PAFC) was the first fuel cell type to be commercialised and uses phosphoric acid as an electrolyte. Like in the PEMFC the hydrogen is split at the anode and crosses the electrolyte to the cathode. Compared to the PEMFC, the PAFC is more CO₂ tolerant and can use a broader range of fuels. At operating temperatures the expelled water can be converted to steam for air and water heating, increasing the cell's efficiency.

The Molten Carbonate Fuel Cell (MCFC) uses an electrolyte composed of a molten carbonate salt mixture suspended in a porous, chemically inert ceramic matrix of beta-alumina solid electrolyte (BASE). It operates at high temperatures (650°C and above), meaning that non-precious metals can be used as catalysts at the anode and cathode. Due to its high operating temperatures it can convert fuel into hydrogen internally, which means that no external reformation step is necessary.

The final fuel cell type is the Solid Oxide Fuel Cell (SOFC), and this is the fuel cell of interest within this thesis.

1.1.2. Solid Oxide Fuel Cells

The Solid Oxide Fuel Cell or SOFC is a high operating temperature fuel cell operating at temperatures between 500-1000 °C. This allows the fuel cell to use an internal fuel reformer which makes it possible to use impure fuels.

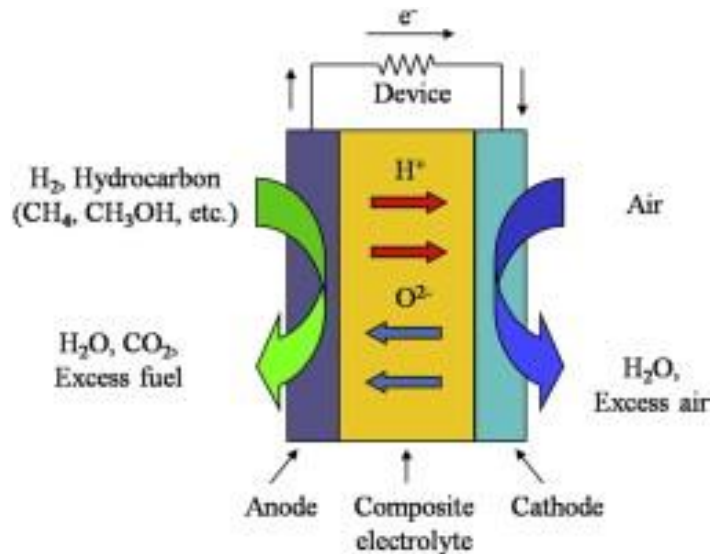


Figure 2. The overall composition of an SOFC showing input and output materials. Oxygen flows from the cathode to the anode. Figure taken from Y. Zhao et al.³

During this project two different materials will be assessed. The first material is $Ge_5O(PO_4)_6$ which is being considered as an electrolyte material. The second is copper doped CeO_2 which can be used in a cell as either an electrolyte material or as part of the cathode.

1.2. Background on Electrolyte Materials

As we are assessing the suitability of $Ge_5O(PO_4)_6$ as an electrolyte with focus on its conductivity pathway, it is necessary to provide a background on solid state electrolytes and conduction pathways.

1.2.1. Solid State Electrolytes

Solid state electrolytes are also known as fast ion conductors. This is because they can exhibit high ion conductivity ($>10^{-4} \text{ S cm}^{-1}$)⁴. This conductivity arises from the migration of ions through an ordered lattice structure. This movement of ions is usually facilitated via the use of intrinsic or extrinsic lattice defects. An explanation for the formation of intrinsic defects within a crystal structure may be derived from the Gibbs free energy equation (Equation 1.1)⁵.

$$\Delta G = \Delta H - T\Delta S \quad (1.1)$$

The equation shows that at low temperatures the Gibbs free energy is dominated by the enthalpy (H). However, when the temperature increases, entropy (S) starts to have a larger contribution to the energy. This increase in entropy signals the formation of crystallographic defects within the structure to minimise the free energy⁶. This may result in the formation of two types of point defects, known as the Schottky defect and the Frenkel defect. Schottky defects arise when charged ions/atoms leave the lattice, forming vacancies within the structure, while Frenkel defects are where an atom does not stay within a crystallographically defined point and instead resides with interstitial spaces between atoms⁴.

Extrinsic defects are the result on non-stoichiometric crystal compositions or the addition of a dopant. These defects can cause a range of interactions. For example, in yttria-stabilised zirconia (YSZ) vacancies are formed in the anionic lattice resulting in a high ionic conductivity.

The use of solid state electrolytes allows SOFCs to avoid problems relating to electrolyte creep where a short circuit is formed from one electrode to the other, through a liquid electrolyte via the formation of products on the surface of the electrodes. It also means that the cell is safer, as unlike in a liquid based design any cracks in the system will not cause the release of toxins into the atmosphere.

1.2.2. Conduction Mechanisms

There are three general types of conduction mechanisms that have been observed in the conduction of ions through crystal lattices. These are known as the vacancy, interstitial and interstitialcy mechanisms. Each mechanism type relies on different defect types⁶.

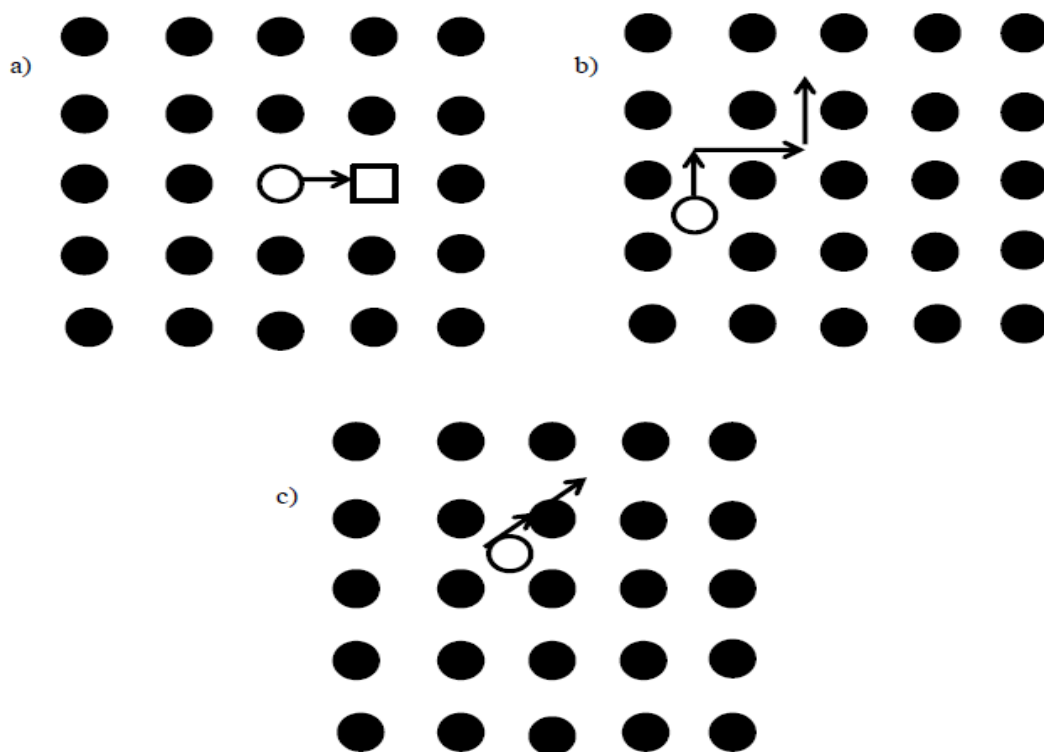


Figure 3. Schematic views of the different types of conductance mechanisms. Diagram a. shows the vacancy mechanism, diagram b. shows the interstitial mechanism and diagram c. shows the interstitialcy mechanism. Figure taken from M. Tham⁷

Figure 3a shows a vacancy type mechanism. In this mechanism type the movement of atoms through the crystal lattice occurs via the “hopping” of atoms into adjacent vacant sites. Figure 3b shows the interstitial mechanism. For this mechanism type, extra atoms need to be present within the interstitial spaces of the crystal structure. These atoms then move through this interstitial space. The third and final mechanism shown in figure 3c is known as the interstitialcy mechanism. In this mechanism type atom exchange occurs between the interstitial and lattice sites. This can also be referred to as the “knock on” mechanism⁸.

1.2.3. Oxygen Ion Conductors

Mobile Charge Carrier materials are a large subset of materials that have found many uses in the development of batteries and fuel cells. The materials we will be looking at within this thesis fall under a subcategory of these materials known as oxide ion conducting ceramic oxides. The ability of these materials to permit fast oxygen ion transport has led to them being used for a variety of functions within electrochemical cells such as separation membranes, catalysts, membranes for methane conversion to syngas, and as electrolytes^{2,9-11}.

These oxide ion conducting ceramic oxides normally offer one of the three conductance mechanisms mentioned above. As we are looking at the conductance mechanism of $\text{Ge}_5\text{O}(\text{PO}_4)_6$ we will review traditionally used oxide ion conductors, comparing examples that cover the vacancy and interstitial type mechanisms.

1.2.4. Vacancy Mechanism Ion Conductors

The most common type of structure for ion conductors is the Fluorite structure in which the ion conductor adopts the composition of AO_2 (A = tetravalent cation)^{12,13}. The most well-known of the fluorite structure conductors is acceptor doped Zirconia⁴. Zirconia normally adopts a cubic fluorite structure at 2400 °C, but when cooled it goes through phase transitions to tetragonal and monoclinic polymorphs. This phase transition can involve an expansion of the unit cell which compromises its integrity⁴.

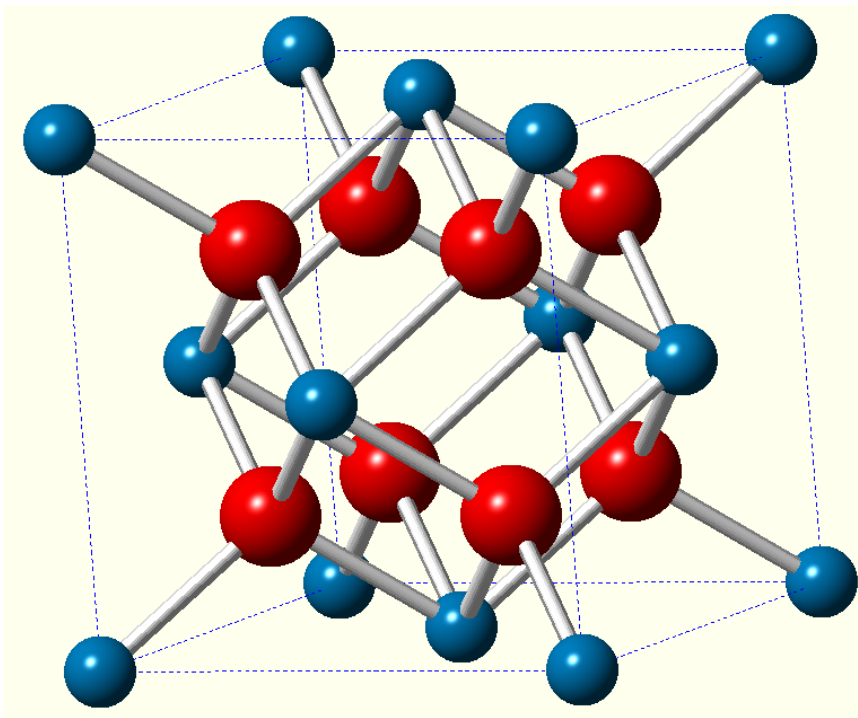


Figure 4. Diagram of the fluorite structure. The blue spheres are Zr^{4+} and the red spheres are oxygen.

In order to stabilise the structure, it is doped with aliovalent cations. Some of the most common are Ca^{2+} , Sc^{3+} and Y^{3+} .¹⁴ This doping provides significant benefits in comparison to pure ZrO_2 . The first benefit is that these dopants stop the phase transitions, stabilising the Fluorite structure at operating temperatures. The second

benefit is that extrinsic defects are formed in the oxygen lattice in order to maintain charge neutrality. These defects then allow oxygen migration via the vacancy mechanism¹⁵.

Many parameters that affect this mechanism have been studied by a range of sources. These parameters include the ionic radii and concentration of the dopant.

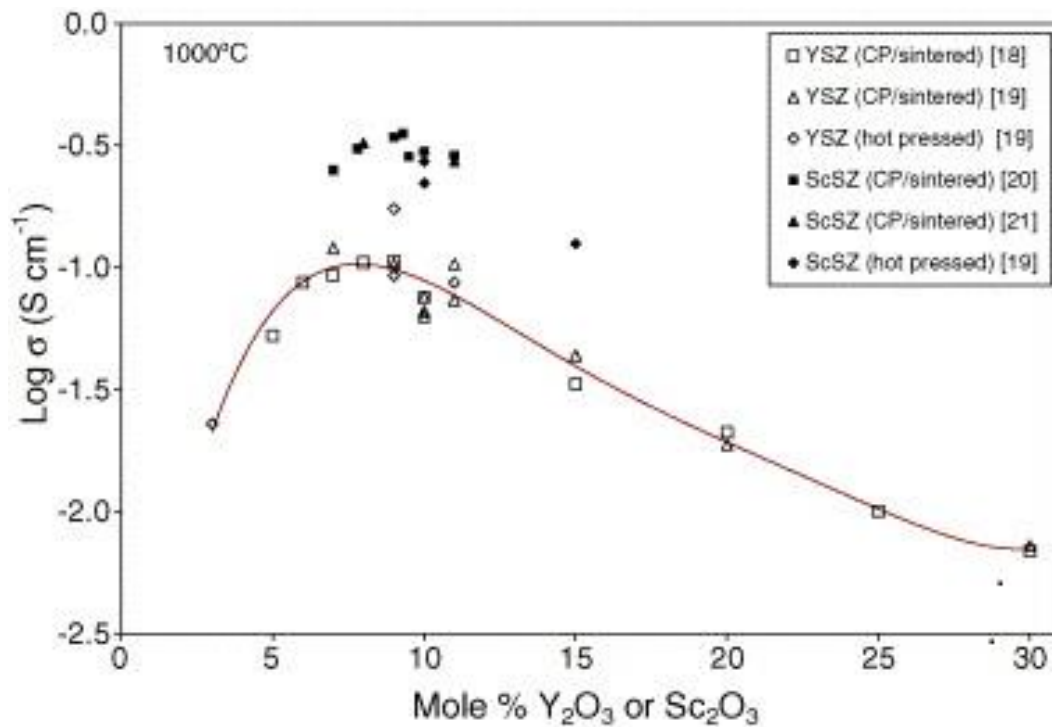


Figure 5. The effect of mol % dopant concentration on conductivity for yttria and scandia stabilised zirconia¹⁶.

Figure 5 shows the effect of dopant concentration on ionic conductivity¹⁶. It shows that with increasing amounts of dopant impurities the conductivity increases. This is due to the increasing number of vacancies in the oxygen sub-lattice. However this trend only holds up to 8% doping. Above mole 8% doping we instead see a degradation of the performance¹⁷ due to dopant- vacancy interactions¹⁸. The graph also shows the effect of ionic radii on the electrical conductance performance. We can see that ScSZ gives a

better performance than YSZ^{14,19}. This is because Sc³⁺ has a similar ionic radius to the host Zr⁴⁺ ions (0.84 Å and 0.87 Å respectively)^{14,20}. Having a larger ionic radius difference introduces elastic strain to the material which plays a large role in dopant-vacancy interaction²¹.

1.2.5. Interstitial Ion Conductors

1.2.5.1. Lanthanide silicate

The lanthanide silicate family of conductors have a structure that is a derivative of an apatite structure which has an ideal stoichiometric formula of A₁₀(BO₄)₆O₂. The apatite structure exists as a hexagonal unit cell with a space group of P63/m (shown in figure 6a). In the case of the lanthanide series, the unit cell consists of SiO₄ groups with La coordinating with oxygen to form both a 7 coordination structure and a 9 coordination structure (figure 6b and 6c respectively). As a result of this structure, channels of lanthanum and oxygen run along the C-axis.

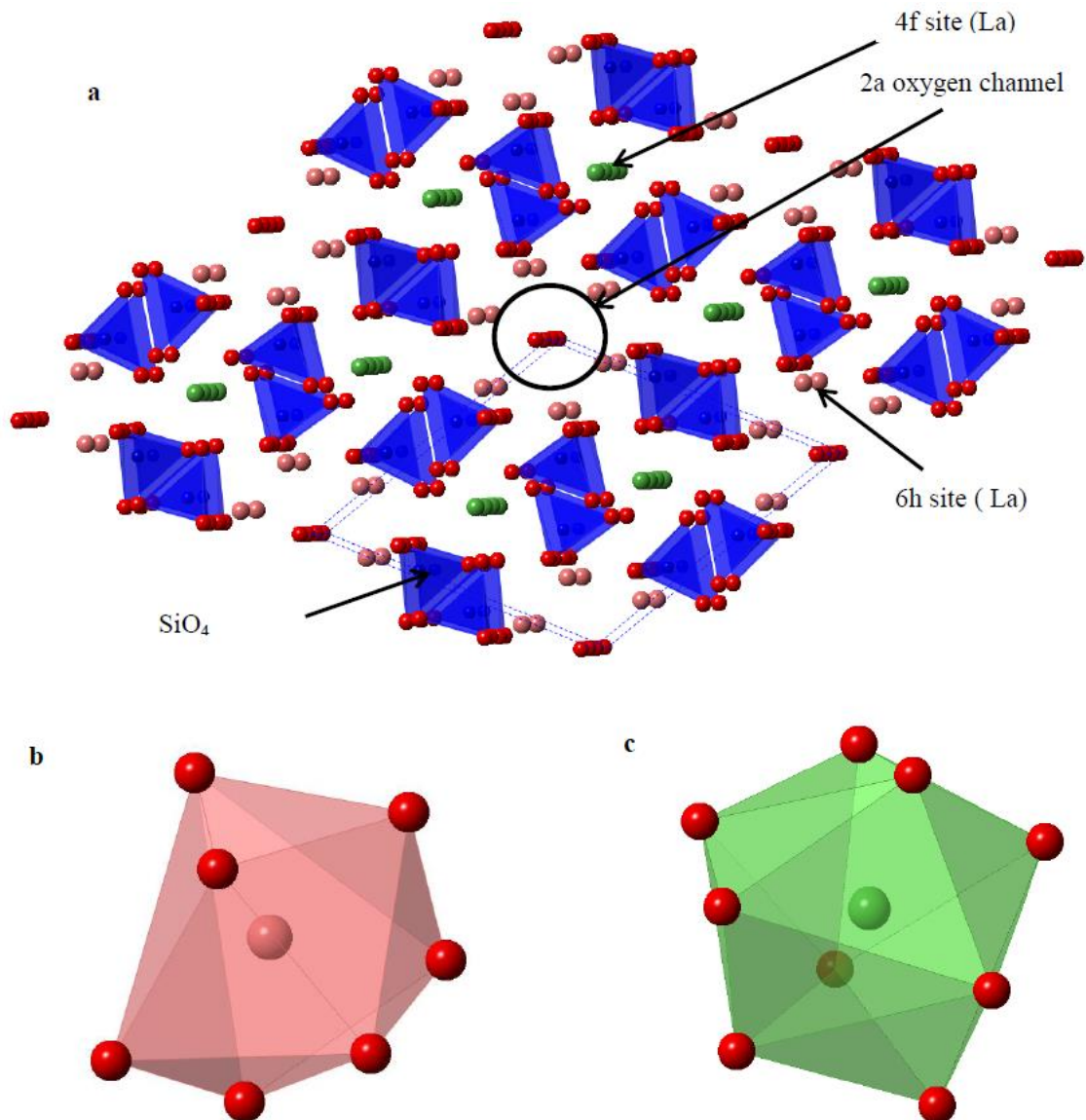


Figure 6. A schematic diagram of the crystal structure in $\text{La}_{10}(\text{SiO}_4)_6\text{O}_3$. Shown are the SiO_4 tetrahedra (blue), 7- coordinate La (pink), 9coordinate La (green) and oxygen (red).

The Lanthanide silicate series was studied by Nakayama et al.²² This study showed that this structure allowed for a high oxygen ion conductivity, with $\text{La}_{10}(\text{SiO}_4)_6\text{O}_3$ having the highest conductivity in the tested series. When compared to other common electrolytes such as $(\text{ZrO}_2)_{0.92}(\text{Y}_2\text{O}_3)_{0.08}$ and $(\text{Bi}_2\text{O}_3)_{0.75}(\text{Y}_2\text{O}_3)_{0.25}$ it was shown that the Lanthanide material had a higher conductivity at temperatures below 600 °C and 300 °C respectively.

Conductivity Mechanism

The conductivity mechanism of the apatite structure was investigated using two derivatives of $\text{La}_{10}(\text{SiO}_4)_6\text{O}_3$. The derivatives tested were $\text{La}_{9.33}(\text{SiO}_4)_6\text{O}_2$ and $\text{La}_8\text{Sr}_2(\text{SiO}_4)_6\text{O}_2$. The difference between the two derivatives is that $\text{La}_{9.33}(\text{SiO}_4)_6\text{O}_2$ is cation deficient while $\text{La}_8\text{Sr}_2(\text{SiO}_4)_6\text{O}_2$ is not. When tested it was found that the cation deficient derivative had a high oxygen ion conductivity ($\sigma = 1.2 \times 10^{-4} \text{ S cm}^{-1}$ at 700°C) while the non-deficient structure was a poor ion conductor ($\sigma = 2.9 \times 10^{-7} \text{ S cm}^{-1}$ at 700°C)²³. This indicated that structural changes between the two structures cause a change in conductivity. A neutron diffraction study by H. Sansom et al.²³ found that the cation vacancies were present at the 4F site (La) in $\text{La}_{9.33}(\text{SiO}_4)_6\text{O}_2$ and that an oxygen was missing from the 2a channel. The location of this oxygen was then confirmed via refinement of an oxygen ion site at 0, 0, 0.38 (fractional coordinates) which improved the model. Refinement of the non-deficient structure with a similar site led to no improvement. This suggested that disorder within the oxygen ion channel facilitated by lanthanum ion vacancies leads to the higher oxygen ion conductivity in $\text{La}_{9.33}(\text{SiO}_4)_6\text{O}_2$ ²⁴.

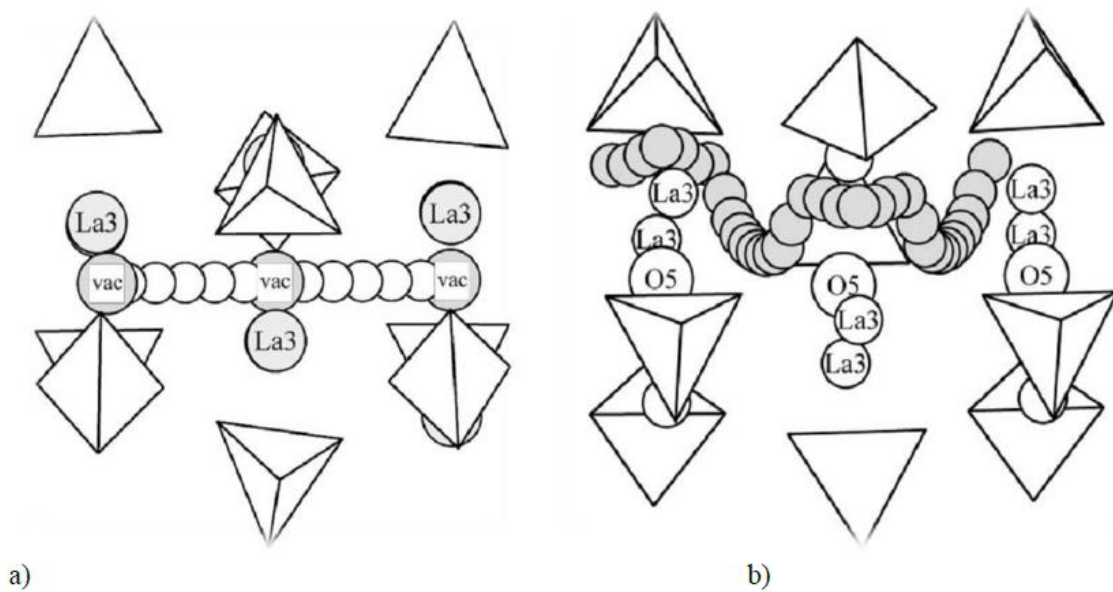


Figure 7. Ionic conduction in stoichiometric and non-stoichiometric lanthanum silicate²⁵ a) shows the vacancy mechanism of O5 along the O5 oxide channel. b) shows the interstitial mechanism that occurs perpendicular to the O5 oxide channel.

Atomistic simulations using the GULP package (with the shell model and Buckingham potentials being used.) by Islam et al²⁶ and Tolchard et al²⁵ show that the oxygen transport in $\text{La}_8\text{Sr}_2(\text{SiO}_4)_6\text{O}_2$ occurs through a vacancy mechanism. This is similar to other vacancy oxide ion conductors, except that the vacancy is within the 2a oxygen channel, so the conduction occurs anisotropically along the c-axis. However, the conductance mechanism in the more active $\text{La}_8\text{Sr}_2(\text{SiO}_4)_6\text{O}_2$ material occurs via an interstitial pathway involving oxygens that sit near the 2a oxygen channel and is facilitated by the displacement of the SiO_4 towards the (4f site) cation channels.

1.3. The $\text{Ge}_5\text{O}(\text{PO}_4)_6$ Structure

In this thesis we will be examining $\text{Ge}_5\text{O}(\text{PO}_4)_6$ to attempt to provide an atomistic model of its conduction pathway. The material was first synthesised by H. Mayer et al.

in the form of a single crystal²⁷ and was included in a $\text{GeO}_2\text{-P}_2\text{O}_5$ phase diagram produced by A.E.Mal'shikov et al.²⁸.

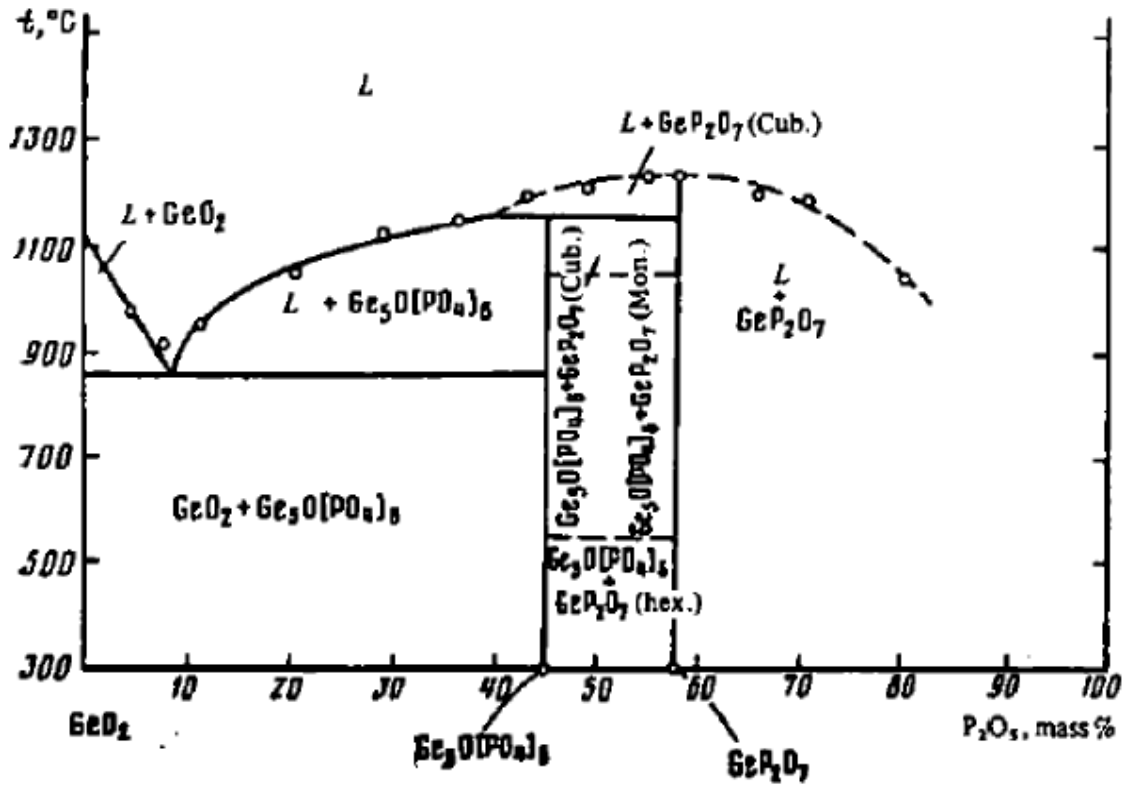


Figure 8. The $\text{GeO}_2\text{-P}_2\text{O}_5$ phase diagram²⁸

The structure was reported by H. Mayer et al to belong to the R-3 space group with the cell parameters $a=7.94 \text{ \AA} \pm 0.004$ $c=24.87 \text{ \AA} \pm 0.01$ and $Z=3$.

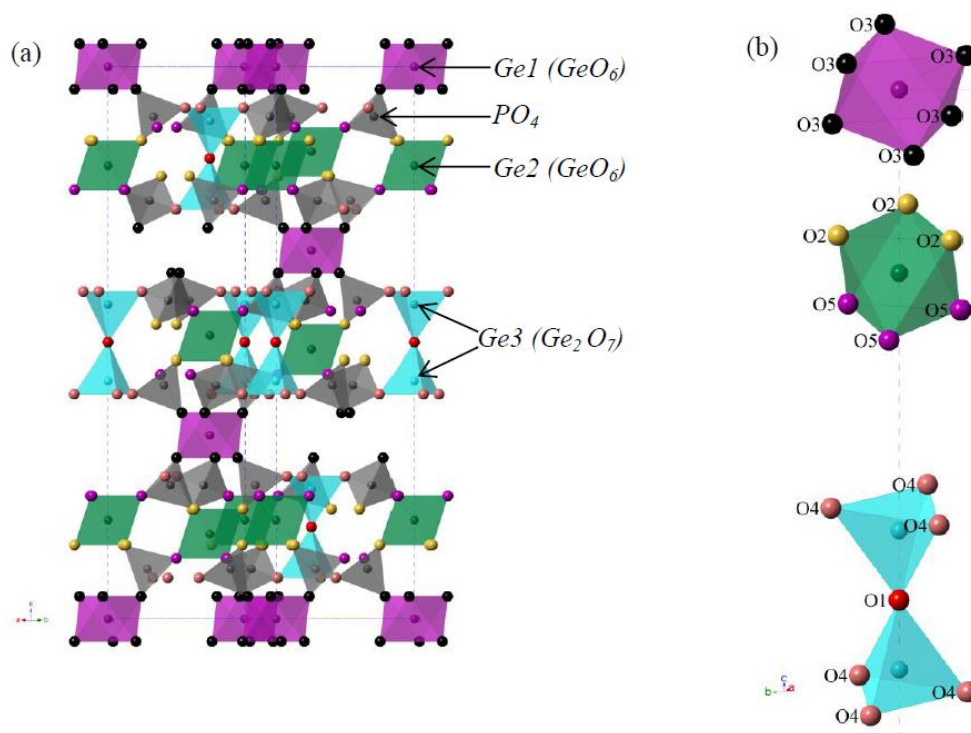


Figure 9. Projection of $\text{Ge}_5(\text{PO}_4)_6\text{O}$ along [100]. a) shows the whole structure where purple spheres are Ge1, green spheres are Ge2, and light blue spheres are Ge3. b) shows the oxygen environments. The red sphere is O1, yellow spheres are O2, black spheres are O3, pink spheres are O4 and purple spheres are O5. Figure taken from M. Tham⁷

The crystal structure of $\text{Ge}_5\text{O}(\text{PO}_4)_6$ is comprised of GeO_6 octahedra and (Ge_2O_7) ditetrahedral structures that are connected together by PO_4 units to form a 3-dimensional network. The network contains three different environments for germanium which are aligned along the c-axis. In Ge(1) and Ge(2) the germanium is at the centre of an octahedron. In Ge(1) all of the coordinated oxygens are symmetry equivalent (O3) while the Ge(2) octahedra contain two groups of symmetry related oxygen containing three oxygen atoms each (O2 and O5). Finally Ge(3) forms a tetrahedron with oxygen O(4) and O(1). Two of these tetrahedra form a bipyramid structure linked through O(1). All of the terminal oxygens are connected to phosphorous to form PO_4 groups which link the octahedral and bipyramidal structures to each other^{29,30}.

$\text{Ge}_5\text{O}(\text{PO}_4)_6$ can be classified as an excess ion conductor similar to previously discovered interstitial ion conductors. Previous NPD studies of the material conducted by the Irvine Group⁷ have shown that interstitial oxygen sites are located within the area around the excess oxygen O1.

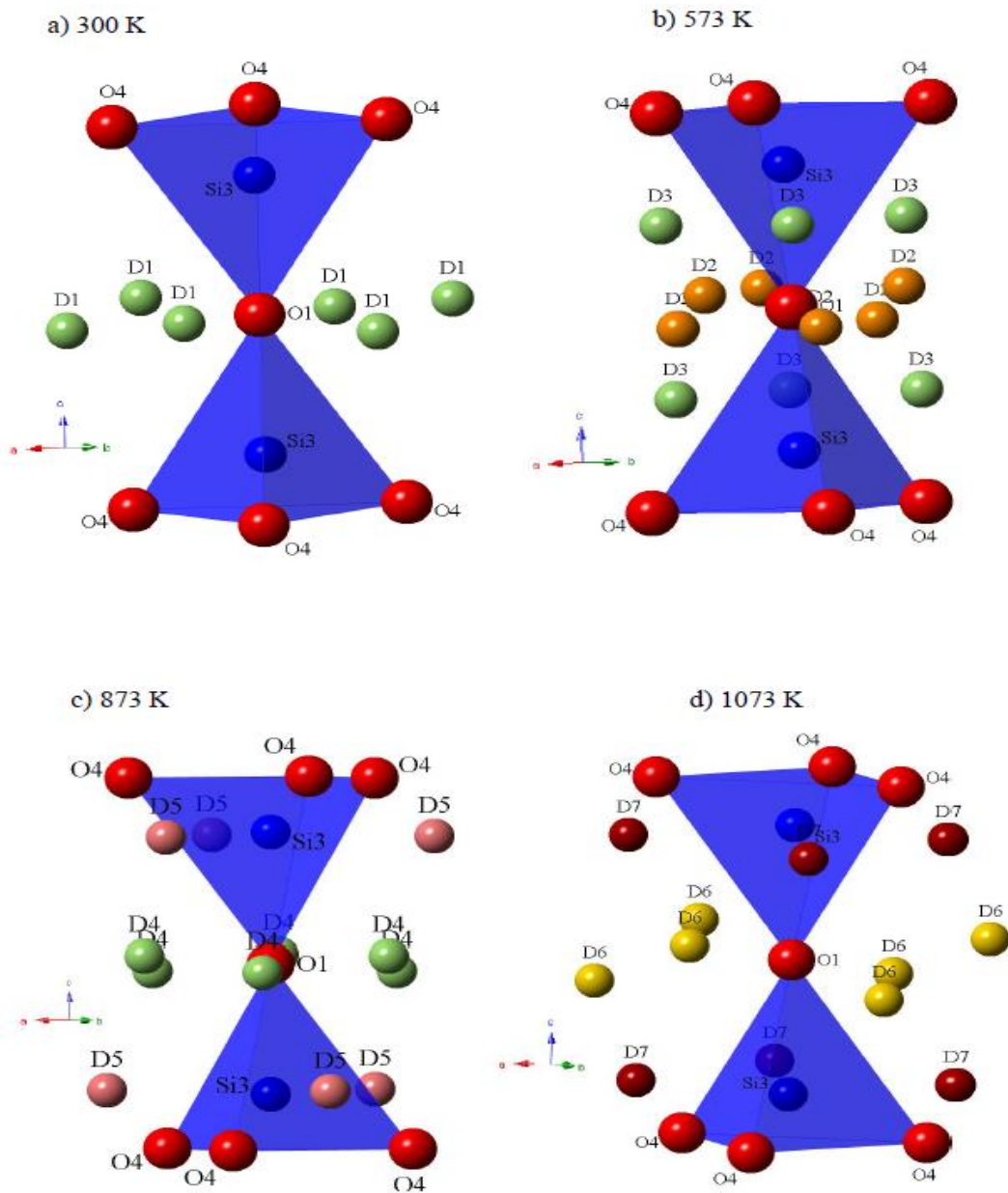


Figure 10. The interstitial oxygen sites (green, orange and yellow) as found by M. Tham.

The presence of these sites as well as the fact that this is the only oxygen not bound to a phosphorous atom has led to speculation that this atom could be easily mobilised and therefore may be part of the oxygen migration pathway.

The NPD studies also showed the possible presence of germanium sites located in the cavities located above and below the bi-pyramid structure.

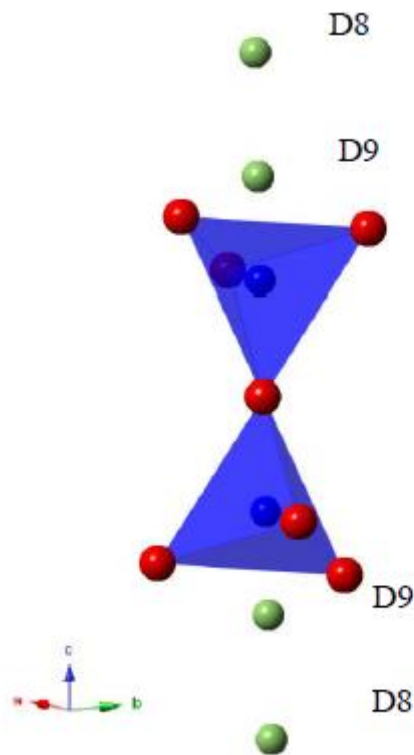


Figure 11. The interstitial germanium sites (green) as found by M. Tham.

The locations of these sites and the research on other similar materials which shows that conductivity occurs along their c-axis has led to the proposal that this material also offers an interstitialcy conduction pathway located along the C-axis.

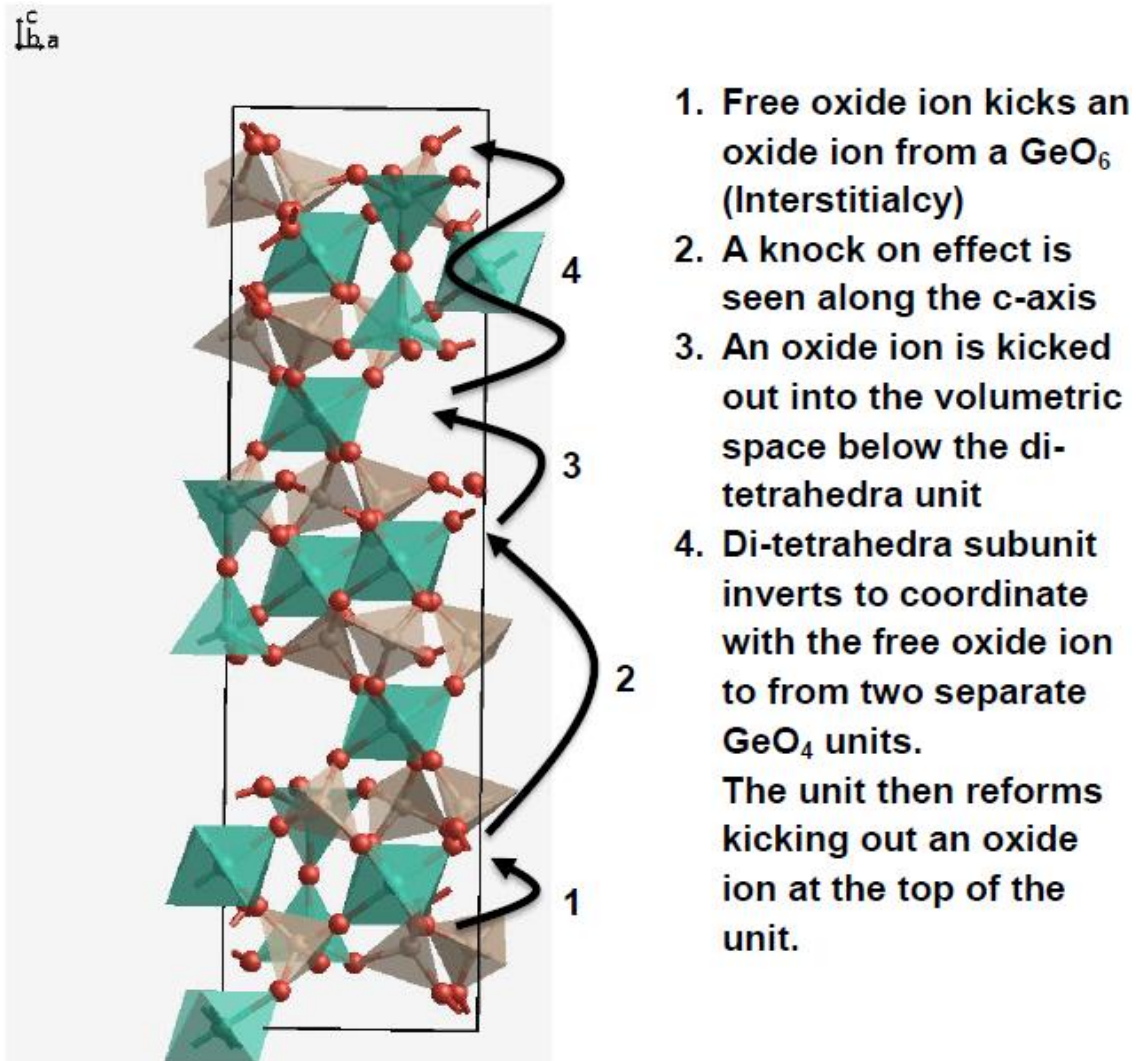


Figure 12. The interstitialcy pathway along the C- Axis proposed by M. Tham.

1.4. Aim of research Project

The aim of this project will be to undertake first principles calculations to further our understanding of the conduction mechanism of $\text{Ge}_5\text{O}(\text{PO}_4)_6$ and its related alternative structures. It will examine possible vacancy, interstitial and interstitialcy mechanisms in an attempt to determine if the previously suggested conduction mechanism for $\text{Ge}_5\text{O}(\text{PO}_4)_6$ is correct or if another pathway is used.

1.5. Background on Oxygen Storage Materials

1.5.1. Uses of Oxygen Storage Materials

Oxygen Storage materials are very important in the development of green energy solutions. Two of their main uses are in catalytic converters in cars and as cathodes/electrolytes in SOFCs. In catalytic converters they are used to help oxidise CO and unburnt hydrocarbons and can also store the oxygen produced by the reduction of NO. In Solid Oxide Fuels their use is to provide the oxygen ions that are transported across the electrolyte.

1.5.2. Cerium Oxide

The main class of materials used for oxygen storage are the metal oxides (MO_x). These materials can be used to store or release oxygen via the systematic use of oxidising or reducing conditions respectively. Ceria (CeO_2) is one of the most widely used metal oxides due its high oxygen storage capacity (OSC) that comes from its ability to form defects quickly. The OSC of Ceria can be improved via the doping of differently charged cations into the cerium sub lattice. The mechanistic reasons for this were investigated by Kehoe, Scanlon and Watson in their paper “Role of Lattice Distortions in the Oxygen Storage Capacity of Divalently Doped CeO_2 ”³¹. In the paper they investigate how the reduction energy is affected by different transition metals and how these metals actually distort the CeO_2 lattice structure. Normally ceria adopts a fluorite structure with Ce in cubic co-ordination and O in tetrahedral co-ordination. Kehoe et al. found that a number of stable configurations exist for doped cerium oxide, depending on which metal was used as a dopant. In each of these new configurations the bond

lengths between some of the cerium and oxygen atoms were lengthened allowing the bonds to be broken more easily.

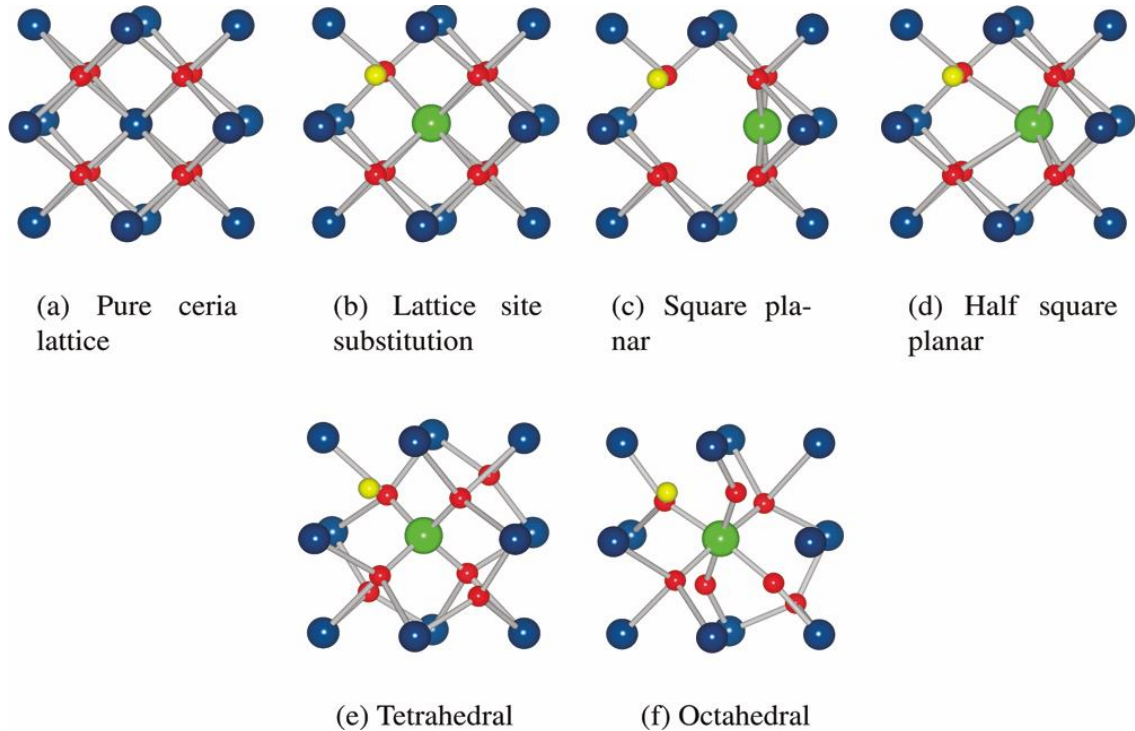


Figure 13. The different lattice configurations probed by the paper written by Kehoe et al. Blue represents cerium, red represents oxygen, green represents the dopant and yellow represents an oxygen vacancy. Figure taken from Kehoe et al. (2011)³¹

The authors show that group 2 metals substitute one of the ceriums in the lattice, which affects the lengths of the bonds around the dopant. They also found that the transition metals tended to be located in a square planar (for Pd, Cu, and Pt), octahedral (for Ni) or tetrahedral (for Zn) configuration instead of sitting in a lattice site. In all of these cases in addition to the previously mentioned changes in the bond lengths of the attached oxygens it was also found that a charge compensating oxygen vacancy (CCV) had been formed next to the dopant. The authors found that the actual size of the dopant atom was

not the most important factor in the creation of the lattice distortions associated with the increase in OSC. They concluded that the electronics of the dopants (crystal field effects) had a larger impact on the lattice structure than the actual dopant size. This was shown by the fact that the group 2 elements did not distort the lattice to a large enough extent to significantly affect the energy required for the reduction of CeO_2 , while the transition metals such as palladium or platinum distorted the lattice to a greater extent than the larger group 2 elements that appear later in the periodic table, allowing for a greater change in the energy required for the reduction.

Copper Doped Ceria

Of the dopants mentioned above, the Irvine group is most interested in the use of copper. Several studies³²⁻³⁴ have indicated that copper can be doped into the ceria lattice, however there is no consensus on the concentration of copper that can be placed into the ceria lattice before a secondary phase is formed. There is also some debate as to the oxidation state of copper that is doped into ceria. While the above studies have shown the ability of Cu^{2+} to be doped into Ceria, there has also been a report of the possibility of Cu^{3+} doping³⁵.

Documented uses of Copper Doped Ceria

As mentioned above there have been several studies into copper doped ceria and its use. One of these uses is as a part of the catalytic conversion process in cars. This process was investigated by S. Li et al.³⁶ who examined the effectiveness of copper doped ceria nanostructures in the oxidation of CO and reduction of NO. In their paper they were able to create single phase 10% copper doped ceria nanobundles and nanorods. These bundles and rods were compared against each other and against regular CeO_2 nanorods.

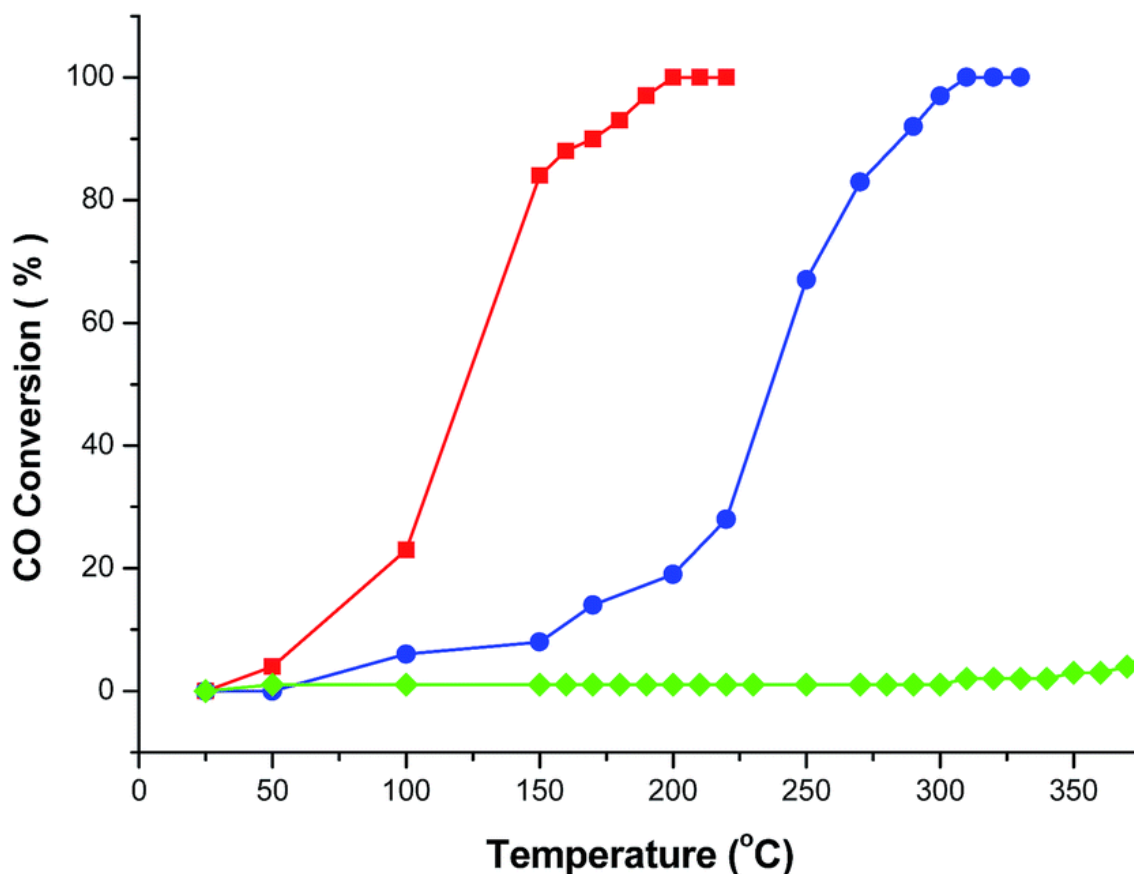


Figure 14. CO conversion vs reaction temperature (red line: CeO₂:Cu²⁺ nanorods, blue line: CeO₂:Cu²⁺ nanobundles, and the green line represents pure CeO₂ nanorods). Figure taken from Li et al.³⁶.

They found that the copper doped ceria samples showed a greatly enhanced oxidation of CO in comparison to regular CeO₂. This increase in activity was attributed to the copper doped ceria samples having a much larger BET surface area (The surface of the material is calculated using the Brunauer–Emmett–Teller³⁷ theory which uses probing gases in order to look at multi-layer adsorption on a surface.), with the nanorods having a specific surface area of 72.12 m² g⁻¹ and the nanobundles having a surface area of 52.90 m² g⁻¹. In addition to these nanorods and nanobundles, the paper also examined nanocrystals formed from Ce(Cu) metal organic frameworks (MOFs). The paper examined MOFs using the ligands benzenedicarboxylic acid (BDC) and 4,4'-biphenylcarboxylic acid (BPDC). It was found that these nanocrystals had even larger

surface areas (66.11 and $97.00 \text{ m}^2 \text{ g}^{-1}$ respectively) which led to 100% conversion rates.

The researchers then tested the ability of these structures to convert NO.

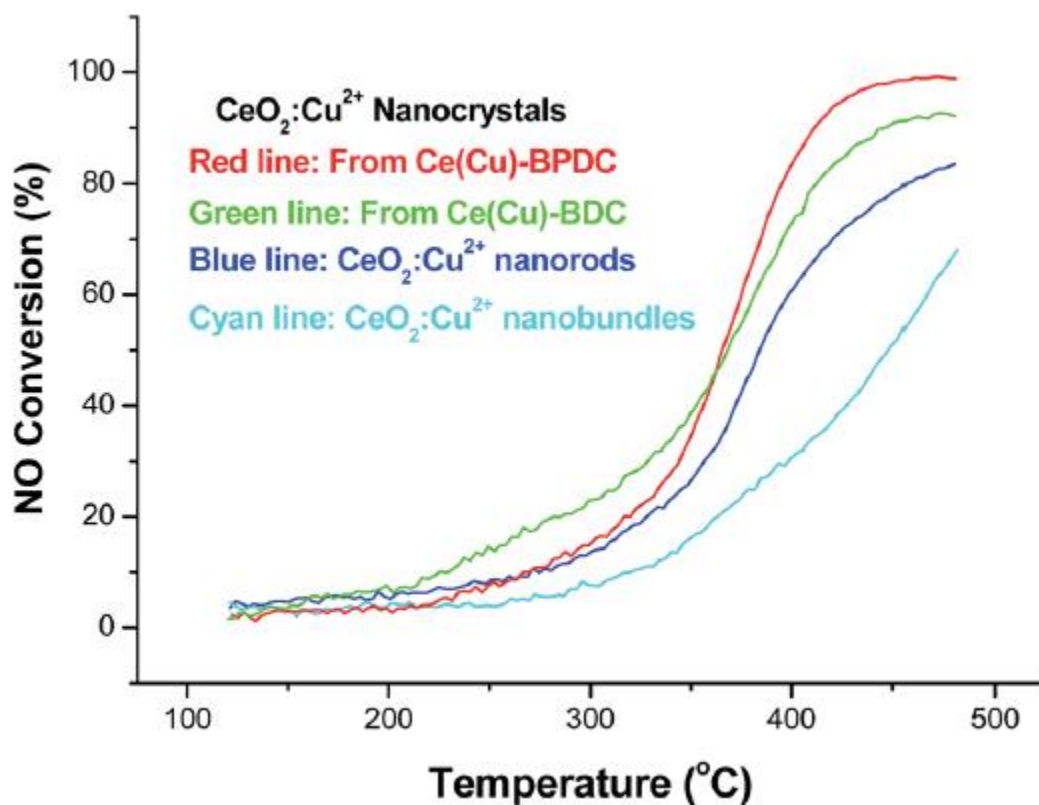


Figure 15. Profiles of NO conversion as a function of reaction temperature. Figure taken from Li et al.³⁶.

The paper found that these nanostructures also have an NO conversion ability which followed the same trend as in CO oxidation with respect to surface area size.

The use of copper doped ceria as a catalyst for Co oxidation was also examined by W. Zhu et al.³⁸ who created a series of Cu doped ceria nanospheres representing doping concentrations from 0% up to 7.5% copper doping.

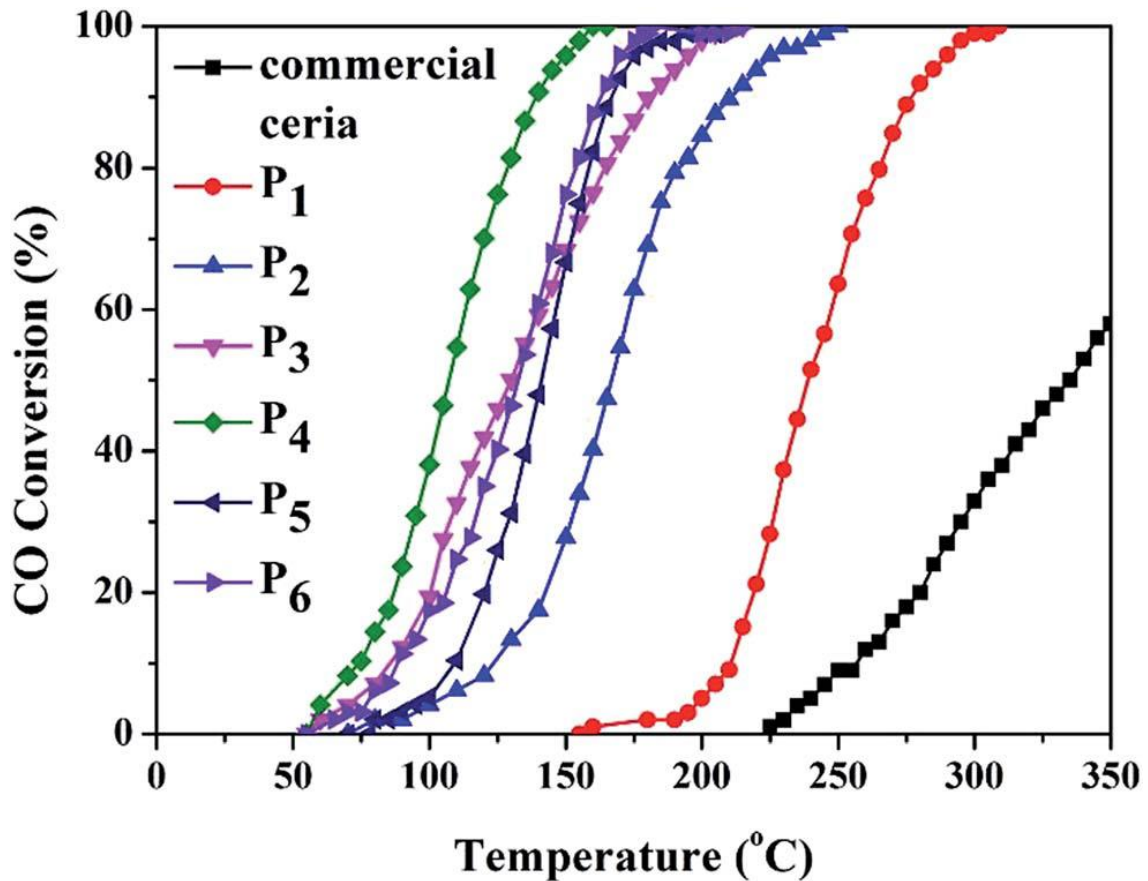


Figure 16. Conversion of CO. Comparing commercial ceria with copper doped samples (P1= 0%, P2 = 0.5%, P3 =1.5%, P4 = 2.5%, P5 = 5.0%, and P6 = 7.5% copper doping). Figure taken from Zhu et al.³⁸

The study found that doping copper into ceria increased its catalytic performance, with the performance increase in line with increasing amounts of copper doping.

Another study that examined the use of copper/ceria mixtures in car exhaust systems was conducted by Giménez-Mañogil et al.³⁹. In their paper the authors examine the use of CuO/Ceria-Zirconia catalysts in soot combustion. They report the production of a variety of samples under different conditions such as physical mixing, impregnation and co-precipitation methods. The samples prepared via impregnation and co-precipitation were reported to cause the copper on the surface to be more finely precipitated which was caused by sub-surface copper being exsolved back out of the material and onto its

surface. The increase in copper-ceria interactions in these samples was linked to an increase in the reducibility of CuO to Cu₂O. This reportedly allowed for a larger soot conversion rate when compared to a Pt/Al standard. This effect was also reported by other authors such as Rao et al.⁴⁰ who reported that small CuO particles on a ceria support promoted contact between the catalyst and the soot.

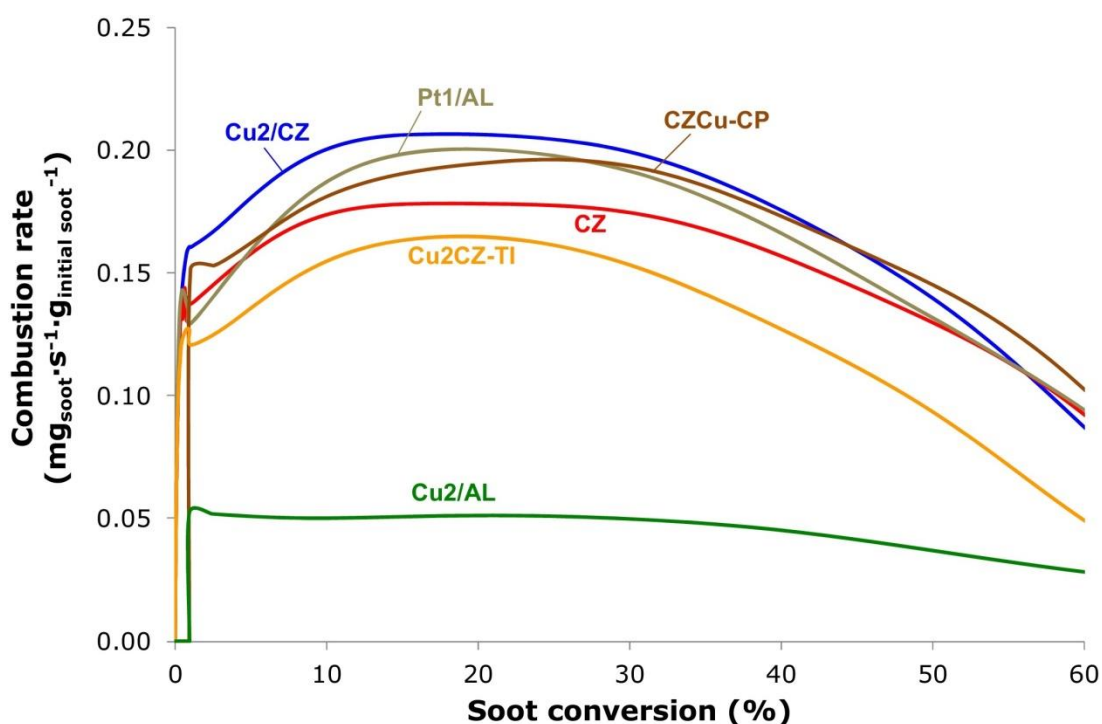


Figure 17. Isothermal soot combustion at 450 °C (under NO_x/O₂) (Cu2/CZ represents 2% weight copper catalyst on a ceria/zirconia support prepared via impregnation, CZCu-Cp represents a sample prepared via co-precipitation, Pt1/AL was the standard, CZ represents ceria/zirconia with no copper doping, Cu2Ca-Ti represents a sample with tight contact via physical mixing, and Cu2/AL is sample where copper has been mixed with γ -Al₂O₃). Figure taken from Giménez-Mañogil et al.³⁹

Another use for copper doped ceria is oxidation of methanol to produce formaldehyde and the oxidation ethylene. The effect of copper doped ceria on these reactions was studied by R. Dzeimbaj et al.⁴¹. In their paper they tested the catalytic activity of solid solutions of copper doped ceria for up to 25% doped copper. They found that the solid

solution was able to act as a catalyst in both of these oxidations with the catalytic ability of the copper doped ceria as the copper doping percentage was increased to 20% after which the catalytic activity began to decrease. They linked this effect to both the crystallite size as well as on the oxygen vacancy concentration within the crystal.

The above papers show that copper doped ceria can be used as an effective catalyst in a variety of oxidation and reduction processes. However they do not agree on a defined percentage on the maximum amount of copper that can be doped into ceria, with some claiming that certain production methods only allow copper to be present on the surface and not inside the bulk structure.

Aim of research Project

The aim of this project will be to establish a thermodynamic model description of Ce-Cu-O fluorite by employing the CALPHAD⁴²⁻⁴⁴ technique. The model will be used to calculate the thermodynamic limit of copper doping under oxidising and reducing conditions at different temperatures. Moreover, our thermodynamic calculations will reveal thermal and oxygen partial pressure dependent trends of charge disproportionation reactions between different valencies in the fluorite structure and changes of vacancy concentrations.

Chapter 2: Computational Methods

In order to investigate oxygen storage and migration we have used ab-initio quantum chemistry methods. These methods are also known as first-principles methods and are used to solve the electronic Schrödinger equation.

2.1. First Principles Calculations

First Principles calculations, or Quantum mechanics calculations (QM), are used by chemists to calculate the properties of a system (energy, activation barriers, thermodynamic properties etc.). These can then be used to guide future lab work or to explain previously obtained results. This approach is very successful for small systems, however it becomes rapidly more demanding as the system size increases. This has led to research looking at the improvements of these methods. The original Hartree Fock (HF) methods used have gradually fallen out of favour for newer Density Function Theory (DFT) methods which scale better with increasing system size. In this work all of the first principles calculations were carried out using DFT and as such the basis of this method and its difference to HF will be discussed.

2.1.1. Basic Concepts

The time-dependent Schrödinger equation was formulated in 1926 by Erwin Schrödinger:

$$i\hbar \frac{\partial \Psi}{\partial t} = H\Psi \quad (2.1)$$

In this equation the term i is the imaginary unit (so $i^2=1$), \hbar is Planck's constant divided by 2π , t is the time, H is the Hamiltonian and Ψ is the wavefunction. The equation is

used to describe how the quantum state of a system changes with time. This equation is the basis for all quantum dynamics. The equation can be simplified for use in systems where the time is not a factor. When simplified the equation gives:

$$H\Psi = E\Psi \quad (2.2)$$

This equation is known as the time-independent Schrödinger equation. This equation works as an eigenvalue equation. In an eigenvalue equation an operator is used on an eigenfunction to give an eigenvalue. In this case the Hamiltonian can be used on the wave function to give the energy.

The Hamiltonian in the time-independent equation can be broken down into terms for the kinetic energy (T) and potential energy (V) (where r represents the position vector)⁴⁵.

$$H(r)=T(r)+V(r) \quad (2.3)$$

These energy terms are dependent on several sub energies. These sub terms include terms for nuclear kinetic energy, electronic kinetic energy, nuclear-electron potential energy, inter-electron potential energy and inter-nuclear potential energy.

To calculate all of the nuclear and electronic terms together leads to unwieldy mathematical calculations. As such the Born Oppenheimer approximation was created to simplify this problem.

2.1.2. The Born-Oppenheimer Approximations

The Born –Oppenheimer approximation⁴⁶ is used to simplify both the wave function and Hamiltonian. The approximation considers nuclei to be static on the timescale of electronic relaxation due to the fact that they are far larger and heavier than electrons. This allows us to consider the nuclear kinetic energy of the system to be zero and for nuclear-nuclear repulsion to be constant⁴⁷. This allows us to simplify the Hamiltonian to the electronic Hamiltonian.

$$H_{electronic} = -\frac{1}{2}\sum_i^n \nabla_i^2 - \sum_i^n \sum_A^m \frac{Z_A}{r_{iA}} + \sum_i^n \sum_{j>i}^n \frac{1}{r_{ij}} \quad (2.4)$$

As we have simplified the Hamiltonian we can also simplify the wavefunction to the electronic only wavefunction. This wave function only contains information about the coordinates and spin states of the electrons

$$\Psi_{electronic} = \Psi(X_1, X_2, \dots, X_n) \quad (2.5)$$

These can then be placed into what is known as the electronic schrödinger equation:

$$H_{elec}\Psi_{elec} = E_{elec}\Psi_{elec} \quad (2.6)$$

The main challenge is to find an appropriate expression for the wavefunction. It is at this point that computational chemistry diverges into two different strategies. The first being the Hartree-Fock method which attempts to directly calculate the wave function and the second being Density Functional Theory which uses the electron density to calculate the properties of the system.

2.1.3. Hartree-Fock Method

In the Hartree-Fock method it is assumed that the electronic wavefunction can be described by an anti - symmeterised product of one-electron orbitals. This can be expressed as a single Slater determinant:

$$\Psi(X_1, X_2, \dots, X_n) = \frac{1}{\sqrt{n!}} \begin{vmatrix} \psi_1(X_1) & \psi_2(X_1) & \dots & \psi_n(X_1) \\ \psi_1(X_2) & \psi_2(X_2) & \dots & \psi_n(X_2) \\ \dots & \dots & \dots & \dots \\ \psi_1(X_n) & \psi_2(X_n) & \dots & \psi_n(X_n) \end{vmatrix} \quad (2.7)$$

This determinant is anti-symmetric so that it obeys the Pauli principle of anti-symmetry.

As a result of this approximation we must find the optimal terms for the one-electron orbitals used within the Slater determinant. In order to achieve this we can use the variation principle which states that any trial wavefunction will give a higher energy than the actual real energy of the system

This allows us to use the equation:

$$E = \frac{\int \Psi_{trial}^* H \Psi_{trial} dx}{\int \Psi_{trial}^* \Psi_{trial} dx} \quad (2.8)$$

Via this equation and the variation principle we can see that when $E=E_0$ then $\Psi_{trial} = \Psi_0$, thus to obtain the best molecular orbitals for Ψ_0 we simply use the ones with the lowest energy⁴⁷.

Each one of these molecular orbitals can be broken down again and described by a linear combination of atomic orbitals or (LCAOs). This gives us the following equation:

$$\psi_i = \sum_{\mu}^n c_{\mu i} \varphi_{\mu} \quad i = 1, 2 \dots n \quad (2.9)$$

Where φ_μ are the atomic orbitals, each atomic orbital is an atom centred one electron function known as a basis function. The contribution of each basis function to the molecular orbital is controlled by the coefficient $c_{\mu i}$.

To optimize the molecular orbitals we must then optimise these coefficients. To achieve this we first generate an initial set of coefficients based upon a best guess to generate a trial wavefunction. This wavefunction is then placed into what are known as the Hartree-Fock (HF) equations. The HF equations are analogues of the previously described Schrödinger equation.

$$\hat{f}_i(X_i)\psi_i(X_i) = \epsilon_i\psi_i(X_i) \quad (2.10)$$

In this equation the Hamiltonian is approximated by what is known as the Fock operator or \hat{f}_i . This 1-electron Fock operator can be broken down into:

$$\hat{f}_i(X_i) = -\frac{1}{2}\nabla_i^2 - \sum_A^m \frac{Z_A}{r_{iA}} + v^{HF}(X_i) \quad (2.11)$$

This expression for the Fock operator contains three main terms. The first term contains information about the one-electron kinetic energy while the second contain information regarding the one-electron potential energy. The one-electron integrals for these can be written as:

$$H_i = \left(-\frac{1}{2}\right) \int \psi_i^*(r_1)\nabla_i^2\psi_i(r_1)dr_1 + \sum_A^m(-Z_A) \int \frac{|\psi_i(r_1)|^2}{|r_1-R_A|} dr_1 \quad (2.12)$$

The third term of the Fock operator is the electron-electron repulsion. The repulsion is given by an approximation called the “mean field” approximation⁴⁷ and is calculated by

giving the average electronic field seen by the i^{th} electron due to the presence of the other electrons in the system.

This repulsion term includes two types of electron-electron interactions which are the Coulombic and exchange interactions. Instead of a one electron integral both of these terms are described by two electron integrals. The Coulombic integrals are given by the equation:

$$J_{ij} = \int \int \frac{|\psi_i(r_1)|^2 |\psi_j(r_2)|^2}{|r_1 - r_2|} dr_1 dr_2 \quad (2.13)$$

These integrals are always positive and describe the repulsion of two electronic charge clouds.

The exchange integrals are given by the equation:

$$K_{ij} = \int \int \frac{\psi_i^*(r_1) \psi_j^*(r_2) \psi_i(r_2) \psi_j(r_1)}{|r_1 - r_2|} dr_1 dr_2 \quad (2.14)$$

These integrals are used to describe the effect of switching electronic labels.

The exchange integrals are negative for same-spin electrons while they are zero for opposite-spin electrons. As a result this exchange interaction partially offsets the Coulombic interaction.

Using these equations we can therefore simplify the equation of the Fock operator for the i^{th} electron to:

$$\hat{f}_i = H_i + \sum_{j=1}^N (2J_{ij} - K_{ij}) \quad (2.15)$$

N is the number of doubly occupied Molecular Orbitals in a closed shell system.

2.1.4. Post Hartree-Fock Methods

In HF one of the main approximations is the “mean field” approximation. Due to this approximation the Coulombic potential felt by each electron is treated as a homogeneous mean field of all of the other electrons and so the motion of each electron in the system is independent of every other electron (except for exchange). In a real system the positions of the electrons would be correlated with each other to minimise repulsion and so decrease the systems energy. As a result there is always a difference between the HF calculated energy and the “true” energy known as the correlation energy⁴⁵.

$$E_{true} = E_{HF} + E_C \quad (2.16)$$

E_{HF} reaches its limiting value with use of an infinite set of basis functions and the correlation energy is always negative. Several methods known as post –HF methods have been developed, to try to recover the correlation energy via exciting electrons from their ground state into unoccupied virtual orbitals.

2.1.5. Density Functional Theory

Density Functional Theory (DFT) was developed to provide an alternative to Hartree Fock Theory. DFT attempts to simplify the mathematical relations used to find the energy of a system by establishing a direct link from the electronic density of a system to its energy. This therefore would decrease the computational power needed to investigate larger systems and would solve the problem of electronic correlation similarly to post HF methods.

2.1.5.1. Hohenberg-Kohn Theory

In DFT the determination of the Hamiltonian is based upon the Hohenberg – Kohn theorem which was proved in 1964⁴⁸. This theorem can be summed up by three statements. The first statement says⁴⁹:

“The electron density determines the external potential (to within an additive constant).”

From this statement we can conclude that the Hamiltonian of a system can be determined by the electron density as the Hamiltonian is determined via the use of the external potential (which the statement indicated is related directly to the electron density) and the number of electrons in the system which can be computed via the integration of the density over all space. Given that we can now determine the Hamiltonian of a system via its density we can theoretically determine the wavefunction of the system and thus determine all properties of the system. This therefore allows the first statement to be summarised to say that the energy of a system is a functional of the systems' density.

The second statement establishes a variation principle⁴⁹:

“For any positive definite trial density, ρ_t , such that $\int \rho_t(\mathbf{r}) d\mathbf{r} = N$ then $E[\rho_t] \geq E_0$ ”

This statement restricts DFT so that it can only be used to predict ground states.

The third statement is a result of the two theorems above and states that the energy functional can be written as a functional $F[n]$:

$$E[\rho] = \int \rho(\mathbf{r})v(\mathbf{r})d\mathbf{r} + F_{\text{HK}}[\rho] \quad (2.17)$$

The ground state energy and density correspond to the minimum of the Functional $F[n]$. This means that we can establish that there is a universal functional that is independent of the potential of the system that is being assessed, meaning that it has the same form for all systems. This theoretically then allows to obtain the exact ground state and energy of any system.

2.1.5.2. Kohn-Sham Method

Density Functional Theory contains a shortfall in its description of the kinetic energy of a system. In response to this failing Kohn and Sham⁵⁰ developed a practical method by which to approximate this energy. To achieve this they used a fictitious system of non-interacting electrons which are placed in an external potential (the Kohn-Sham potential) that allows the ground state density to be the same as the density of the real system of interacting electrons. Similarly to the Hartree-Fock method, this non – interacting system is described via the use of a single Slater determinant. The energy of this non-interacting system can be given by the following equation:

$$E_{ni}[\rho] = T_{ni}[\rho] + V_{ne}[\rho] + J_{ee}[\rho] \quad (2.18)$$

The terms of the equation on the right hand side are the kinetic energy of the non-interacting electrons, the external potential and the classical electron-electron repulsion respectively.

Of course a real system would also contain quantum interactions which would effect both the kinetic and potential energy. As such the energy of a real system can be shown to be:

$$E_{KS}[\rho] = E_{ni}[\rho] + E_{xc}[\rho] \quad (2.19)$$

This shows that the overall energy of the system is a combination of the energy of the non-interacting system plus an exchange-correlation energy made up of kinetic and potential energy contributions:

$$E_{xc}[\rho] = \Delta T[\rho] + \Delta V_{ee}[\rho] \quad (2.20)$$

The minimisation of the system energy can then begin with the introduction of the one-electron orbitals into the Kohn-Sham equations:

$$h_i^{KS}\psi_i(\mathbf{r}_i) = \epsilon_i\psi_i(\mathbf{r}_i) \quad (2.21)$$

The Kohn-Sham operator shown above is an analogue of the Fock-operator from HF Theory.

$$h_i^{KS} = -\frac{1}{2}\nabla_i^2 - \sum_A^m \frac{Z_A}{r_{iA}} + \int \frac{\rho(\mathbf{r}')}{|\mathbf{r}_i - \mathbf{r}'|} d\mathbf{r}' + V_{XC} \quad (2.22)$$

The first three terms of the right side of the equation correspond to $T_{ni}[P]$, $V_{ne}[P]$ and $J_{ee}[P]$ respectively. The last term is analogous to the Hartree-Fock potential and is a derivative of the system's density:

$$V_{XC} = \frac{\delta E_{XC}}{\delta \rho} \quad (2.23)$$

Similarly to HF theory the one-electron operators are expressed in terms of a set of basis function which the Kohn-Sham operator acts on to generate an energy and new orbital coefficients. The Kohn-Sham operator uses the electron density as an argument and so an initial guess for the electron density must be made. The Kohn-Sham equations then generate a new density:

$$\rho(\mathbf{r}) = \sum_{i=1}^n |\psi_i(\mathbf{r})|^2 \quad (2.24)$$

This allows an optimal value for the density to be found iteratively in a manner that is analogous to the optimisation of the MO coefficients in HF theory^{47,50}.

In these equation we have mentioned the exchange correlation term, V_{XC} . This term if known would allow the self-consistent solution of the Kohn-Sham equations to be exact. However it is not known leading to approximations being necessary.

2.1.5.3. Local Density Approximation

There are several different levels of approximation for the exchange-correlation functional, with the simplest being the Local Density Approximation (LDA). In LDA the exchange and correlation function depends only on the electron density at that particular point in space. This method therefore assumes that the exchange correlation energy for that point in space can be considered to be the same as the energy for a locally uniform electron gas of the same charge density, often leading to an overestimation of the exchange-correlation energy.⁴⁷

2.1.5.4. Generalised Gradient Approximation

The generalised gradient approximation (GGA) expands the exchange correlation energy adding in terms to describe the gradient of the electron density. This allows the overestimation of the energy found in LDA to be corrected. The PBE⁵¹ functional used in several parts of the work described in this thesis is classified as a GGA functional.

2.1.5.5. The +U Correction

A popular set of functionals used in calculations regarding metals like Ceria are the DFT+U set of functionals. Examples of its use in DFT calculations of Ceria systems can be found in several papers. The GGA+U functional PBE+U was used in the paper by Kehoe et al.³¹ mentioned in chapter 1.5.2. where they examined the doping of transition metals into the ceria lattice. Other examples of investigations of doped ceria systems using this method include papers by Yang et al.⁵² and Yeriskin et al.⁵³ which investigated Palladium and Lanthanum doped ceria systems respectively. In the GGA+U potential a Hubbard term or “U” is added to the functional used by the first principles program (for example PBE+U. This term is used to help describe the onsite Coulomb interaction of the 4f electrons in the Ceria atoms. This solves a known problem in the calculation of Ceria systems with non –Hubbard corrected GGA functionals, in which the energy of the band gap is under estimated, resulting in incorrect energies for optimized structures. The use of the Hubbard correction does however come with its own problems as mentioned in a paper by Huang et al.⁵⁴. The Hubbard potential is not a universal constant, and no single optimal value captures all of the structural and electronic properties of Ceria, as well as the energetics of its reduction. Due to this problem we have opted to use the hybrid HSE functional in the place of PBE+U despite its relative computational expense, as this hybrid functional also helps to correct the underestimation of the band gap but without the inconsistencies of the PBE+U method.

2.1.5.6. Hybrid Functionals

Hybrid functionals are functionals which are constructed so that they include a portion of Hartree-Fock exchange. The HSE⁵⁵ functional used in parts of this thesis is an example of a Hybrid functional. This functional is actually a range separated hybrid functional which uses an error function screened Coulomb potential which can be split into long range and short range interactions.

2.1.5.7. Dispersion Correction

One problem with DFT is that it neglects the treatment of London dispersion. London dispersion is an attractive force that is caused by instantaneous dipoles that arise from redistributions of electrons within a molecule or atom. As two atoms are brought together the electrons from one of the atoms will “flee” to the other side of the atom. This causes the atom to form a dipole that has its positive side facing the incoming atom which has a negative charge. As the size of the atoms increase this force becomes stronger. This means that London dispersion can have a large effect on condensed phases as we see multiple large atoms being forced together. Dispersion corrections have therefore been developed to try to artificially account for the dispersion forces. The corrections used in this paper are the Grimme D2 correction⁵⁶ which adds an attractive semi-empirical pair potential to the total energy of system, and the Grimme D3 correction⁵⁷, in which the dispersion coefficients are geometry dependent and are adjusted based upon the coordination number of the atoms.

2.1.5.8. Reciprocal Space

The systems explored in this thesis are all solid state systems that exist within periodic lattice structures. This periodic lattice structure can be converted into what is known as a reciprocal lattice by performing a Fourier transform on the real lattice structure. This reciprocal lattice can be broken up into what are known as Brillouin zones. The zones are constructed via the use of Bragg planes. A lattice point is chosen to be the origin and lines are drawn connecting it to all other lattice points. Bragg planes exist as perpendicular bi-sections of the connecting lines. The first Brillouin zone is the zone in which the defined lattice points have no Bragg planes between them and the origin and is the equivalent of the Wigner-Seitz unit cell of the reciprocal lattice. The construction of the Brillouin zone allows the use of Bloch wave function which is the wavefunction of a particle in a periodically repeating environment. The wave function samples the Brillouin zone over a number of points generally referred to as K-points.

2.1.5.9. Basis Sets

Basis sets are the set of basis functions that are used to generate the molecular orbitals (or bands in the periodic case) used in either Hartree Fock or DFT. These basis sets are usually built up using one of two methods which can be characterised broadly as either atom centred basis sets or plane wave basis sets.

2.1.5.10. Plane Wave Basis Sets

In calculations carried out on periodic systems the most widely used basis set type is the plane wave basis. In plane wave basis sets sine and cosine functions are used to expand

the bands or molecular orbitals so that they expand infinitely through space. In this basis set type the contribution of kinetic energy is determined by the frequency of the wave.

$$\psi(X) = A \cos(Kx) + B \sin(Kx) \quad (2.25)$$

In this equation K is the wave vector and A and B are coefficients. K is determined by a relationship with the size of the unit cell t:

$$Kt = 2\pi m \quad (2.26)$$

Where m is a positive integer. The energy can then be given by K:

$$E = \frac{1}{2}K^2 \quad (2.27)$$

A maximum cut-off for the energy is usually enforced⁴⁵.

2.1.5.11. Pseudopotentials

When a plane wave basis set is used on a periodic system, a problem arises regarding the treatment of the core electrons of any atomic species that are present. Plane wave basis sets have a character that varies slowly, which means that a large number of them must be used when describing the core electrons. This is due to the fact that the wavefunctions of the core electrons oscillate rapidly. This would result in inefficient calculations that would take vastly more time. In order to combat this we can use a fitted function known as a pseudopotential (PP) to represent the core electrons. The core electrons are usually not chemically relevant in a system and as such can be justifiably replaced with a mathematically simpler potential. This potential is fitted so that while it replaces the core electrons, it will not affect the valence behaviour of the electrons beyond a certain nucleus-electron cut-off distance.

In the fitting an initial calculation takes place to find the all-electron reference state. The core electrons are then replaced by the PP while the Hamiltonians of the valence electrons are modified to add a term to account for the core electrons⁴⁷. This allows the valence electrons to feel the effect of an “effective core”.

While certain computational packages use the above method for potential generation the package used in this thesis (VASP)⁵⁸⁻⁶⁰ comes supplied with pre-optimized potentials for each element and so does not need to generate these potentials “on the fly”.

2.1.6. Geometry Optimization

The most common calculation carried out in computational chemistry is the Geometry Optimization. During a geometry optimization we are attempting to place the atoms in our system of interest in a geometry that leads to the system being at its lowest possible energy on the Potential Energy Surface (PES). There are several different methods available to conduct these optimizations. In all methods we start from an unoptimized structure which has a known energy. We then move the atoms within the structure to form several trial structures which then have the energies and the forces felt by the structures calculated. In the most basic optimization algorithm known as “steepest descent” we simply then choose the structure for which the energy and forces have been decreased by the largest amount. We then continue to do this until the change in the energy and forces felt by the system converge to below a user determined number at which point the system is considered to be optimized. A more advanced version of the steepest decent algorithm is the “conjugate gradient” algorithm. This algorithm follows the same premise as steepest descent but also takes into account the results of the

previous step in the optimization. This ensures that any step taken does not redo or undo any previous step and so therefore normally results in the optimized structure being reached using a smaller number of steps. This conjugate gradient method is the method used by default in the VASP computational package used in thesis. Another possible method type is the “updated Hessian” method. In these methods a Hessian is constructed at the first step containing the second derivatives of the energy and the slope. This Hessian is used to help estimate the curvature of the PES. As each geometry step is conducted the Hessian is updated with the new second derivatives of the energy and slope. This then allows the PES to be updated to what should be a more accurate representation. This method therefore means that as the optimization goes on the PES becomes increasingly more accurate allowing for more accurate steps towards the energy minima to be taken.

2.1.7. Nudged Elastic Band

Nudged elastic band calculations⁶¹ are used to find the activation energy and reaction path of a process where an atom (ion, or any other particle) has moved from one position to another causing a change in geometry. This is achieved by probing the energy landscape between the two geometries to find the minimum energy pathway between them. In this type calculation we start with an initial and end geometry for a system. We then calculate starting geometries (also known as images) at points along a linear movement across the energy landscape between the two geometries. These images are then optimized to try to minimize their energy.

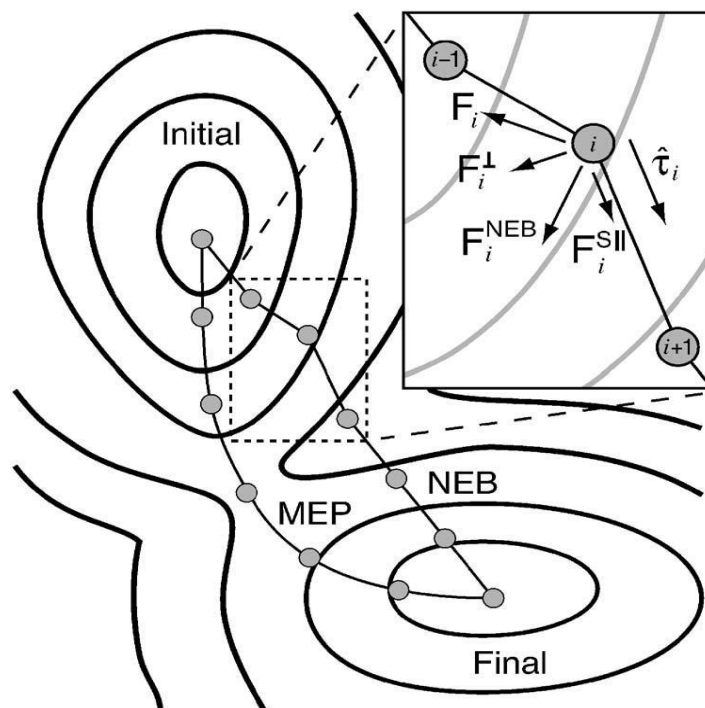


Figure 18. Showing an NEB containing 7 equally spaced images. These images are converged towards the MEP or Minimum Energy Pathway.

This would normally lead to all the images converging together towards the nearest local minima. To avoid this, spring constants are placed between each of the images to ensure that each point covers a different part of the pathway. However, as we can afford NEB calculations only with a small number of images, the NEB method does have one disadvantage. While we can ensure that the images are at their lowest possible energy in section of the pathway we cannot ensure that the highest point in the NEB is at the true maximum for that particular pathway. To solve this problem we can use a modification called the Climbing image modification⁶² or CI-NEB. In this modification we take the highest energy image in the NEB landscape and we remove the spring constants between it and its two neighbours. We can then reverse the force felt by this image and drive it up the slope in the energy landscape that it sits on. This allows this image to be

driven up to the actual maximum in the lowest energy landscape allowing us to see the structure of the transition state and know its energy.

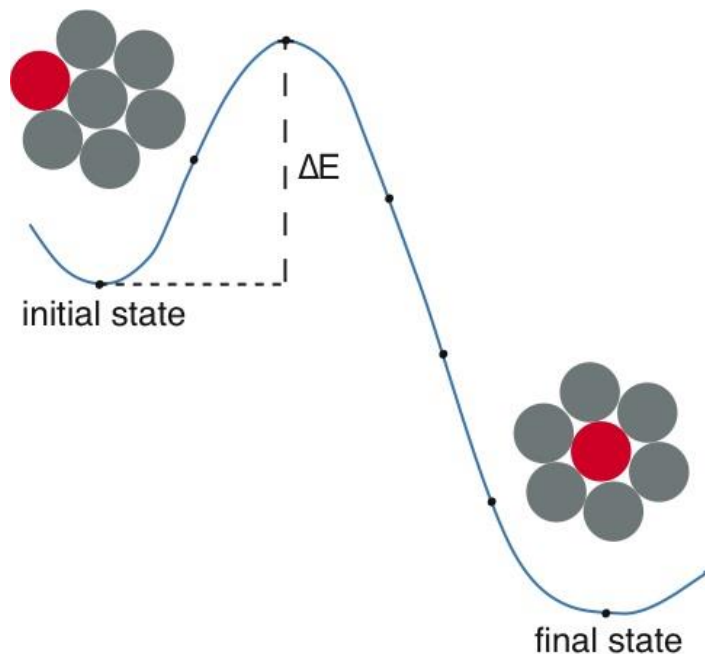


Figure 19. A climbing image NEB. The image at the energy maximum has been moved so that it is not equally spaced when compared to the images to its left and right.

2.1.8. Phonon Calculations

Phonon calculations are used in this thesis to calculate the thermodynamic properties of free energy, heat capacity and entropy.

In VASP, phonon calculations can be carried out with the help of the Phonopy package⁶³. This package allows the use of two different methods called Finite Displacement and Density Functional Perturbation Theory (DFPT). The results in this thesis are calculated using the Finite Displacement method. In this method a supercell of the material is modelled, and each atom in the material lattice is displaced one at a

time in a given direction by a small amount to produce displaced supercells. Single point calculations are carried out on the displaced unit cells to calculate the force felt by every atom in the system. In this setup the symmetry of the crystal structure is taken into account and if one displacement is the symmetric equivalent of one already produced then the displacement supercell is not produced. The force constants for the material are then calculated by using the following equation⁶³.

$$\phi_{\alpha\beta}(jl, j'l') = -\frac{F_{\beta}(j'l'; \Delta r_{\alpha}(jl)) - F_{\beta}(j'l')}{\Delta r_{\alpha}(jl)} \quad (2.28)$$

In this equation $F_{\beta}(j'l'; \Delta r_{\alpha}(jl))$ represents the forces felt by the atoms, $\Delta r_{\alpha}(jl)$ represents the displacement distance of the atoms and $F_{\beta}(j'l')$ is usually equal to zero.

These force constants are then used to create a dynamical matrix

$$D_{\alpha\beta}(jj', q) = \frac{1}{\sqrt{m_j m_{j'}}} \sum_{l'} \phi_{\alpha\beta}(j0, j'l') \exp(iq \cdot [r(j'l') - r(j0)]) \quad (2.29)$$

Where m is the atomic mass and q is the wave vector. From this dynamical matrix we can then write an equation of motion as

$$\sum_{j'\beta} D_{\alpha\beta}(jj', q) e_{\beta}(j', qv) = m_j [w(qv)]^2 e_{\alpha}(j, qv) \quad (2.30)$$

Where e_{α} and e_{β} are eigenvectors of the atomic displacement, and the eigenvector of the band index v at q is given by the diagonalization of $D(q)$:

$$\sum_{j\alpha j'\beta} e_{\alpha}(j', qv)^* D_{\alpha\beta}(jj', q) e_{\beta}(j', qv) = [w(qv)]^2 s_{vv'} \quad (2.31)$$

The phonon wave vectors and eigenvector of the band index obtained via the dynamical matrix are then used in thermodynamic equations to obtain the enthalpy, Helmholtz free energy and the constant volume heat capacity via the following equations⁶³:

$$S = -\frac{\partial F}{\partial T} \\ = \frac{1}{2T} \sum_{\mathbf{q}\nu} \hbar\omega(\mathbf{q}\nu) \coth(\hbar\omega(\mathbf{q}\nu)/2k_{\text{B}}T) - k_{\text{B}} \sum_{\mathbf{q}\nu} \ln [2 \sinh(\hbar\omega(\mathbf{q}\nu)/2k_{\text{B}}T)]$$

$$F = -k_{\text{B}}T \ln Z \\ = \varphi + \frac{1}{2} \sum_{\mathbf{q}\nu} \hbar\omega(\mathbf{q}\nu) + k_{\text{B}}T \sum_{\mathbf{q}\nu} \ln [1 - \exp(-\hbar\omega(\mathbf{q}\nu)/k_{\text{B}}T)]$$

$$C_V = \left(\frac{\partial E}{\partial T} \right)_V \\ = \sum_{\mathbf{q}\nu} k_{\text{B}} \left(\frac{\hbar\omega(\mathbf{q}\nu)}{k_{\text{B}}T} \right)^2 \frac{\exp(\hbar\omega(\mathbf{q}\nu)/k_{\text{B}}T)}{[\exp(\hbar\omega(\mathbf{q}\nu)/k_{\text{B}}T) - 1]^2} \quad (2.32-2.34)$$

2.2. CALPHAD

To create our phase diagrams we are using a computational method known as CALPHAD or Calculation of phase diagrams. The CALPHAD method first found ground in the 1970's with the first official meeting being organised by Dr. Larry Kaufman in 1973⁶⁴. The CALPHAD method of calculating phase diagrams is based on the fact that a phase diagram is the result of the calculation of the thermodynamic properties of an equilibrium system, and that these thermodynamic properties are the sum of the thermodynamic properties of all of the phases present, and so, by knowing

the thermodynamic properties of the individual phases we can calculate the overall phase diagram.

Several different computational packages have been developed based on the CALPHAD method. The software package being used in this project is the Thermocalc package⁶⁵.

The Thermocalc software package allows the user to combine both computational and experimental data to optimise thermodynamic parameters that describe each phase in a system of choice. The package allows these optimised parameters to then be used to model a phase diagram. The main thermodynamic parameters that have been used so far are parameters to model the Gibbs energy of formation and the Gibbs energy of interaction for each phase.

Before any thermodynamic parameters can be produced, the user must first gather what thermodynamic data they can find on the elements present in the system of interest. This information will include the standard phases of the elements, the atomic mass of the elements and their enthalpies and entropies of formation in their standard state. Once this information is entered, it can then be used in conjunction with thermodynamic data from experimental sources (such as heat capacities, enthalpies of mixing of the different components etc.) and from looking at other existing phase diagrams of the system, to estimate the required thermodynamic parameters of the different phases present within the system.

For a pure element in its standard state the Gibbs energy of formation will be zero. However, the phase diagrams used in this project deal with both stoichiometric and non-stoichiometric compounds. The thermodynamic parameters of these phases are made up of a series of functions that are used to describe the Gibbs energy over a range of

temperatures. The functions for these compounds tend to look like the equation below (E. Povoden-Karadeniz, Personal Communication), where A-F are model parameters that are fitted using experimental and already known phase diagram data.

$$\Delta^{\circ}G = A + BT + CT \ln T + DT^2 + ET^3 + FT^{-1} \quad (2.35)$$

The function is derived from the Gibbs energy equation $\Delta G = \Delta H - T\Delta S$ which can be broken down into:

$$\begin{aligned} \Delta S &= -\left(\frac{\partial G}{\partial T}\right) = -B - C(1 + \ln T) - 2DT - 3ET^2 + FT^{-2} \\ \Delta H &= \Delta G + T\Delta S = A - CT - DT^2 - 2ET^3 + 2FT^{-1} \\ C_p &= \left(\frac{\partial H}{\partial T}\right) = -C - 2DT - 6ET^2 - 2FT^{-2} \end{aligned} \quad (2.36-2.38)$$

The fitting of the model parameters is undertaken by a module of the software known as the Parrot module. This module takes the information from an experimental data file and uses it to optimize the model parameters. The optimization is conducted by taking the values from the experimental database (e.g. enthalpy of formation of a phase etc.) and varying parameters A-F so that the relevant parameters match these values. However, parameters A-F may be present in more than one function, as such, the value of A that is correct for one function may not be correct for a different function, and so the values of the optimized parameters will not be 100% accurate. The software tries varying these values so that the sum of the root square of the errors is as small as possible. By using this method, the software module should calculate the model parameters to a value that is of an acceptable accuracy. Once the optimization is

completed, the user will use the Thermocalc program to calculate and display the phase diagram that is described by these parameters and functions. It is then recommended that the user has a second phase diagram of the system that can be compared to the calculated phase diagram. When the user compares the diagrams they can then notice if the optimized parameters are causing any errors resulting in causing the calculated phase diagram to have phase transition points which are inconsistent with the experimentally known phase transitions. If this is the case then the parameters can undergo several more rounds of optimization (changing which parameters are to be optimized e.g. only the parameters that are present to describe a liquid phase etc.) until the phase diagram appears to be correct, with the calculated diagram having phase transition points which match the known phase transitions for the system under investigation.

Of course the phase diagrams will not only contain solid stoichiometric and non-stoichiometric compounds but also other phases like liquids or gases. The functions that are used to describe liquid and gas phases have the same basic structure as the functions used to describe the solid compounds (see the function described above). The overall liquid parameter however will usually both contain the functions for the liquid as well as the addition of the functions for the solid of the same compound. These liquid and gas functions will undergo the same optimization process using known experimental data as the solid compounds.

The interaction energy also has a formula that is similar for solids and liquids. The interaction energy exists due to the fact that phases are described by placing their different components into sub lattices (e.g. CeO_2 contains a Ce^{4+} ion on one lattice and

two O⁻² ions on a second lattice). The atoms/ions in each sub-lattice can then interact with each other, causing a change in energy. The program will by default use a Redlich-Kister expression⁶⁶ to model the excess energy. This expression shows how a binary interaction parameter may change as a result of composition. This expression is written as:

$$X_a X_b (L_0 + L_1 (X_a - X_b) + L_2 (X_a - X_b)^2 + L_3 (X_a - X_b)^3 + \dots) \quad (2.39)$$

Where X_a and X_b are fractions of the constituents a and b respectively, and the binary L parameters are functions of temperature and pressure. This can be generalised into a formula that has the general form $A + B \cdot T$ where A and B are again model parameters that will be optimized.

Once these optimizations are completed and the user is satisfied that the phase diagram is of sufficient accuracy, the parameters can be saved in a database file that can be opened by anyone with access to the file, allowing multiple people to replicate phase diagrams without having to enter all the thermodynamic data themselves.

These databases can vary in size from the very small, containing only 2 -3 elements, to very large ones containing 20 +. In this project the database will be created by combining a few smaller mini databases into one larger database containing all of the phases that can be included in the Ce-Cu-O system.

Chapter 3 – Investigation of the Thermodynamic Properties of Copper Doped Ceria

3.1. Aim

The aim of this project is to investigate the thermodynamics of copper doped ceria. We will look at how this material fits into a phase diagram of the Ce-Cu-O system and how this system changes under different atmospheric conditions. We will also investigate the atomic makeup of the system in order to determine the oxidation states of the atoms present within the material and the formation of vacancies.

3.2. Creation of Starting Thermodynamic Database

In order to create a database of thermodynamic properties for our system we will first look at the binary Ce-O and Cu-O systems and identify how these should be expanded to accommodate our new mixed phase. Phase diagrams and thermodynamic databases were found to already be available for both of the binary systems. The Ce-O system had previously been modelled by Zinkevich et al.⁶⁷ The thermodynamic database proposed by them results in the phase diagram as shown in figure 20. The most relevant phase for us being the CeO_{2-x} fluorite phase which has a melting temperature of 2500K. The Cu-O system is described by Schramm et al.⁶⁸. This database crucially contains information about the CuO and Cu_2O phases (Figure 21), showing their melting temperatures. The parameters and phase descriptions used in the creation of these two binary systems were brought together to create a starting database which we could then expand to include descriptions of any ternary phases.

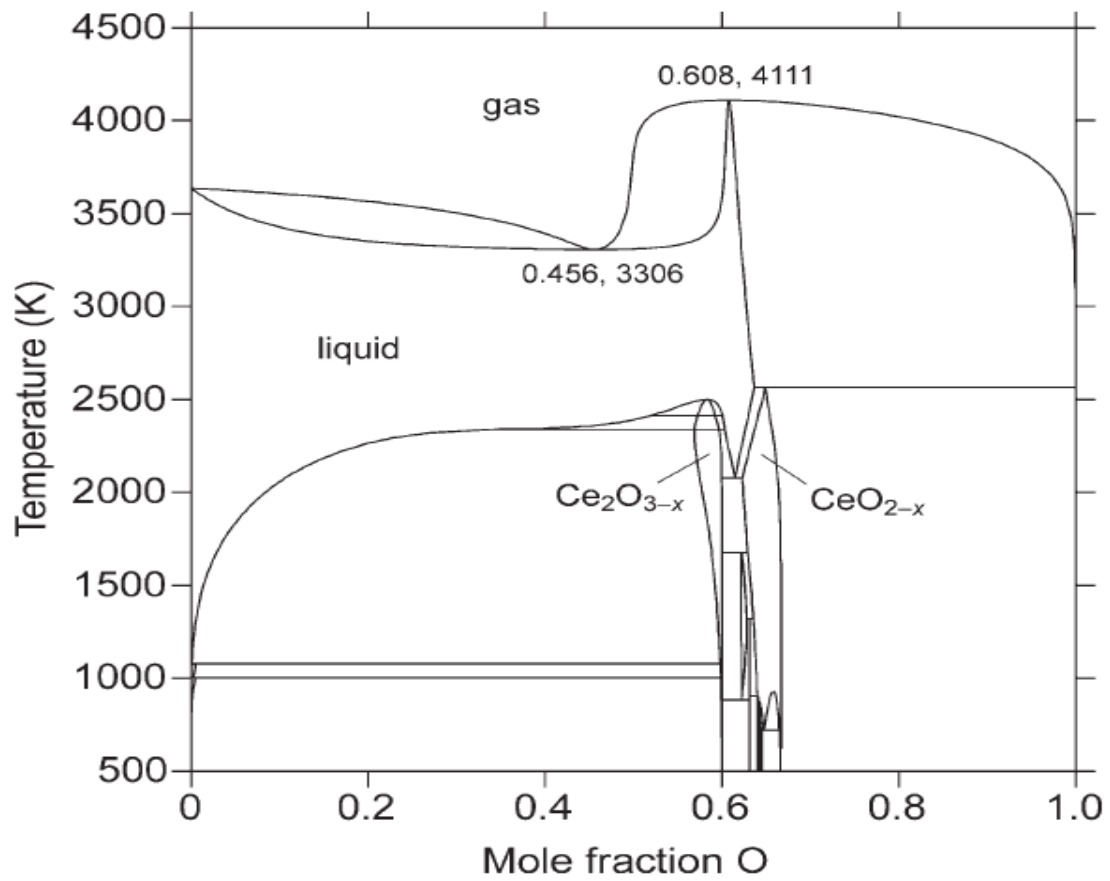


Figure 20. The Phase Diagram of the Ce-O system as predicted by Zinkevich et al.⁶⁷

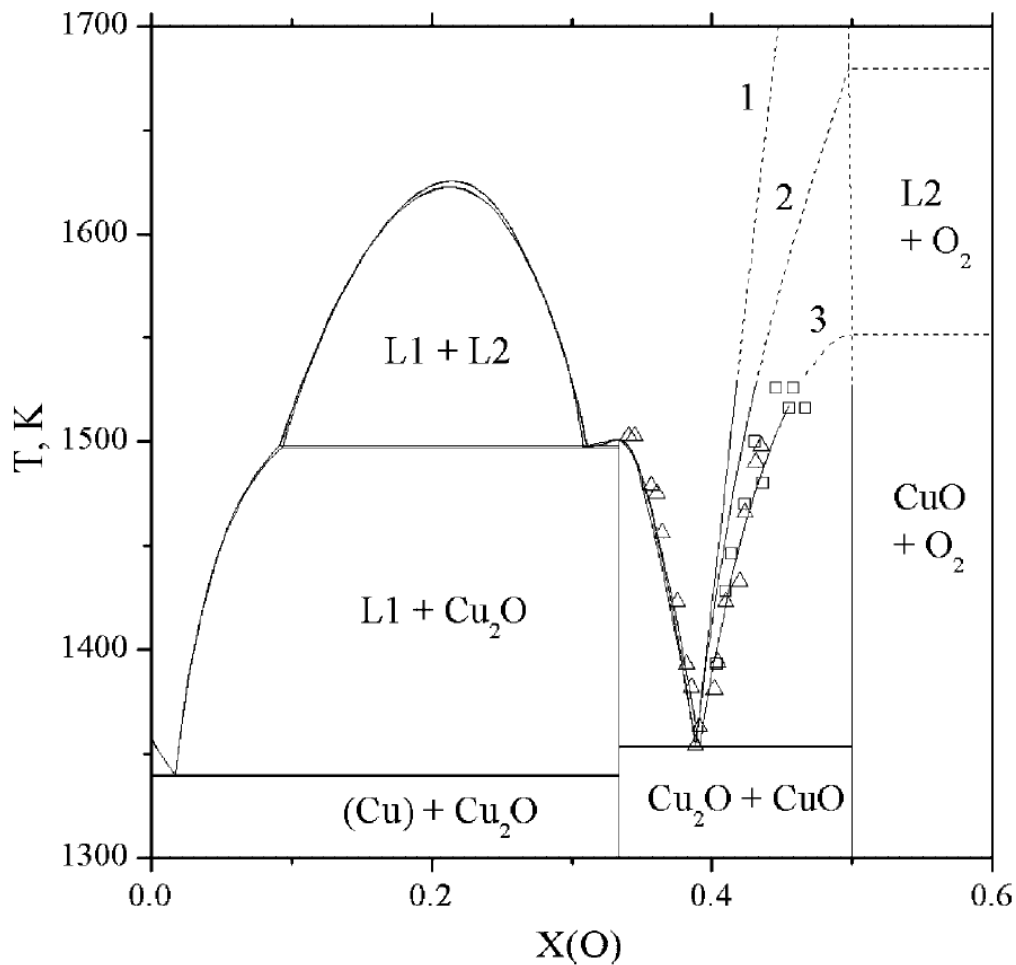


Figure 21. The Phase Diagram of the Cu-O system as predicted by Schramm et al.⁶⁸

3.3. Thermodynamic Modelling of the Copper Doped Ceria Phase

The main phase of interest in this project is the fluorite based copper doped ceria phase. This ternary phase is based upon the expansion of the CeO₂ fluorite phase as described by Zinkevich et al⁶⁷. The fluorite phase can be described using the Compound Energy Formalism (CEF)⁶⁹. In the CEF of oxide phases ions and vacancies are defined as distinct species which occupy the most energetically favourable positions in the crystal lattice. This allows the structure to be split up into separate sub-lattices. The metallic ions will sit on sites that are different from those of the light non-metallic element of

oxygen in this case. For the copper doped ceria phase this sub lattice model was expanded to provide the model $(Ce^{3+}, Ce^{4+}, Cu^{2+}, Cu^{1+})_2(O^{2-}, Va)_4$ where the parentheses separate the two different sub-lattices. The first sub-lattice contains the metallic species, while the second contains the oxygens and vacancies. The Gibbs energy of this fluorite phase G_m^{FL} is given by equation (3.1) (Equation derived by E. Povoden-Karadeniz, Personal Communication). This equation is obtained by combining the energies of all of the possible “end members” $(Ce^{3+})_2(O^{2-})_4$, $(Ce^{3+})_2(Va)_4$, $(Ce^{4+})_2(O^{2-})_4$, $(Ce^{4+})_2(Va)_4$, $(Cu^{2+})_2(O^{2-})_4$, etc. (Here the term end members refers to the compounds which exist at the compositions which exists at the extreme ends of the composition spectrum) , the entropies of ideal mixing between different species on the same sub lattice (RT-terms in Eq. (3.1) with fractions of species i in the sub lattice, y_i), and the energy of non-ideal mixing, ${}^E G_m^{FL}$

$$\begin{aligned}
G_m^{FL} = & {}^{\circ}G(FL, Ce^{3+} : O^{2-})y_{Ce^{3+}}^{z1}y_{O^{2-}}^{z2} + {}^{\circ}G(FL, Ce^{4+} : O^{2-})y_{Ce^{4+}}^{z1}y_{O^{2-}}^{z2} \\
& + {}^{\circ}G(FL, Cu^{1+} : O^{2-})y_{Cu^{1+}}^{z1}y_{O^{2-}}^{z2} + {}^{\circ}G(FL, Cu^{2+} : O^{2-})y_{Cu^{2+}}^{z1}y_{O^{2-}}^{z2} \\
& + {}^{\circ}G(FL, Ce^{3+} : Va^0)y_{Ce^{3+}}^{z1}(1-y_{O^{2-}}^{z2}) + {}^{\circ}G(FL, Ce^{4+} : Va^0)y_{Ce^{4+}}^{z1}(1-y_{O^{2-}}^{z2}) \\
& + {}^{\circ}G(FL, Cu^{1+} : Va^0)y_{Cu^{1+}}^{z1}(1-y_{O^{2-}}^{z2}) + {}^{\circ}G(FL, Cu^{2+} : Va^0)y_{Cu^{2+}}^{z1}(1-y_{O^{2-}}^{z2}) \\
& + aRT(y_{Ce^{3+}}^{z1} \ln y_{Ce^{3+}}^{z1} + y_{Ce^{4+}}^{z1} \ln y_{Ce^{4+}}^{z1} + y_{Cu^{1+}}^{z1} \ln y_{Cu^{1+}}^{z1} + y_{Cu^{2+}}^{z1} \ln y_{Cu^{2+}}^{z1}) \\
& + bRT(y_{O^{2-}}^{z2} \ln y_{O^{2-}}^{z2} + (1-y_{O^{2-}}^{z2}) \ln(1-y_{O^{2-}}^{z2})) \\
& + {}^E G_m^{\Phi}
\end{aligned} \tag{3.1}$$

${}^E G_m^{FL}$ Describes the excess Gibbs energy of non-ideal mixing which is the energy change caused by the interactions of two or more different elements (or the differently charged ions of the same type), when those elements are on the same sub-lattice, and can be given by equation (3.2).

$$\begin{aligned}
{}^E G_m^{FL} = & \sum_i \sum_{j>i} y_i^{s1} y_j^{s1} \left[\begin{aligned} & y_{O^{2-}}^{s2} \left(\sum_{v=0}^2 (y_i^{s1} - y_j^{s1})^v {}^v L_{i,j;O^{2-}}^\phi \right) \\ & + y_{Va^0}^{s2} \left(\sum_{v=0}^2 (y_i^{s1} - y_j^{s1})^v {}^v L_{i,j;Va^0}^\phi \right) \end{aligned} \right] \\
& + y_{O^{2-}}^{s2} y_{Va^0}^{s2} \sum_i y_i^{s1} \left(\sum_{v=0}^2 (y_{O^{2-}}^{s2} - y_{Va^0}^{s2})^v {}^v L_{i;C,Va^0}^\phi \right)
\end{aligned} \tag{3.2}$$

Here ${}^v L$ are linearly temperature-dependent parameters with interaction exponents v . L -parameters describe excess interaction energies between metallic species i and metallic species j on the cationic sublattice, or O^{2-} , Va on the interstitial sublattice. The non-ideal interactions of more than two species have not been considered within this project.

3.4. Cation and Vacancy Modelling of the Copper Doped Ceria Phase using reciprocal Relations

The substitution of cerium with copper within the same sub lattice causes a problem for the structure of the Fluorite phase in the form of charge defects. The replacement of a Ce^{4+} or Ce^{3+} with a Cu^{1+} or Cu^{2+} causes the previously neutral fluorite structure to become negatively charged. To resolve this charge imbalance, oxygen ions are removed from the lattice to form vacancies. When we have information regarding the composition of the structure as a function of temperature, composition and oxygen partial pressures, we can use this information to predict defect chemistry via the use of CALPHAD modelling.

In order to model the Gibbs energy contributions to the fluorite phase of Cu-doped CeO_2 , the strategy of using reciprocal relationships within the compound energy formalism has been used. Figure 22 shows the composition square for the copper based

end-member compounds along with mixed neutral compounds N and NB which are located at the end of the neutral line.

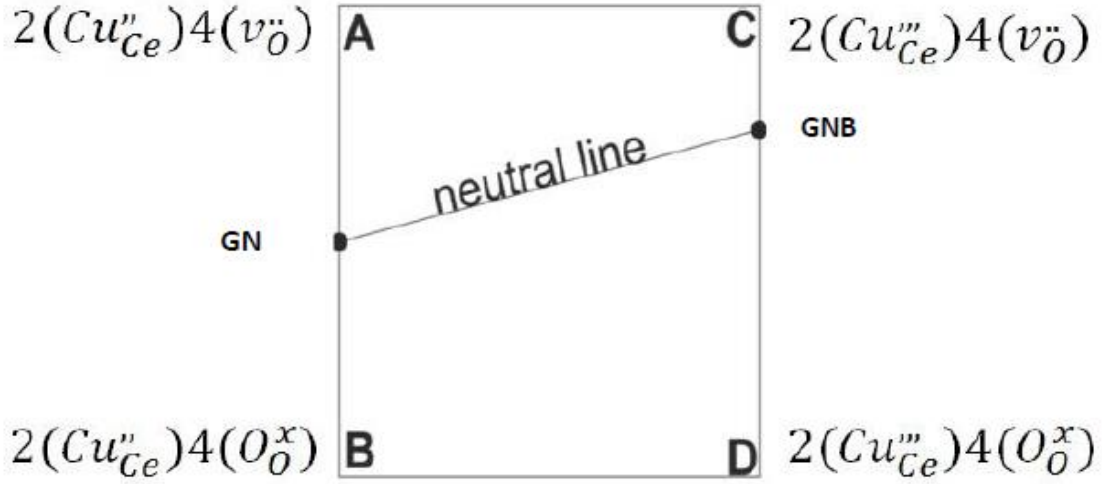


Figure 22. The composition square of the copper doped end-members of the fluorite phase. The end members are represented in the form of Kröger-Vink notations.

The Gibbs energies of the charged end-member compounds can be related to each other and the neutral compounds via the use of three different relations. The first relationship is:

$$G(A)+G(D)=G(B)+G(C), \quad (3.3)$$

Which assumes a smooth Gibbs energy surface among the end members A-B-C-D of the fluorite phase, with the least probability for demixing. The second relationship is:

$$G(N)=\frac{1}{2}G(A)+\frac{1}{2}G(B), \quad (3.4)$$

Where $G(N)$ is the Gibbs molar energy of the neutral structure situated half way between end members A and B

and the third relationship is:

$$G(\text{NB}) = \frac{1}{4}G(\text{C}) + \frac{3}{4}G(\text{D}). \quad (3.5)$$

Where $G(\text{NB})$ is the Gibbs molar energy of the neutral structure NB which sits between charged end members C and D.

By setting one of the end members as a fixed “reference” (this is typically a highly charged hypothetical compound; in our case the most highly charged end-member $2\text{Cu}^{1+}4\text{O}^{2-}$ was used). We can use computationally determined enthalpies and entropies of the neutral structures to optimise the variables of the Gibbs energy equations of the charged end members.

As well as determining the thermodynamic properties of the neutral structures, we must also determine the thermodynamics of mixing within the Ce-Cu phase in order to ensure proper modelling of the excess Gibbs energy of non-ideal mixing, and related phase boundaries.

In order to model the energy of non-ideal mixing we therefore decided to analyse the mixing thermodynamics of 25%, 50% and 75% Cu-doped ceria via the use of DFT, and to use the results for adjustment of parameters within the Compound Energy model of the fluorite solid solution.

3.5. Test Calculations

Before first principles calculations were carried out on our target material we first conducted test calculations to determine a suitable functional for use in the calculations. We chose to use CuO and Cu₂O as test materials as they have known experimental enthalpies and entropies that will allow us to compare our results. The accuracy of calculations intended to find the enthalpy of the materials was first tested. In order to

find the enthalpy we would need to find the ground state energy of CuO and Cu₂O and subtract the ground state energy and Zero Point Energies of their component atoms Cu and O (in the case of O, an O₂ molecule was used and the given energies halved). The enthalpy predicted during these calculations are for the materials at a temperature of 0 K; experimental enthalpies at finite temperature are expected to be higher. The zero point corrections of the solids were calculated from a Hessian based on the finite displacement method. The vibrational energy of O₂ was based on analytic second derivatives as calculated by Gaussian.

The ground state energies of CuO, Cu₂O, O₂, and Cu metal were calculated using first principles methods. In particular the energies were calculated by conducting geometry optimizations using Density Functional Theory (DFT). The computational package used was the VASP⁵⁸⁻⁶⁰ package which uses plane-wave basis sets. In the case of CuO and Cu₂O both the atomic positions and cell size were optimized using an increasing K point grid until the cell size changed by no more than 0.01 angstroms and the atomic positions moved by no more than 0.001 Angstroms. This led to a 23x23x23 grid being used for the PBE calculation, and a 3x3x3 grid being used for the HSE and B3LYP calculations. In the case of Cu metal only the cell size was optimized, and in the case of O₂ only the atomic positions were optimized in a cell of 10x10x10 angstroms. An energy cut off of 500 eV was used for all calculations which is a higher cut-off than the “accurate” setting in VASP for most atoms. The Projector augmented wave set of pseudopotential⁷⁰ were used for all VASP calculations.

Molecule	Calc. PBE (eV)	Calc. B3LYP (eV)	Calc. HSE (eV)	Reported PBE (eV)	Reported HSE (eV)	JANAF (eV)
CuO	-1.22	-1.14	-1.43	-1.23	-1.44	-1.60
Cu ₂ O	-1.25	-1.12	-1.55	-1.28	-1.62	-1.76

Table 1. Table showing the results on enthalpy calculations using the functions PBE, B3LYP and HSE in comparison to data reported by Emily Carter⁷¹ and data reported in the JANAF tables⁷².

The resultant energies were compared to previous computational data reported by Emily Carter⁷¹ and enthalpies reported in the JANAF tables. It was found that the B3LYP functional gave the worst results in comparison to experiment, underreporting the energy by 0.46 eV in case of CuO and 0.64 eV in the case of Cu₂O. This was followed by the PBE functional which underreported the energy by 0.38 eV in the case of CuO and 0.51 in the case of Cu₂O. The PBE results were also compared to the PBE calculations previously recorded by Emily Carter⁷¹ and were shown to be within a margin of 0.03 eV. HSE was shown to obtain the closest energy with a difference compared to experiment of 0.17 eV for CuO and 0.21 eV for Cu₂O. In the case of HSE we do see a larger difference between our computed results and the results of Carter⁷¹. These differences are likely due to their use of a larger supercell and higher energy cut off.

After deciding on the use of the HSE functional for geometry optimizations relating to enthalpy calculations, the method for the entropic calculations was then tested. For our

entropic calculations we are using a 2x2x2 supercell based upon the HSE optimized geometry. Due to computational timescales of such calculations, the PBE functional was used for the phonon calculations, with a 9x9x9 KPoint grid and a 500 eV cut-off. The calculations were set up with the help of the Phonopy computational package which takes a VASP optimised structure and creates a perfect supercell allowing for the use of the DFPT phonon calculation method and supercells with displaced atoms for use with the Finite Displacement phonon calculation method. The calculations were run in VASP and the results analysed with the Phonopy package to produce entropies at different temperatures. The entropies for a temperature of 300 K were compared to entropies reported in the JANAF tables.

Molecule	DFPT (J K ⁻¹ mol ⁻¹)	Finite Displacement (J K ⁻¹ mol ⁻¹)	JANAF (J K ⁻¹ mol ⁻¹)
CuO	45.34	42.86	42.85
Cu ₂ O	N/A	91.61	92.7

Table 2. Table showing the resultant entropies from phonon calculations in comparison to the JANAF tables.

It was shown that for the Finite displacement method the calculated entropy for CuO was within 0.01 J K⁻¹ mol⁻¹ of experiment and for Cu₂O was within 0.9 J K⁻¹ mol⁻¹ of the experimental value. This was better than the DFPT method which was within 2.49 J K⁻¹ mol⁻¹ of experiment for CuO (The DFPT calculation for Cu₂O failed). Given these results the Finite displacement method was chosen for use in all further entropic calculations.

3.6. Calculations Relating to Neutral Structures

Three different oxidation states of Copper were investigated in relation to their doping ability. The three states investigated were Cu^{1+} , Cu^{2+} , and Cu^{3+} . The first step in the investigation of these oxidation states was to conduct a geometry optimization of a fluorite unit cell containing 4 cerium atoms and 8 oxygen atoms (This optimization was carried out using HSE with a 5x5x5 Kpoint grid and an energy cutoff of 500eV). Once this unit cell had been optimized all of the cerium atoms were replaced with copper atoms. In each of the neutral structures the doped Cu will be entirely composed of either Cu^{1+} , Cu^{2+} or Cu^{3+} with no mixing of the oxidation states. We can mimic these oxidation states by the removal of oxygens from the structure. In the case of Cu^{1+} , 6 oxygens are removed, when Cu^{2+} is mimicked, 4 oxygens are removed, and finally when Cu^{3+} is mimicked 2 oxygens are removed. In all cases the oxygens were removed systematically in a way to reduce the amount of instances where the removed oxygens were adjacent to each other in order to reduce the amount of destabilising vacancy-vacancy interactions. From this system one structure was produced each for Cu^{1+} and Cu^{2+} while three possible structures were generated for Cu^{3+} . With the structures generated, initial geometry optimizations were carried out on each structure. As these neutral structures are unphysical, the optimizations produced results in which the fluorite structure of the unit cell was lost. In order to resolve this problem we chose to optimize only the unit cell volume and freeze the atomic positions in relation to their fractional coordinates. The volume calculations were carried out using HSE with a 5x5x5 K-Point grid and an energy cutoff of 500 eV. With these optimizations we were then able to calculate an initial energy for each of the neutral structures, which we

would then be able to convert into enthalpies (in the case of Cu^{3+} the unit cell with the lowest energy was carried forward for use, with the other two being discarded).

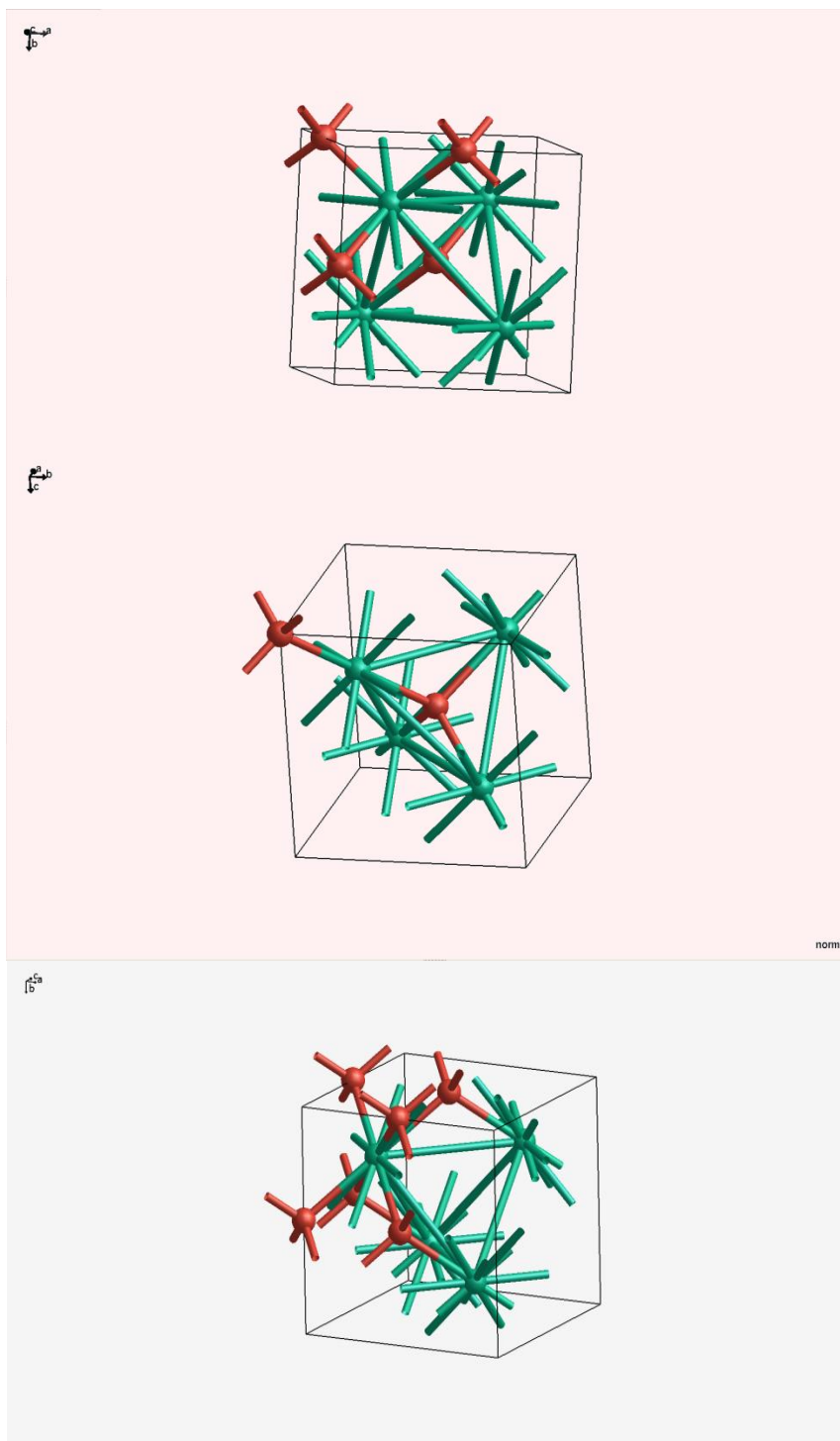


Figure 23. The minimal energy neutral end-member structures for Cu^{2+} (top), Cu^{1+} (middle), and Cu^{3+} (bottom) doped ceria. The green atoms are copper while the red atoms are oxygen.

The conversion of these energies into enthalpies requires the use of the following equation:

$$H = E_{\text{tot}} - E_{\text{comp}} + E_{\text{ZPC}} \quad (3.6)$$

Where E_{tot} is the energy of formation of the unit cell, E_{comp} is the energy of the sub components of the unit cell in their elemental states (in our case the energy of 4 x a copper atom in the bulk metal + 2/4/6 oxygen atoms in O_2), and E_{ZPC} is a zero point correction. In order to do this we carried out geometry optimizations on a single copper atom representing the primitive unit cell of bulk copper, and on a molecule of oxygen in order to determine their energies. This leaves us with the problem of calculating the zero point correction. In order to calculate the zero point correction we carried out phonon calculations on 2x2x2 supercells of the neutral structures using the finite displacement method with the PBE functional and a 9x9x9 K-point grid. After carrying out these calculations we were then able to produce enthalpies for the formation of each of the neutral structures.

Neutral Compound	Enthalpy (J/mol/atom)
$\text{Cu}^{1+} - (\text{Cu}^{1+})_2(\text{O}^{2-}_1\text{Va}_3)$	-47106.1
$\text{Cu}^{2+} - (\text{Cu}^{2+})_2(\text{O}^{2-}_2\text{Va}_2)$	-31743.7
$\text{Cu}^{3+} - (\text{Cu}^{3+})_2(\text{O}^{2-}_3\text{Va}_1)$	-3809.19

Table 3. First-principles enthalpies of the Cu^{1+} , Cu^{2+} and Cu^{3+} neutral end-members of doped ceria.

From these calculations it was shown that the Cu^{1+} end-member had an enthalpy of -47106 J/mol/atom which is lower than the end-member Cu^{2+} which had an enthalpy of -31743 J/mol/atom, which makes the former more stable. The Cu^{3+} end-member was

shown to have an order of magnitude higher enthalpy of -3809.19 J/mol/atom. This indicates that Cu^{1+} would appear to be more stable than Cu^{2+} when doped into ceria, with the doping of Cu^{3+} being unlikely. As a result we chose to not include Cu^{3+} doping into the fluorite phase in our database. This explains why the composition square shown in figure 22 does not show any Cu^{3+} based end members.

3.7. Calculations Relating to Mixing Enthalpies

As the Gibbs energy equation for copper doped ceria includes non-ideal mixing terms the thermodynamics of mixing have to be predicted. In particular first principles methods were used in order to predict the enthalpies of formation of ceria doped with 25%, 50% and 75% copper. Based on our previous calculations of the enthalpies of the fully doped end members only calculations looking at ceria doped with either Cu^{1+} or Cu^{2+} were carried out. Similar to our previous calculations we started with an optimized unit cell of normal ceria and replaced a number of the ceria atoms with copper atoms, with the number of atoms replaced dependent on the doping percentage. The different oxidation states of copper were again mimicked by removing a corresponding number of oxygen atoms to neutralise the effective charge generated. In the case of ceria doped with 25% Cu^{1+} we had to use a 2x1x1 super cell in order to allow the appropriate number of oxygen atoms to be removed to neutralise the charge. The scheme used for the optimization of these structures was the same as in the fully doped neutrals structures, with only the volumes of the unit cells being optimized and atoms being fixed in relation to their fractional coordinates using the HSE functional with a 5x5x5 K-Point grid and an energy cutoff of 500 eV. In the case of the 50 % and 75% doped ceria multiple oxygen atoms are removed from the unit cell in order to neutralise the

charge. This results in several possible structures depending on the locations of the vacancies in relation to each other (vacancies being right next to each other vs being spread out). In these cases the structure with the lowest optimized energy was used in each case.

In the case of 75% Cu¹⁺ the decision was taken not to finish the optimization of the structure and to therefore not carry out any energy calculations on this structure. This decision was based upon the large computational resources required for calculation. It was felt that as the experimentally determined copper doping ability of ceria was significantly smaller than 75 %, that any errors in the modelling at this copper doping percentage would not have a great effect on the modelled phase diagram, and so the time investment in this calculation could not be justified.

Once the energies of each of the systems were calculated we again converted them into enthalpies using equation 6.

Copper species	Doping percentage	Enthalpy (J/mol/atom)
Cu ¹⁺	25 %	-69586.8
	50 %	-183591.7
	75 %	N/A
Cu ²⁺	25 %	-273976
	50 %	-161131.9
	75 %	-47332.3

Table 4. First-principles enthalpies of 25%, 50% and 75% copper doped ceria.

In Cu^{2+} doped ceria 25 percent doping is shown to have the lowest enthalpy of -273976 J/mol/atom. The enthalpy increased with a higher dopant concentration, reaching an enthalpy of -47332.3 J/mol/atom at 75 percent doping.

The Cu^{1+} doped sample shows a less negative enthalpy than Cu^{2+} at 25 percent doping while having a more negative enthalpy at 50 percent doping. This would suggest that while Cu^{2+} is initially more stable than Cu^{1+} , when larger amounts of copper are doped into ceria Cu^{1+} would become more likely to be doped into the structure over Cu^{2+} .

3.8. Other Sources of Thermodynamic Information

In the above first principles calculations we have produced data regarding the enthalpies of formation of the neutral compounds for Cu^{1+} and Cu^{2+} doped ceria which can be used to optimize variables related to the enthalpies of the charged end member structures. In order to ensure that the optimization of these variables is as accurate as possible we also decided to include experimental information regarding the phase transitions of copper doped ceria, as well as data regarding the site fractions of the different species within the Fluorite phase. This additional information would both allow the variables regarding enthalpy to be more accurately assessed and also allow variables regarding the entropies of the end member compounds to be assessed. The information used in this project comes from experiments carried out by other researchers in the Irvine group (A. Abdoun, Personal Communication). The first source of information is XRD data from samples of copper doped ceria calcined at 1350°C under both air and argon environmental conditions. This dataset shows that when fired under air, single phase copper doping can be obtained for up to 7% copper, with a secondary CuO phase appearing at samples with 8% or more copper doping. When fired under argon the

single phase can be obtained for up to 11% copper doping with a secondary Cu₂O phase appearing starting for 12% copper doped ceria. The researchers also obtained XPS data showing the relative levels of each oxidation state of copper and ceria in relation to the other oxidation states present.

	$Ce^{3+}/(Ce^{3+}+Ce^{4+})$	$Ce^{4+}/(Ce^{3+}+Ce^{4+})$	$Cu^{1+}/(Cu^{1+}+Cu^{2+})$	$Cu^{2+}/(Cu^{1+}+Cu^{2+})$
0 % Cu	36	63	/	/
2.5% Cu	38	62	54	45
5% Cu	35	65	59	41
7% Cu	29	71	38	62
10% Cu	31	69	27	73

Table 5. The results of the XPS experiments showing relative levels of each oxidation state type for copper and ceria (XPS is a surface sensitive technique so results may not fully describe sub-surface concentrations). Results provided by (A. Abdoun, Personal Communication)

3.9. Optimization of the Thermodynamic Parameters of the Copper Doped Ceria Phase

The parameters of the copper doped ceria phase (the fluorite phase) were optimized using the Parrot module of the Thermo-Calc software package. In the optimization of the Fluorite phase, parameters were added to the existing parameters of non-doped ceria for each of the end members involving copper, and interaction parameters for the mixing of copper and ceria on the same sub-lattice were added.

Four parameters have been added to database to represent the copper based end members. These parameters are:

G(FLUORITE,CU+2:O-2;0) 298.15 GN-0.66667*GNB+0.66667*GREF;,,,

G(FLUORITE,CU+2:VA;0) 298.15 GN+0.66667*GNB-0.66667*GREF;,,,

G(FLUORITE,CU+1:O-2;0) 298.15 GREF;,,,

G(FLUORITE,CU+1:VA;0) 298.15 1.33333*GNB-0.33333*GREF;,,,

The first parameter represents the $2\text{Cu}^{2+}4\text{O}^{2-}$ end member, the second parameter represents the $2\text{Cu}^{2+}4\text{Va}$ end member, the third represents the $2\text{Cu}^{1+}4\text{O}^{2-}$ end member and the fourth represents the $2\text{Cu}^{1+}4\text{Va}$ end member. These parameters rely on a combination of three user defined functions which can be related to the composition square shown in figure 22. By using the three relationships contained within the composition square we can assign a specific combination of functions to each end member in order to create their specific Gibbs energy parameter. These functions are GN, GNB, and GREF and are represented in the database as:

ent-sym fun GN 2.98150E+02 +2*GUSRCUO+V1+V2*T; 6.00000E+03 N

ent-sym fun GNB 2.98150E+02 +GUSRCU2O+V3+V4*T; 6.00000E+03 N

ent-sym fun GREF 2.98150E+02 +GUSRCU2O+3*GHSEROO+v20; 6.00000E+03 N

The function GN relates to the molar Gibbs energy of Cu^{2+} neutral structure shown in the composition square. This neutral structure consists of 2 Cu^{2+} and 2 O^{2-} ions. The functional form includes 3 main terms. The first term is 2*GUSRCUO. This term represents the Gibbs energy of formation of a CuO formula unit multiplied by two (this is obtained from the database of Schramm et al.⁶⁸). This term must then be altered due to the fact that even though the number of Cu^{2+} and O^{2-} ions is similar to the CuO phase, these atoms actually exist inside a fluorite like structure. To alter this Gibbs energy, terms 2 and 3 are added to the functional. Term 2 is the variable V1 which represents changes to the enthalpy of formation and term 3 is the variable V2 multiplied by the temperature which represents changes to the entropy. The functional GNB has a similar structure to the function GN but is related to the Gibbs molar energy of the Cu^{1+} neutral structure. This neutral structure consists of 2 Cu^{1+} and one O^{2-} ions. The first term represents the Gibbs energy of formation of a Cu_2O formula unit (this is obtained from database of Schramm et al.). Variables V3 and V4 are again used to alter the Gibbs energy of the function to represent the fact that these atoms are within a fluorite structure. The variable V3 represents changes to the enthalpy and variable V4 represents changes to the entropy. The function GNREF is used to set the $\text{Cu}^{1+}\text{O}^{2-}$ end member as a reference parameter and relies on the already published GSEROO function⁷³ which defines on the Gibbs energy parameter of oxygen, and on the GUSRCU2O function. In the setting of this reference we add together the GUSRCU2O function and three times

GSEROO function (This represents the formula we are using as base unit for the end member which is $2\text{Cu}^{1+}4\text{O}^{2-}$). After this we added 85000 to the enthalpy in order to make the end member unfavourable as we would expect from such an unphysical structure. 85000 was chosen as this was the enthalpy change required to change the fluorite phase from being stable to being metastable

With the functionals defined we then optimized variables V1 –V4. In the optimization of the variables V1-V4 we first have to set the variables to a starting value from which we can optimize. We decided that a good starting value for the variables would be one in which the Fluorite phase is allowed to exist as a metastable state in the tertiary diagram. This was achieved by manually adjusting the variables V1 and V3 and increasing them until a value was reached which allowed the fluorite phase to be destabilised so that it did not appear as a single phase in the diagram. Variables V2 and V4 were left at a value of zero. After setting these starting values, variables V1 and V3 underwent initial optimization. Variable V1 was optimized first, using the collected first principles enthalpy data of the Cu^{2+} neutral structure. The computed enthalpy of formation of the neutral structure was entered into the module in the form of an equilibrium equation. The module then runs the same equation using the value of variable 1 as the input enthalpy and compares the root mean square error between the value of the input enthalpy and the value calculated using V1. The module then iteratively changes the value of V1 until the value of the root mean square error between the input enthalpy and the enthalpy generated using V1 reaches a minimum. The same procedure is then carried out for variable V3 except that that enthalpy data related to the Cu^{1+} neutral structure is used instead of the Cu^{2+} neutral structure. After this initial optimization variables V2 and V4 were added to the optimization. Variable V1 was optimized again

with variable V2 being added to the optimization pass. During this second optimization pass the experimental XRD and XPS data were added as further input arguments in the form of further input equilibrium equations, with the phase boundary between the fluorite phase and the CuO and Cu₂O, and the site fractions present within the fluorite phase at the experimentally relevant temperatures being used as arguments respectively. Variable V1 and variable V2 were iteratively changed by the software in steps of 100000 followed by steps of 10000 for V1 and steps 1 for V2 until the root mean square error between the equilibrium calculations using the variables, and equilibrium calculations using the experimental and first principles data was minimized. The same procedure was then carried out for variables V3 and V4. After this a third optimization pass was carried out with all of the variables being optimized at the same time. These optimizations led to variables V1 and V3 being set to the values of 100000 and 70000 respectively and variables V2 and V4 both being set to a value of 5. With the end members parameters now being fully optimized we then created parameters for the enthalpies of mixing for the interactions between copper and ceria. A parameter was created for each different type of mixing (Cu¹⁺ with Ce⁴⁺, Cu²⁺ with Ce⁴⁺, Cu¹⁺ with Ce³⁺, and Cu²⁺ with Ce³⁺).

Unlike in the case of the end members, each of these parameters were given their own independent enthalpies and entropies to be optimized instead of being related to a function. In the case of any mixing involving Ce⁴⁺ the enthalpies of each parameter was optimized using their related mixing enthalpies calculated via the use of the first principles calculations, and entropies were optimized via the use of the experimentally acquired XRD and XPS data.

3.10. Optimization of the Thermodynamic Parameters of the Ceria Doped Copper Oxide Phases

After the optimization of the copper doped ceria phase a problem was observed in the tertiary phase diagram. In the obtained XRD spectra it was shown that at 1350 C we should see that the single phase copper doped ceria phase has a phase boundary with either CuO or Cu₂O depending on whether the system was created under air or under an argon environment, but in our phase diagram the fluorite phase shared a phase boundary with the liquid phase. This showed that in our model of the ternary system the CuO and Cu₂O phases were being destabilised in comparison to the observed system. This problem was fixed by considering the possibility of doping ceria into the copper oxide phases. During a search through literature a paper by T. Jan et al.⁷⁴ was found in which up to 6 % ceria was doped into copper oxide. The following parameters were added to the already existing copper oxide parameters in order to reflect the possibility of this doping and were optimized using the doping percentage information provided by this paper:

ent-param G(CU2O,CE+3:O-2;0) 2.98150E+02 GUSRCU2O-500000; 6.00000E+03
N

ent-param L(CU2O,CE+3,CU+1:O-2;0) 2.98150E+02 -1050000; 6.00000E+03 N

ent-param L(CU2O,CE+3,VA:O-2;0) 2.98150E+02 -600000; 6.00000E+03 N

ent-param L(CU2O,CE+3,CU+1,VA:O-2;0) 2.98150E+02 -600000; 6.00000E+03
N

ent-param G(CUO,CE+3:O-2;0) 2.98150E+02 -178002.39+275.159239*T
-44.965711*T*LN(T)-.010809208*T**2+1369987.3*T**(-1)+v30; 6.00000E+03 N

ent-param L(CUO,CE+3,VA:O-2;0) 2.98150E+02 +v31; 6.00000E+03 N

ent-param L(CUO,CE+3,CU+2:O-2;0) 2.98150E+02 +v32; 6.00000E+03

The addition of this doping to the copper oxide phases stabilised the phases in our phase diagram, allowing a more realistic phase boundary to be modelled.

3.11. Phase Diagrams of the Ce-Cu-O System

After the optimization of all variables, the phase diagrams for the Ce-Cu-O system under air and 1% oxygen were calculated in order to determine the maximum amount of copper that can be doped into the fluorite phase at equilibrium without formation of a secondary phase. The phase diagram produced under air conditions shows that stable single phase fluorite is initially stabilised at around 1500°C but that almost no copper can be doped into this phase at this temperature. As the temperature increases we see that the fluorite phase can dissolve an increased amount of copper. This amount of copper increases until the phase reaches a maximum stability at roughly 2000°C with a cation fraction of roughly 0.09 Cu.

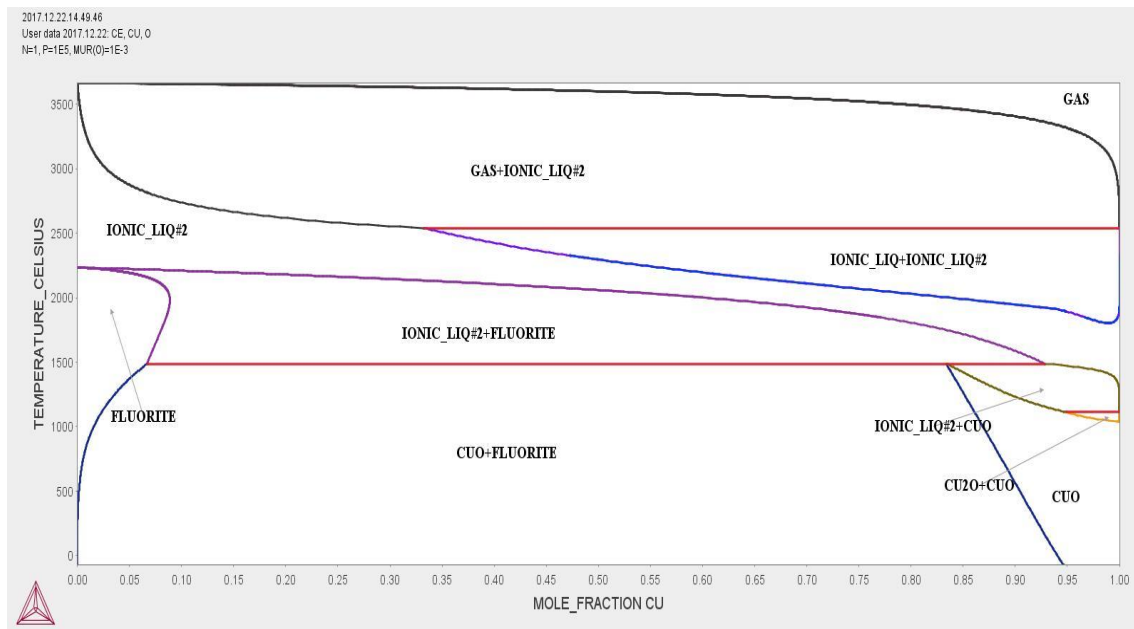


Figure 24. The phase diagram of the Ce-Cu-O system under Air (where the x-axis is cation fraction).

The phase diagram under 1% oxygen conditions shows a similar trend where single phase fluorite is initially stabilised at around 300°C with little copper content. Fluorite again shows increasing single phase stability with increasing temperature, with a maximum doping concentration being reached at 1615°C with a 0.07 cation fraction of Cu. After reaching this doping concentration, the concentration of copper then decreases slightly before increasing again to reach a cation fraction of 0.07 Cu at 2090°C.

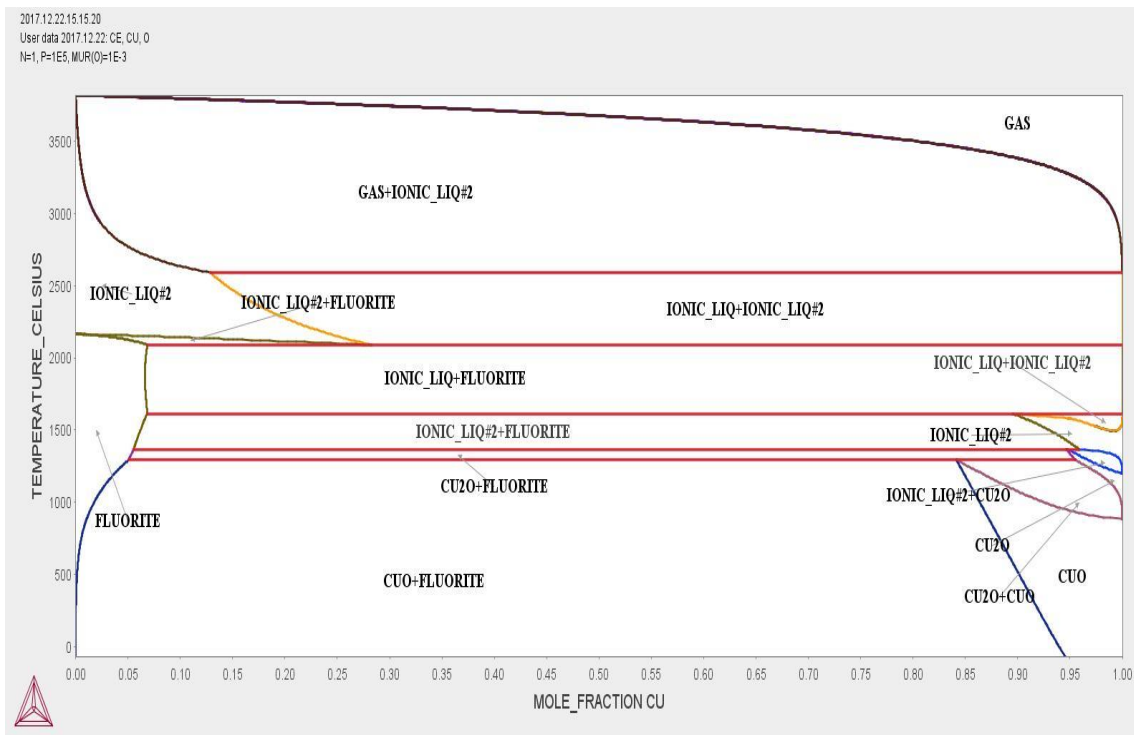


Figure 25. The phase diagram of the Ce-Cu-O system under 1% oxygen (where the x-axis is cation fraction).

Overall these phase diagrams show a general trend that there is an increasing stability of copper doped ceria with increasing temperature. However, literature sources report the production of single phase copper doped fluorite nanoparticles at low temperatures at higher mole fractions of copper than shown in the phase diagram (see table 6). From the results of this study we would propose that the single phase seen in these low temperature studies is in fact meta-stable, and that the catalytic ability of copper doped

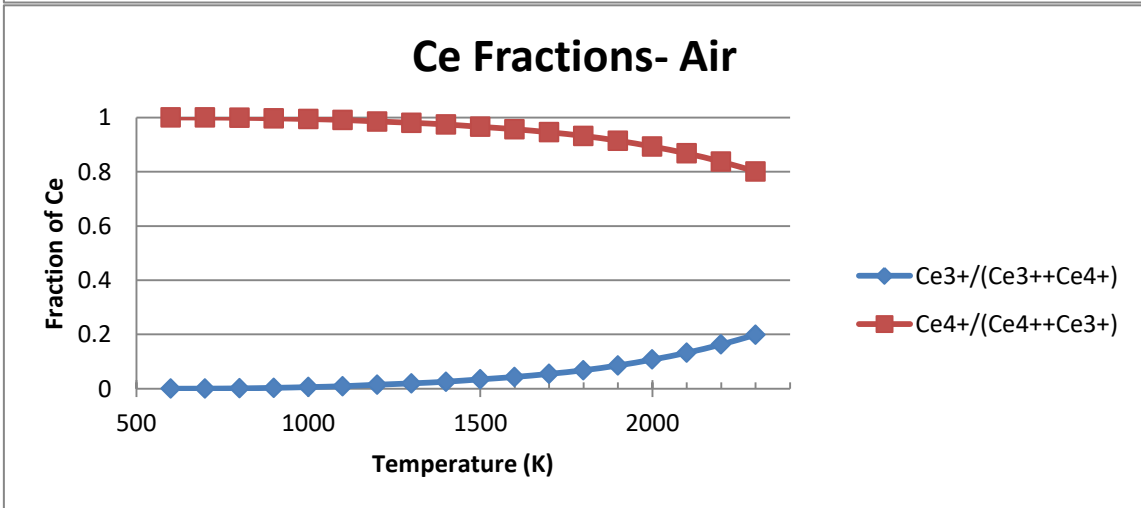
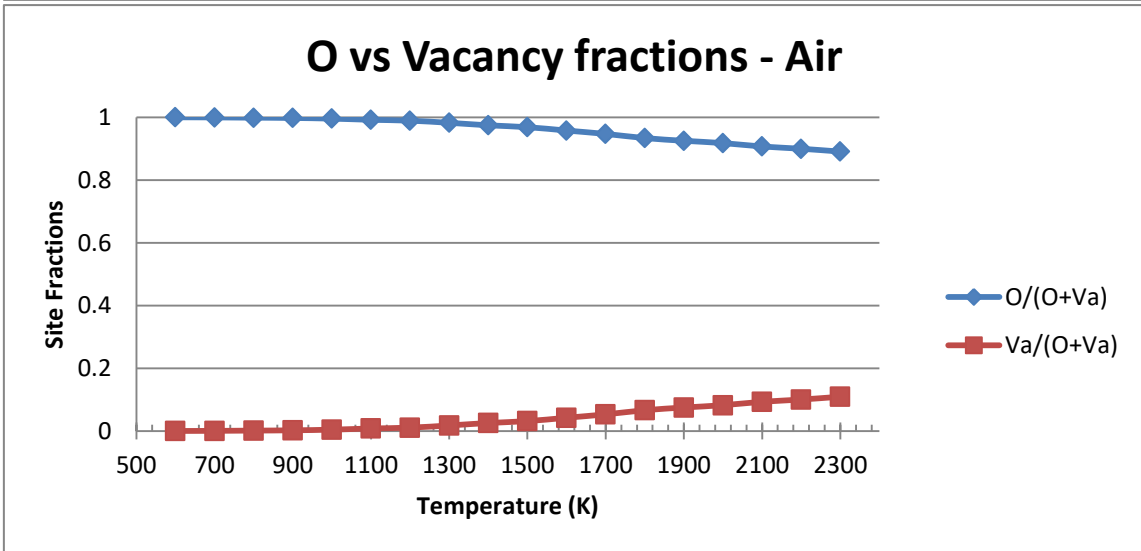
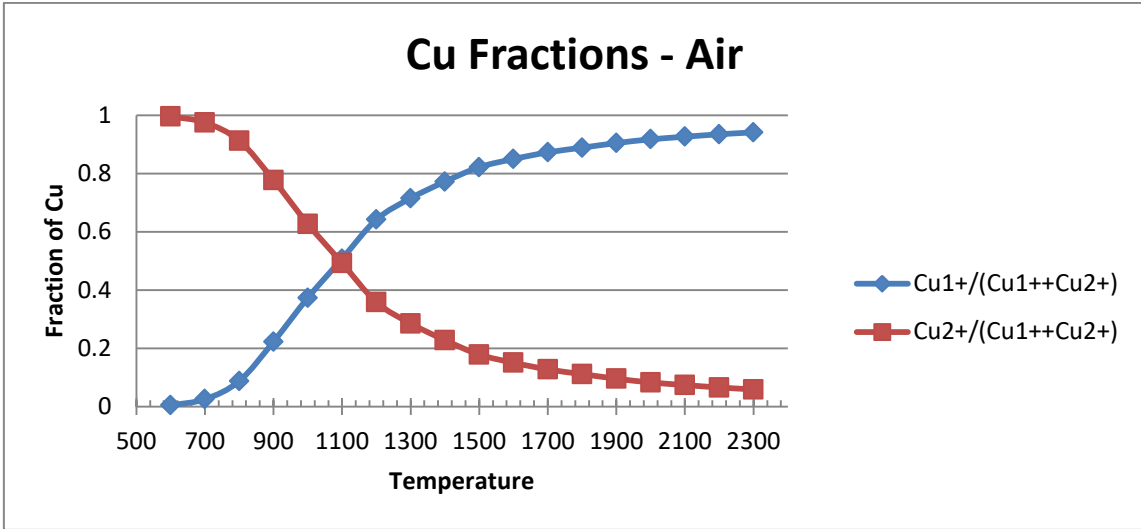
ceria shown in these literature sources is in part due to the metastability of the produced nanoparticles, which allows for the dispersion of copper along the surface of the material resulting in a larger surface area of copper being accessible.

Literature source	Reported maximum single phase (mole fraction of Cu at temp °C)
Horyn et al. ⁷⁵	0.03 at 980°C
Aunbamrung et al. ⁷⁶	0.1-0.2 at 500°C
Tschope et al. ⁷⁷	0.15 at 500°C and 550°C
Gamarra et al. ⁷⁸	0.022-0.116 at 500 °C

Table 6. A comparison between literature values and the maximum copper doping calculated via the produced phase diagram under air.

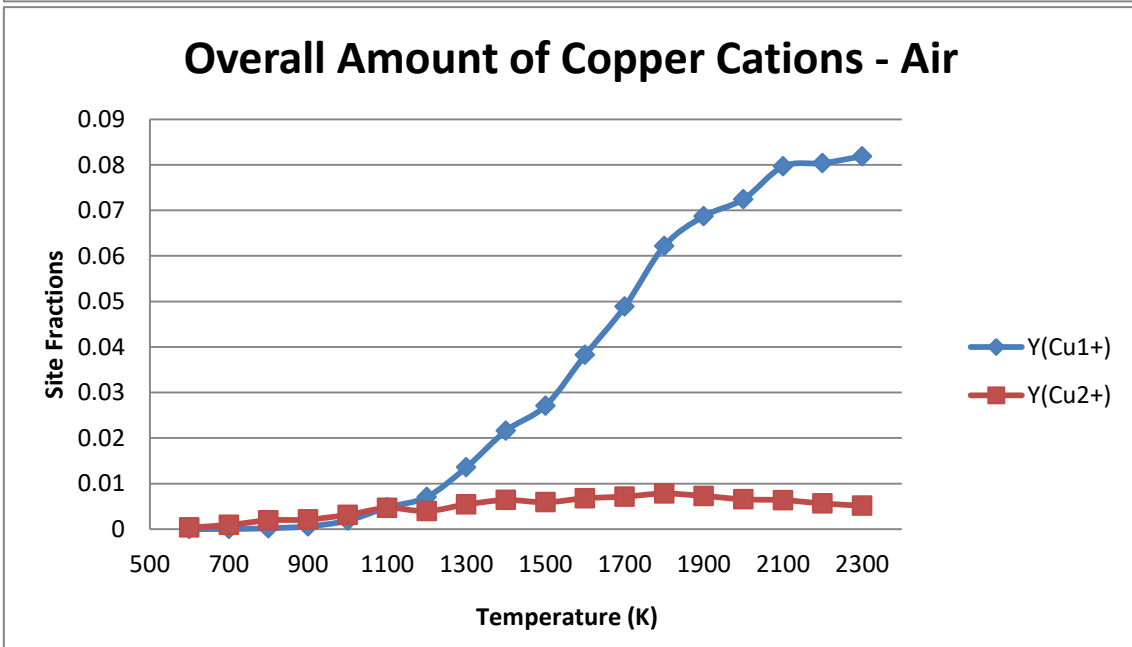
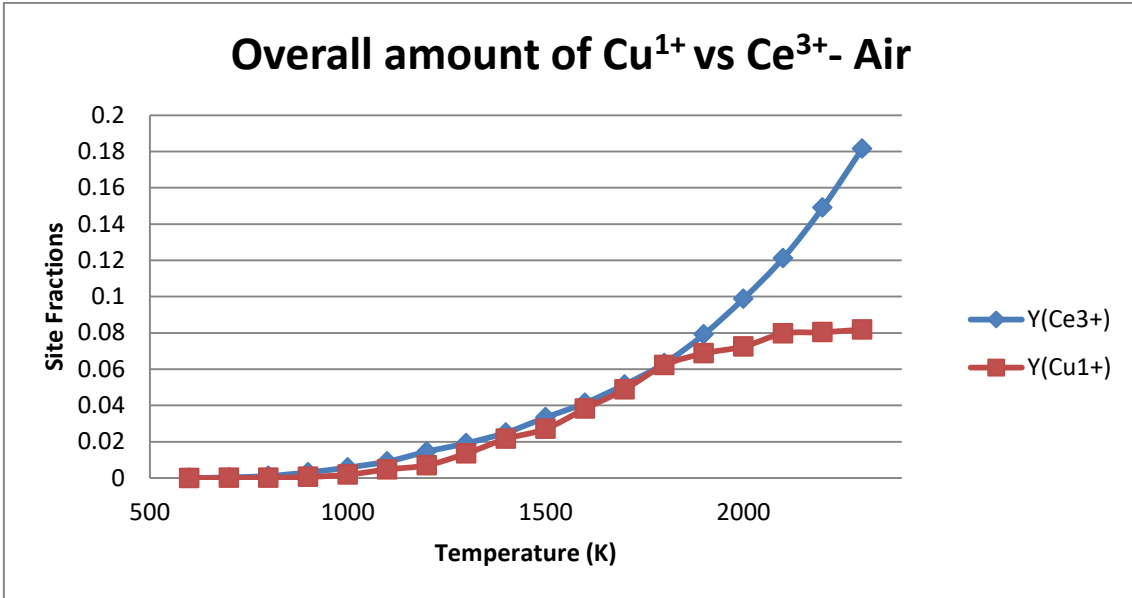
3.12. Site Fraction Study

In order to further understand the link between temperature and fluorite phase stability, we conducted site fraction studies in order to further determine the structure of the fluorite phase. In all studies we suspend (do not consider) all phases from the calculations carried out by the Thermo-Calc package, except for fluorite, and set the copper doping percentage in accordance with the maximum doping seen in the single phase in the relevant phase diagrams at each temperature point. In our first study we looked at site fraction occupancy versus temperature under air conditions.



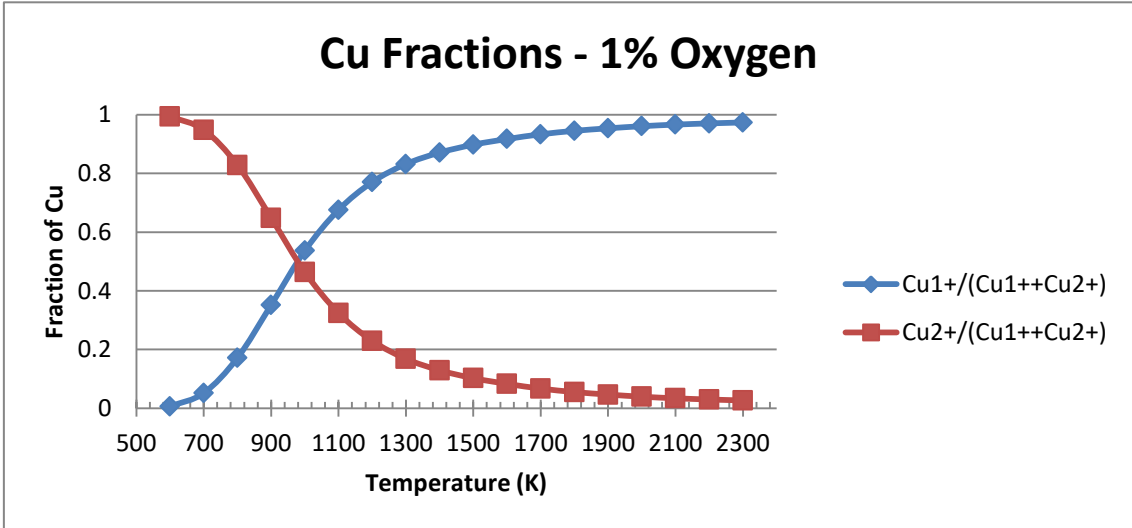
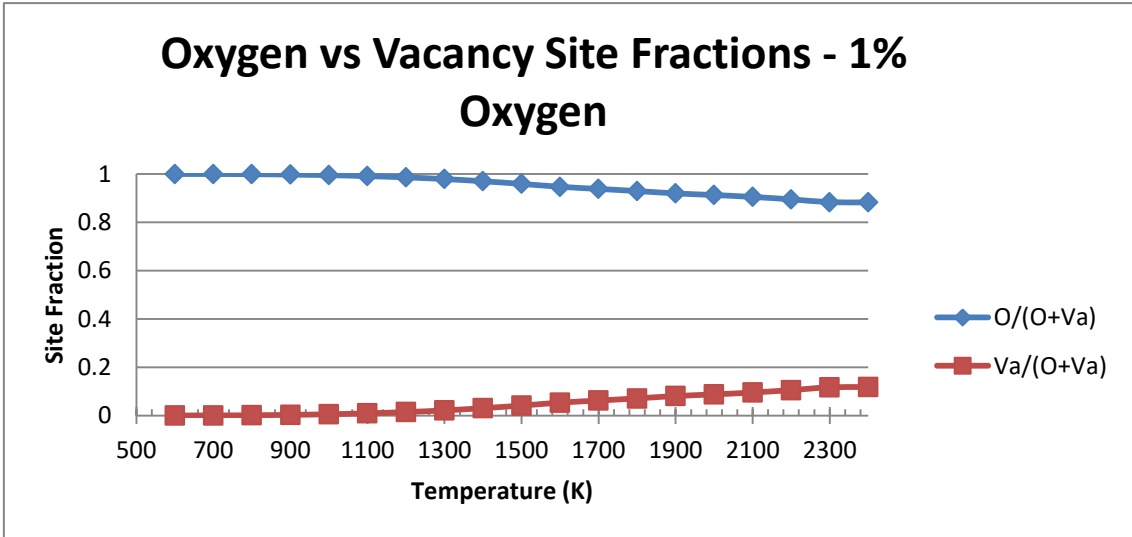
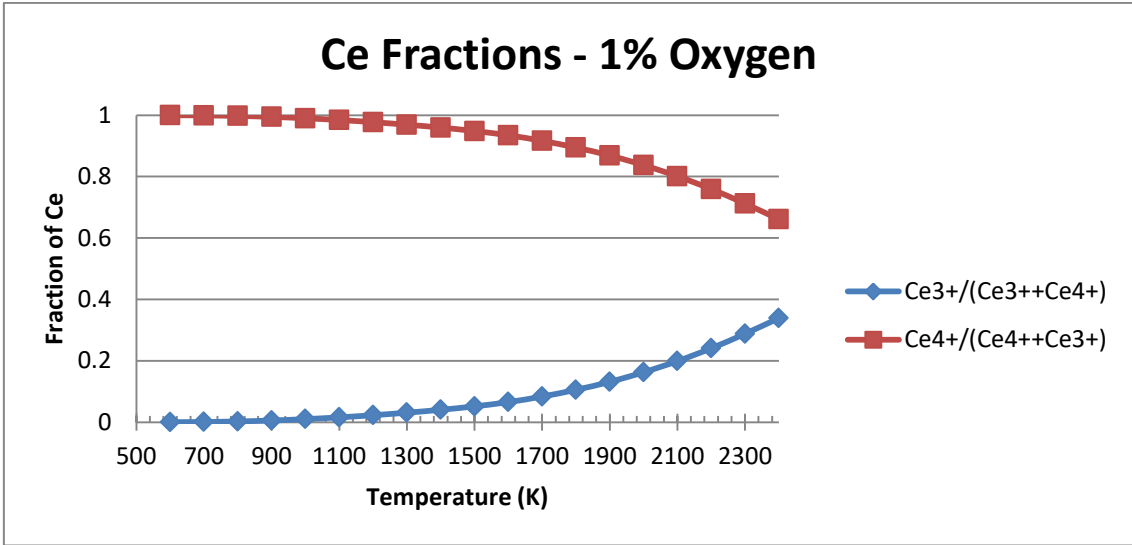
Figures 26-28. The relative fractions of $\text{Cu}^{1+}/\text{Cu}^{2+}$, $\text{Ce}^{3+}/\text{Ce}^{4+}$, and $\text{O}/\text{Vacancy}$ under air (Fractions are related to the maximum single phase doping seen in the air phase diagram at their relative temperatures).

We can see that below 1100K more Cu^{2+} is present, but that by 1200K Cu^{1+} becomes dominant. From the predicted overall doping amount of each oxidation state, we can see that this cross over is due to a large uptake of Cu^{1+} cations at higher temperatures, while the overall level of Cu^{2+} cations remains relatively stable. When we relate this to the relevant phase diagram, we can see that there is a correlation between increasing Cu^{1+} and increasing fluorite stability. This agrees with our first principles calculations, which showed that a Cu^{1+} doped fluorite unit cell was more stable than a Cu^{2+} doped unit cell.



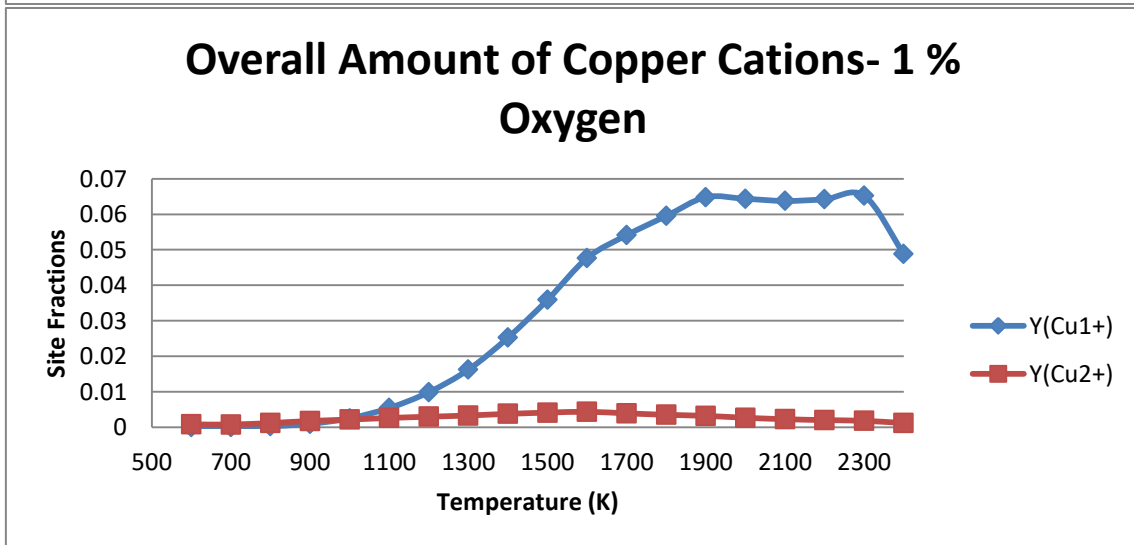
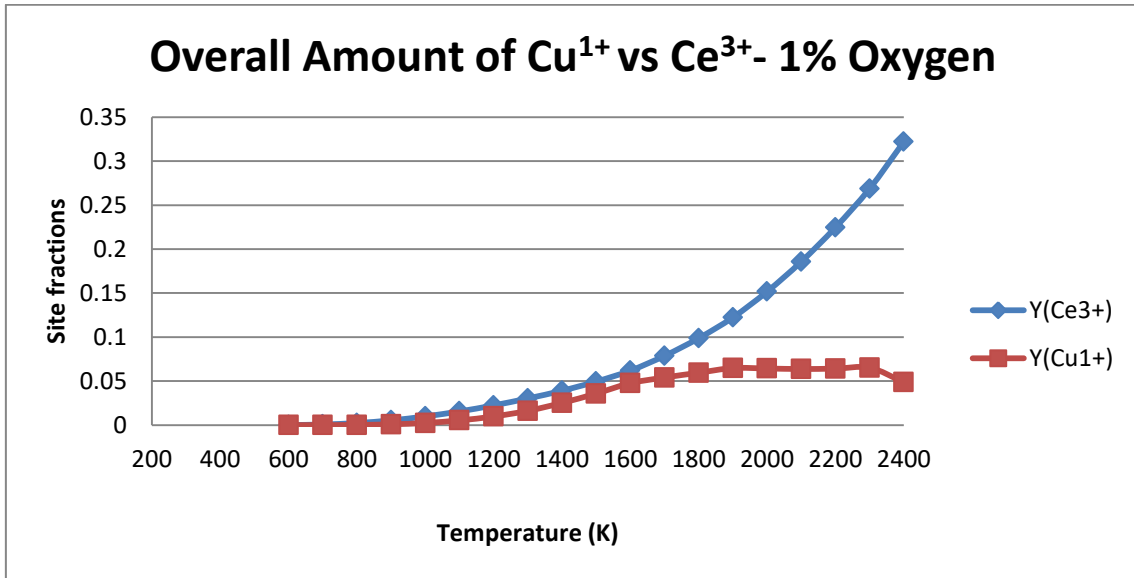
Figures 29-30. Amount of copper cations relative to each other and the overall amount of Ce^{3+} relative to Cu^{1+}

After determining the site fractions present when the phase was under air conditions we then tested the system under an atmosphere of 1% oxygen.



Figures 31-33. The site fractions of Cu¹⁺/Cu²⁺, Ce³⁺/Ce⁴⁺, and O/Vacancy under 1% oxygen

When under a 1% oxygen environment we see that Cu^{1+} becomes dominant over Cu^{2+} between 900K and 1000K which is roughly 100K less than in Air. We also see that the rate of Ce^{3+} formation increases so that the overall fraction of Ce^{3+} almost doubles.



Figures 34-35. Showing the overall amount of copper cations relative to each other and the overall amount of Ce^{3+} relative to Cu^{1+}

From these site fraction studies we can see that the concentration of Cu^{1+} , Ce^{3+} , and vacancies increases with temperature. These studies also show that the evolution of Cu^{1+} and Ce^{3+} increases under a 1% oxygen environment when compared to an air

environment. In order to further confirm this, a plot of site fractions versus $\log P(\text{O}_2)$ was produced at the synthetically relevant temperature of 1350°C.

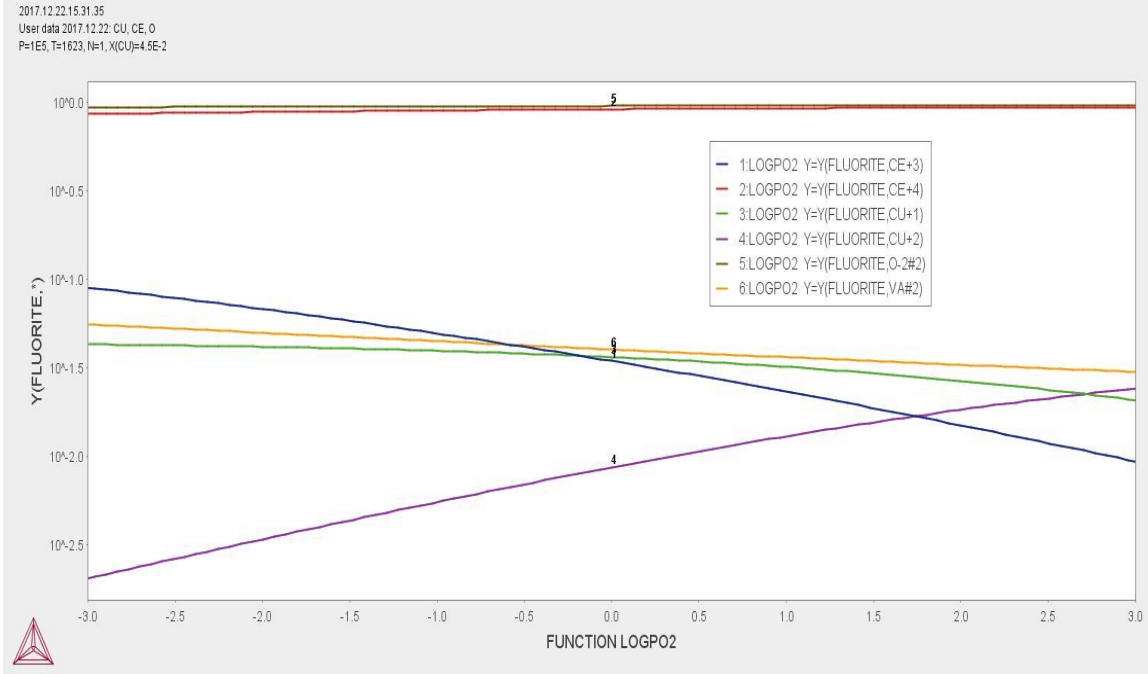


Figure 36. Site fraction occupancy vs change in oxygen partial pressure at 1350°C.

Fig. 36 shows that as oxygen partial pressure is decreased we see an increase in Cu^{1+} , Ce^{3+} , and vacancy concentrations and a decrease in Cu^{2+} , Ce^{4+} , and oxygen concentrations as we would expect. It also shows that Cu^{1+} remains dominant over Cu^{2+} at all partial pressures in agreement with the previously shown temperature dependent vacancy studies.

In conclusion we can show that as the temperature increases the copper doped fluorite phase increases in stability. We propose that this is linked to the change of oxidation state of the copper present within the phase from 2+ to 1+, leading to the formation of vacancies which stabilise the fluorite phase. This allows the maximum concentration of

Cu in the fluorite phase to reach 9 % under air conditions, with this decreasing to 7 % under reducing conditions.

Chapter 4 - Investigation of Oxygen Migration Mechanisms in $\text{Ge}_5\text{O}(\text{PO}_4)_6$

4.1. Aim

The aim of this project is to investigate oxygen migration in two phases of the material $\text{Ge}_5\text{O}(\text{PO}_4)_6$ including a structure similar to the material $\text{Si}_5\text{O}(\text{PO}_4)_6$. The nudged elastic band method will be used to find the activation energies of different oxygen migration pathways, in an attempt to find one which has an activation energy similar to the experimentally determined activation energy of oxygen migration.

4.2. Experimental activation energies and relationship between $\text{Ge}_5\text{O}(\text{PO}_4)_6$ and Si based alternative structure

This project is based upon previous work carried out by M. Tham⁷ of the Irvine Group. Tham's work identified the usefulness of $\text{Ge}_5\text{O}(\text{PO}_4)_6$ as a possible electrolyte material. The work examined both $\text{Ge}_5\text{O}(\text{PO}_4)_6$ (referred to later as structure I) (see figure 37), and a series of Germano-silicophosphates $\text{Ge}_{5-x}\text{Si}_x\text{O}(\text{PO}_4)_6$. Tham's work singles out the Germano-silicophosphate $\text{Ge}_3\text{P}_6\text{Si}_2\text{O}_{25}$ (referred to later as structure II) as being a structure of particular interest as it is an intermediate between the Ge and Si end members of the series⁷⁹. (See figure 38). In our work we look at an analogue of this structure where the Si has been replaced with Ge. This structure differs from that of the main $\text{Ge}_5\text{O}(\text{PO}_4)_6$ structure in two areas. The first is that the unit cell is 2/3 the length of the normal unit cell in the direction of the C-axis. The second area of difference lies in the distribution of the octahedra and bi-pyramids. Structure I can be split into three main columns which run along the length of the C-axis. Each of these columns contains a

mixture of octahedra and bipyramids which are connected together via phosphate (PO_4) groups. In the unit cell of structure II however there is no mixing of octahedra and bipyramids within the same column. Instead, two of the columns consist solely of octahedra, whilst the third consists of purely bi-pyramids. When a geometry optimization is performed on both of these unit cells using the PBE functional we can determine that the energy of the unit cell of structure I comes to -252.33 eV while the energy of structure II comes to -251.92 eV per unit cell. This would indicate that unit cell of structure II is 0.41 eV less stable than the unit cell of structure I at 0 K.

AC impedance experiments conducted by M. Tham⁷ indicate that the material has an activation energy of 0.3 eV for oxygen migration within the bulk structure, with the energy rising to 0.7 eV when a grain boundary is crossed.

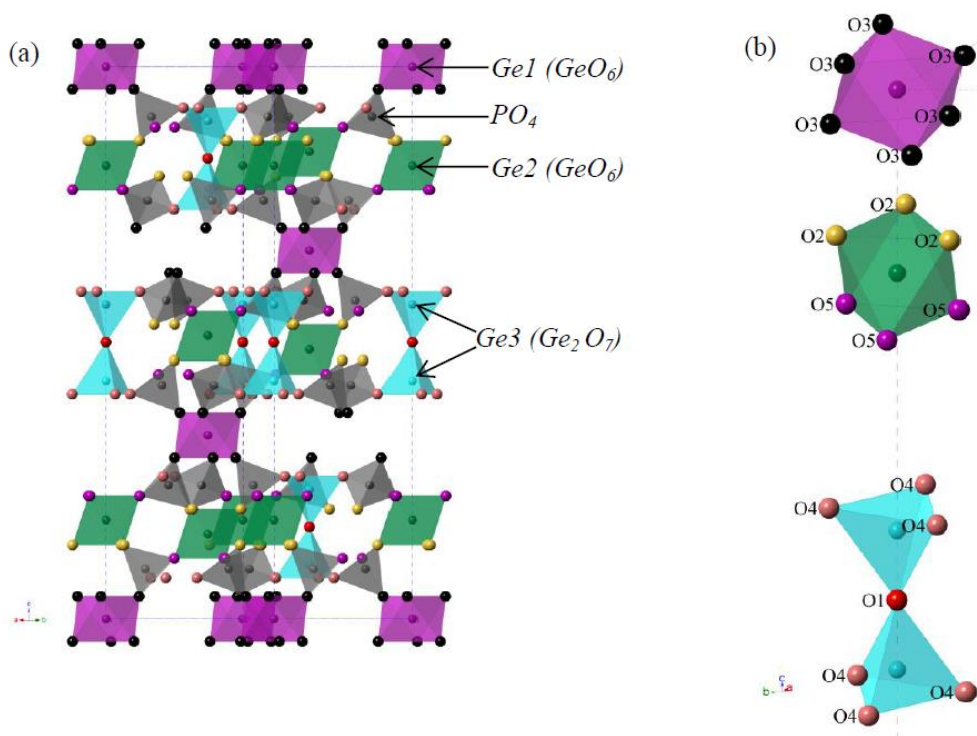


Figure 37. Projection of $\text{Ge}_5(\text{PO}_4)_6\text{O}$ (Structure I) along [100]. a) shows the whole structure where purple spheres are Ge1, green spheres are Ge2, light blue spheres are Ge3, and the grey spheres represent P. b) shows the oxygen environments. The red sphere is O1, yellow spheres are O2, black spheres are O3, pink spheres are O4 and purple spheres are O5. See chapter 1 for further details.

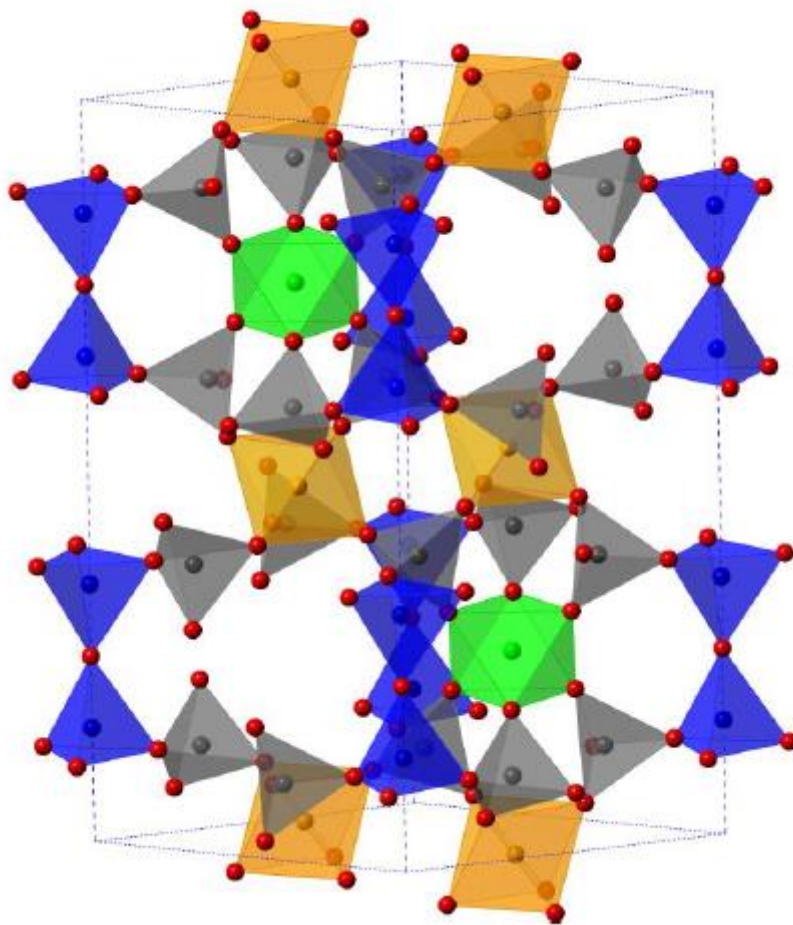


Figure 38. Projection of the alternative germanium structure based upon the structure of $\text{Ge}_3\text{P}_6\text{Si}_2\text{O}_{25}$ (structure II). Orange spheres are Ge(1), green spheres are Ge(2) and blue spheres are Ge(3). Red spheres represent oxygen while the grey spheres represent phosphorous. See chapter 1 for further details.

4.3. Method

In all cases shown below the migration path was identified using the climbing image nudged elastic band method. This CI-NEB is conducted in a version of VASP modified by the Henkelman group. All of the geometry optimizations are conducted using the PBE functional with a 3x3x1 K-Point grid and a 400 eV energy cutoff (The reduction in energy cutoff from 500 eV to 400 eV is based upon the results of the test calculation in section 4.4 which showed that a 400 eV cutoff is adequate for these calculations.) (any

exceptions to this will be noted in their individual sections). The lowest energy pathways in each section will then have further HSE single point calculations carried out on their respective energy minima and maxima using the same energy cutoff and K-Point grid. All calculations will use the Projector Augmented Wave method with associated Pseudopotentials.

The HSE single point calculations are carried out due to problems seen in the band structure when the PBE functional is used in the optimization of structures containing Germanium. This problem was highlighted by D. Colleoni and A. Pasquarello⁸⁰ who found that when only a PBE functional is used, the band gap of Germanium is underestimated, leading to metallic like characteristics. However, when the HSE functional is employed this band gap reappears.

4.4. Test Calculations

Before carrying out any calculations on our target material test calculations were first carried out in order to verify the validity of our method. We have chosen to attempt to repeat the results shown in the paper “Optimization of ionic conductivity in doped ceria” by A. Anderson et al.⁸¹. In their paper the activation energy of oxygen migration in ceria doped by different metals is calculated by solving the equation:

$$E_a = E_{\text{ass}} + E_m \quad (4.1)$$

Where E^m is the migration barrier and E_{ass} is the energy of association of the dopant which can prevent vacancies from being mobile. In this paper the migration barrier is computed by calculating the energy of the oxygen atom when it is sitting in a saddle

point position, which is estimated to be half way between the oxygen sites used in the diffusion process.

We have chosen to try and repeat the results regarding the activation energy of oxygen migration in Gd^{3+} doped ceria (see figure 39) using the NEB method. Anderson et al. reported that the activation energy for the migration of an oxygen to site 1 had an activation energy of roughly 0.7 eV. This was then compared against the experimentally reported activation energy which was 0.72 eV⁸².

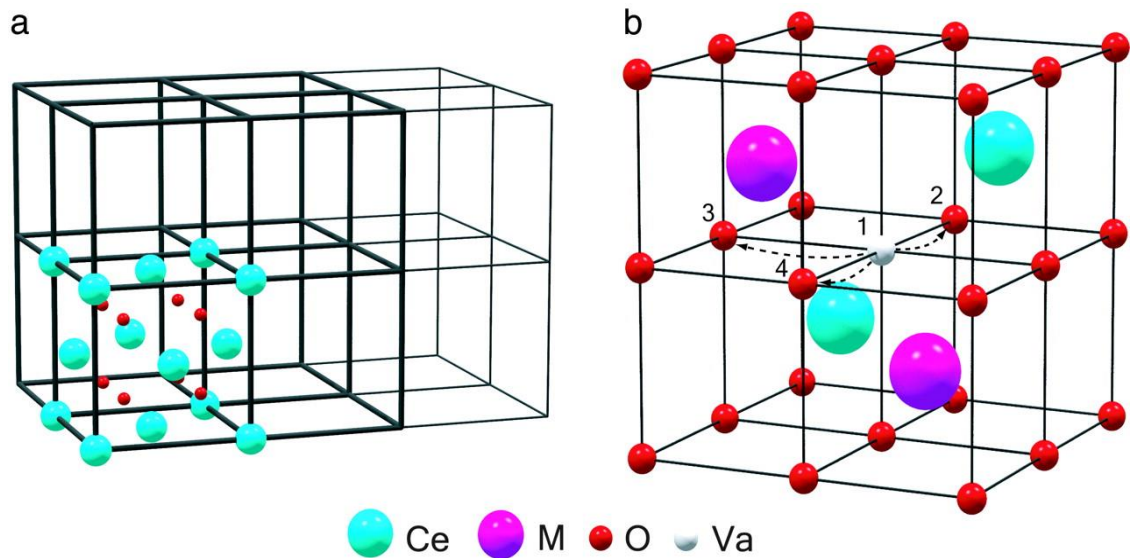


Figure 39. The fluorite structure of ceria and the supercells used to study its defect properties. (a) The $2 \times 2 \times 2$ (96 sites) supercell of ceria (thick lines) and the $3 \times 2 \times 2$ (144 sites) supercell (thick and thin lines). For clarity atoms are only shown in one of the ceria unit cells. (b) A unit cell of ceria centred at the cubic oxygen sublattice. The cell contains two 3+ dopants (M) sitting next to each other and an oxygen vacancy. The numbers designate different locations that the vacancy can occupy with respect to the dopants, and the arrows schematically show how the vacancy can jump from site 1 to nearby sites, which is equivalent to oxygen diffusion in the opposite direction. Site 1 corresponds to the NN (Nearest Neighbour) position. Figure and description taken from Anderson et al.⁸¹

Similarly to the calculations carried out by Anderson et al. a $3 \times 2 \times 2$ ceria super cell was set up in which two Ce atoms have been replaced by Gd to represent a 4.2% doping

level. We then carried out a 16 point CI-NEB calculation using the PBE functional with an energy cut-off of 400 eV and a 1x1x1 kpoint grid. This calculation resulted in an activation energy of 0.56 eV (represented by E_a in equation 4.1) which is approximately 0.14 eV lower than the results reported by Anderson et al. As these results showed an acceptable accuracy with respect to the experimentally determined activation energy we chose to not repeat the calculations using a larger kpoint grid. It would be expected that if a larger grid were used that the energy barrier would increase in energy resulting in an increased agreement with the experimentally determined activation energy.

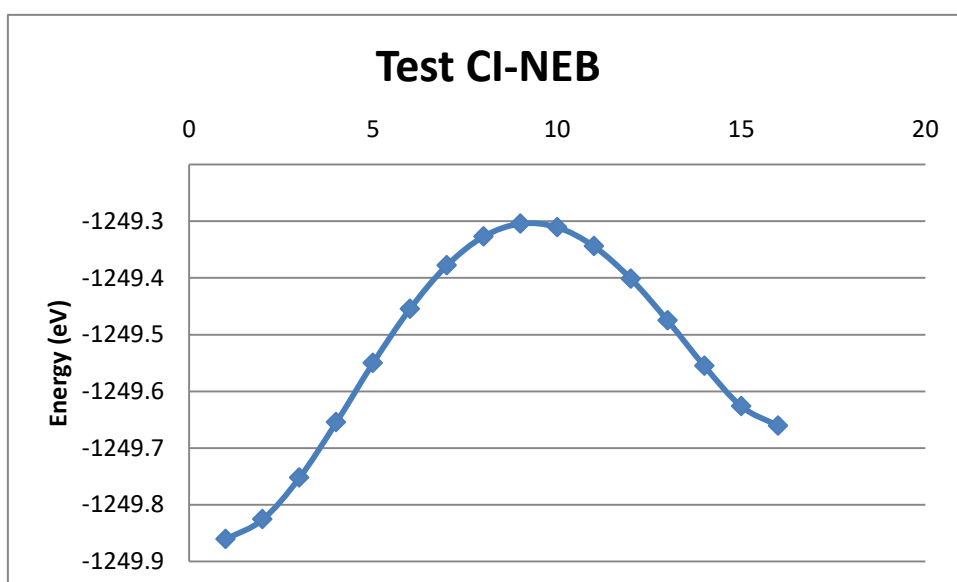


Figure 40. The energy pathway as calculated using the PBE functional

An HSE single point correction was then applied to this NEB which further reduced the activation energy to 0.40 eV.

From these results it can be seen that the CI-NEB method can give results that are within an acceptable margin of error in comparison to previously reported activation energies for oxygen migration.

4.5. Investigation of possible mechanisms within $\text{Ge}_5\text{O}(\text{PO}_4)_6$

This project is split into the investigation of two materials. The first material that will be investigated is the $\text{Ge}_5\text{O}(\text{PO}_4)_6$ structure (structure I). We will look at the possible pathways and compare them to the experimentally determined activation energy.

2.5.1. Rotation of Tetrahedron

As a starting point of this investigation it was decided to use the interstitialcy mechanism along the C-axis proposed by M. Tham⁷ (See figure 41)

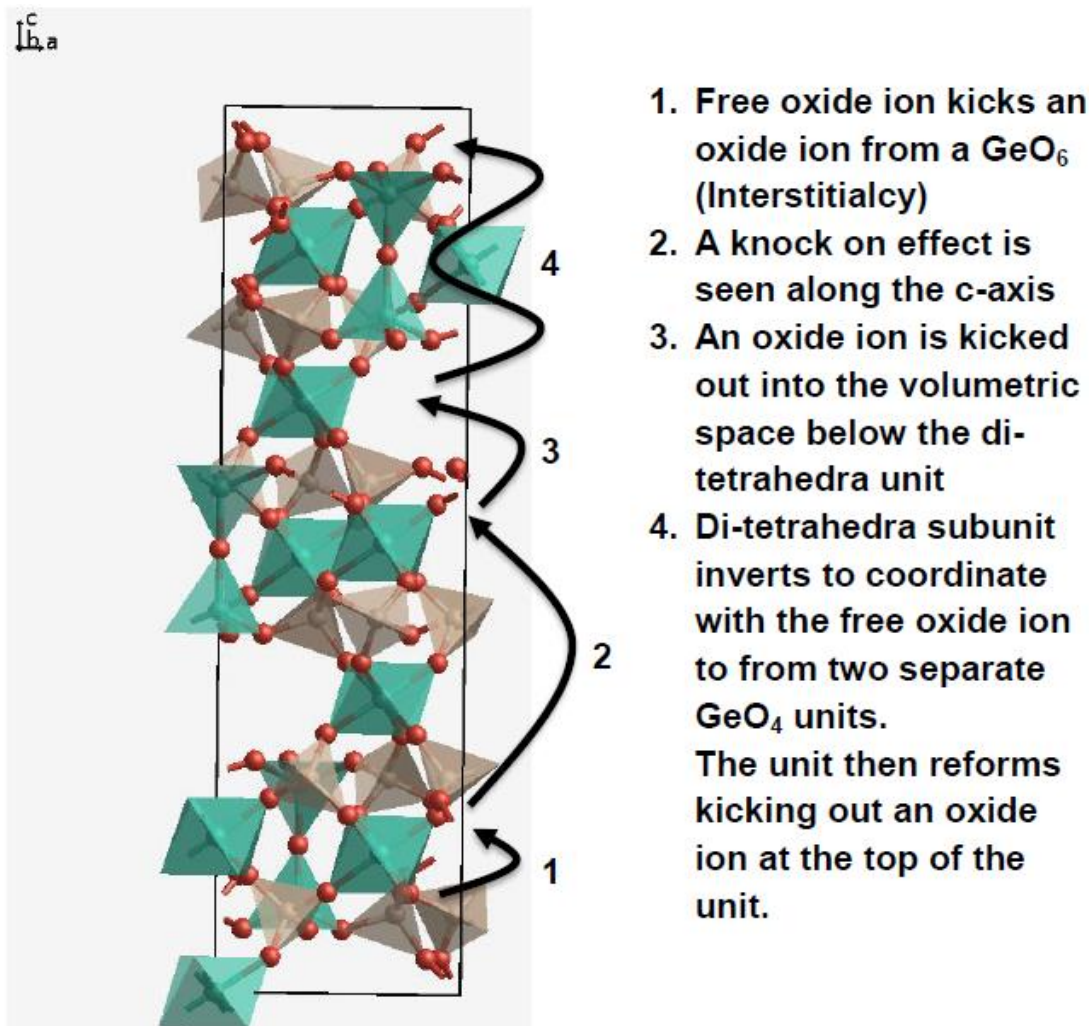


Figure 41. The interstitialcy mechanism proposed by M. Tham⁷.

In this mechanism the first step involves the O1 oxygen atom in the bi-pyramidal structure kicking out one of the oxygens situated in the O4 positions above it. The oxygen in the O4 position then moves into the interstitial space above the bi-pyramid (see figure 42). This movement results in an upward rotation of the top tetrahedron in the bi-pyramid.

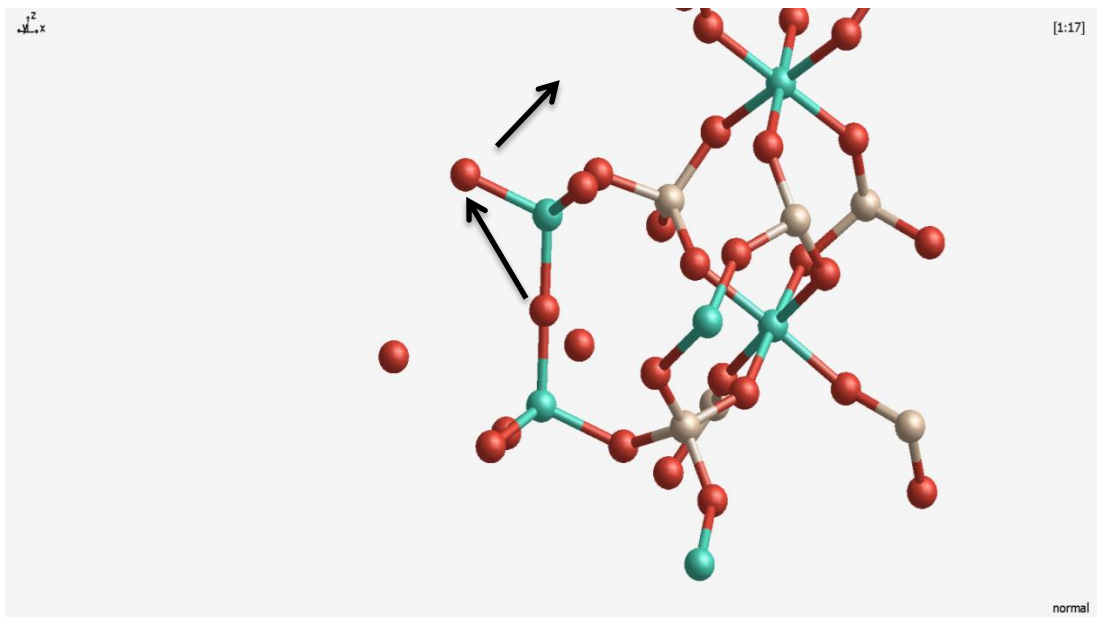


Figure 42. The rotational movement around the germanium atom.

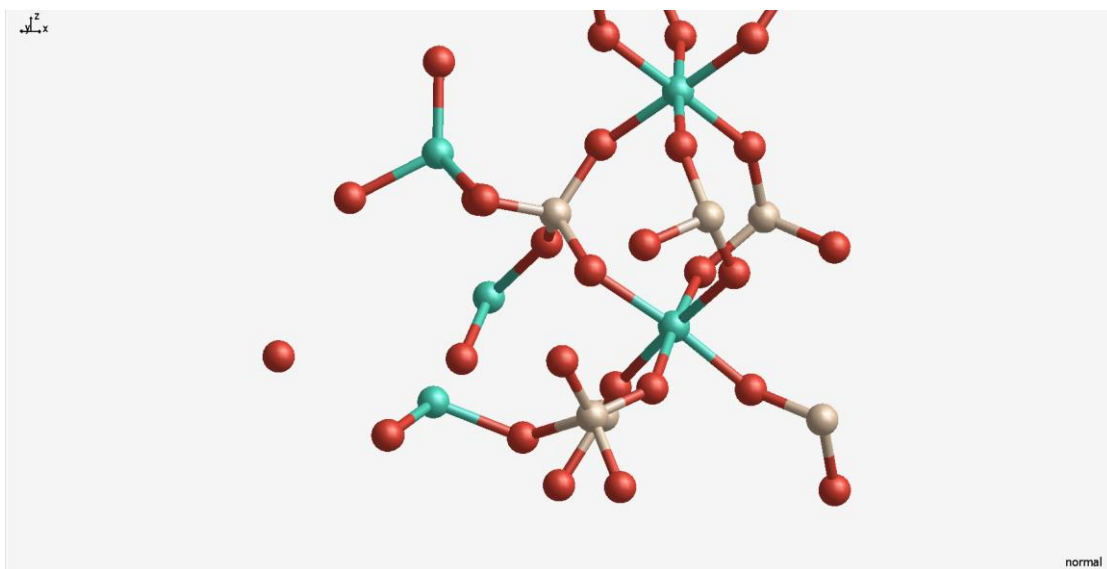


Figure 43. Configuration of atoms after movement

To simulate this movement a 16 point CI-NEB was created. The maximum energy of this NEB was shown to occur at point 9, which leads to an activation energy of 4.80 eV, with the activation energy of the reverse process being 0.67 eV. As stated in the methods section, a further HSE single point calculation was carried out on point 9 as well as on points 1 and 2, which are next to the optimized starting and end structures at 0 and 17 (not shown). These single point calculations led to an increase in the activation energies from 4.80 eV for the forward reaction and 0.67 eV for the reverse reaction to 5.62 eV for the forward reaction and 1.57 eV for the reverse reaction respectively.

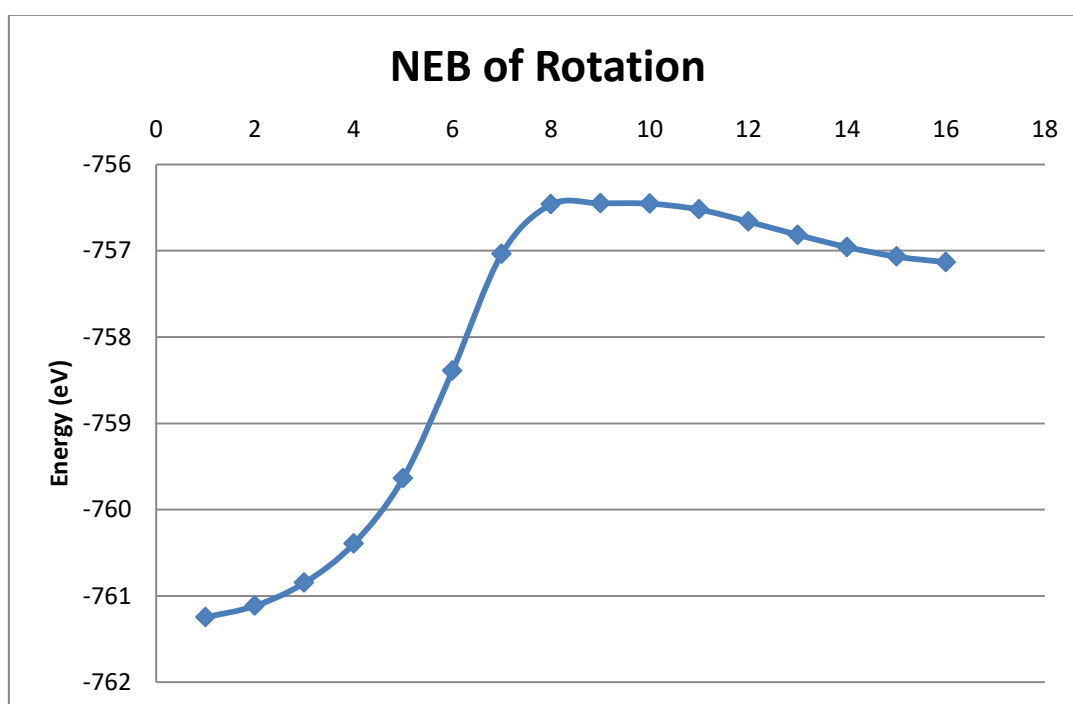


Figure 44. The CI-NEB of the twisting motion as calculated using the PBE Functional.

These results show that this step of the movement suggested by Tham⁷ would lead to activation energy more than an order of magnitude higher than seen experimentally. Due to this result we would suggest that the proposed mechanism would not be able to produce the experimentally determined activation energy.

2.5.2. Vacancy Mechanisms

After ruling out a mechanism involving the twisting motion described above it was then decided to attempt to look at possible vacancy mechanisms for the movement of oxygen. To do this we studied the movement of one oxygen atom at a time. This then allowed us to stitch together a complete pathway from all of the one atom “hops”. All of the hops are calculated using 16-point CI-NEBs as standard.

2.5.2.1. Movement O1 to O4

The first vacancy movement investigated was the movement of an oxygen atom from an O1 site to a vacancy in an O4 site (See Figure 45). This movement would result in an oxygen atom moving from the oxygen site in the middle of a bi-pyramid to an oxygen site at the top of the same bi-pyramid.

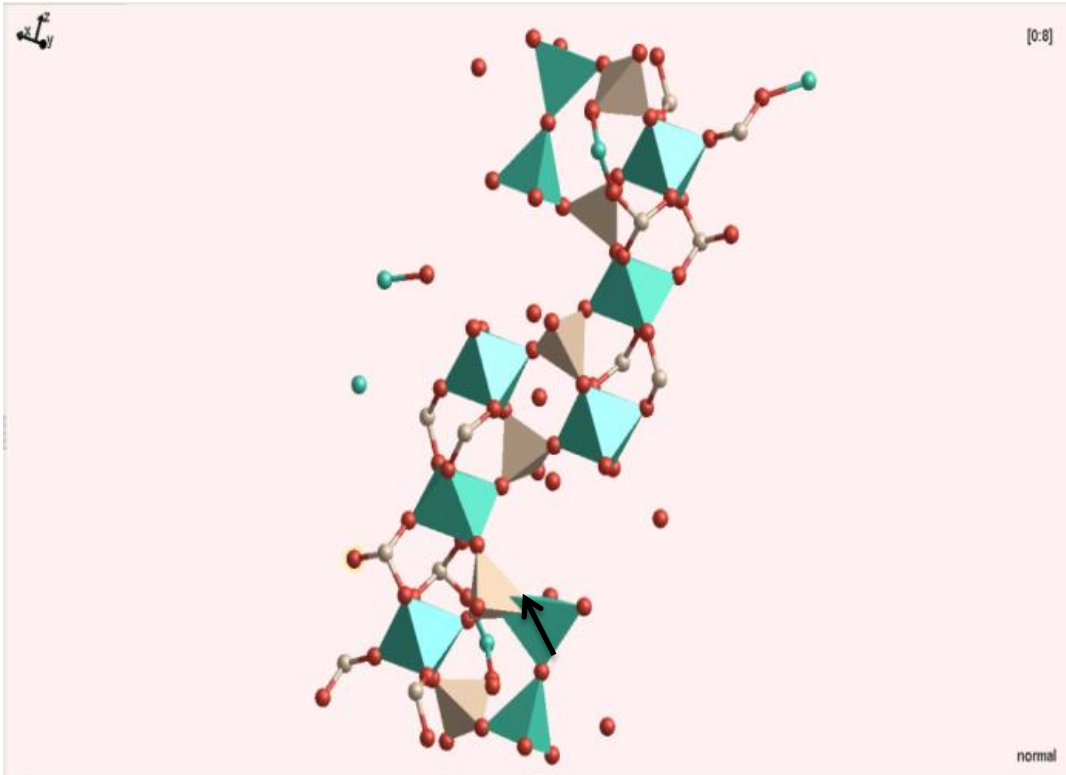


Figure 45. Movement of an oxygen atom in the O1 position to a vacancy in an O4 site above.

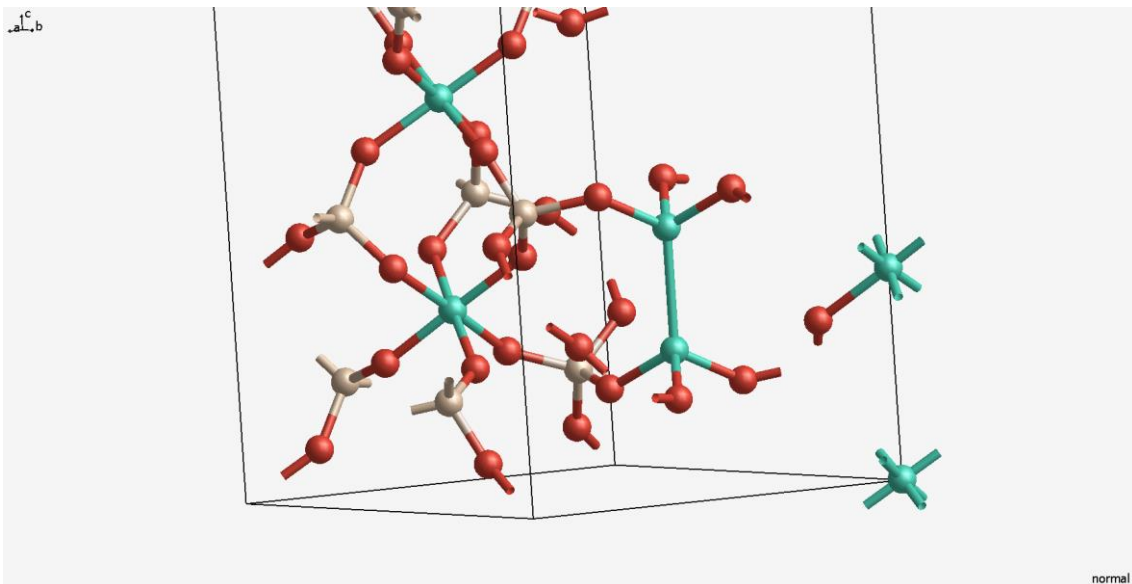


Figure 46. Configurations of atoms after movement

The CI-NEB for this movement shows an energy maximum at point 8. This energy maximum leads to an activation energy of 2.77 eV for the movement when calculated using PBE. While still much higher than the experimental value, this movement plays a part in the lowest energy pathway, using a vacancy mechanism and as such further HSE single point calculations were carried out. After the HSE single point calculations were carried out this activation energy rises from 2.77 eV to 3.80 eV. Using the CI-NEB we can also identify the activation energy for the reverse reaction. In this case the energy for this reverse reaction is originally 3.82 eV which increases to 4.90 eV after the further HSE calculations.

Figure 46 shows the presence of a Ge-Ge bond. This bond is a temporary bond until an oxygen atom moves from one of the sites below into the O1 site in the next step.

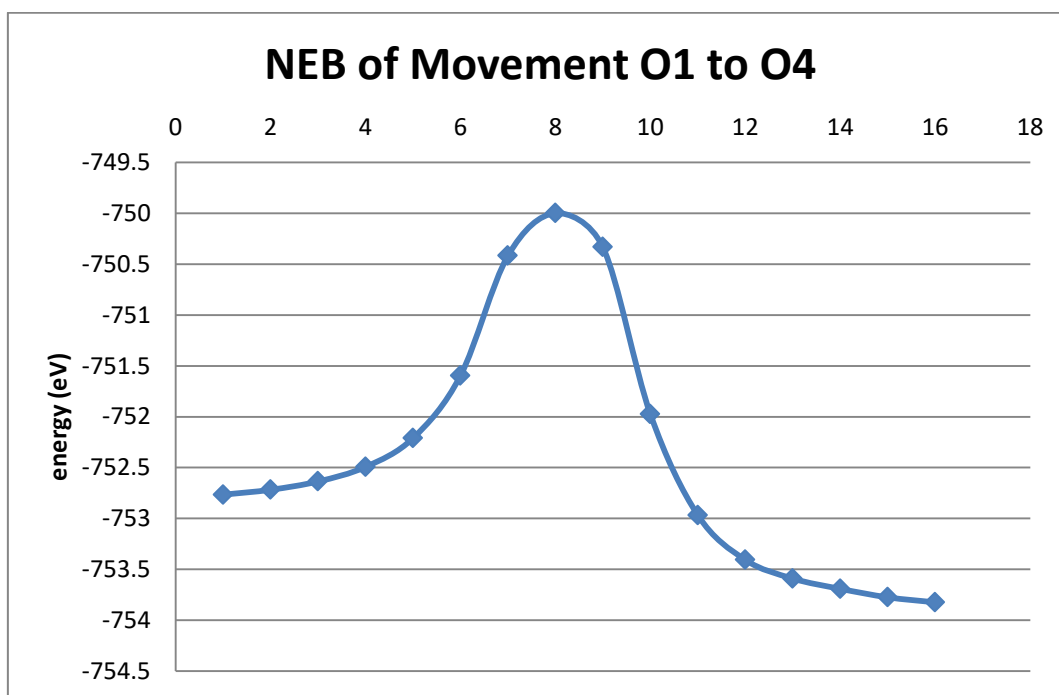


Figure 47. CI-NEB of the movement as calculated using the PBE functional.

2.5.2.2. Movement O4 to O3

From the end of the movement of an oxygen atom from the O1 site to the O4 site the oxygen can then move in two different directions, either up the cell along the c-axis or along the cell using the a/b –axis. The first movement investigated was the movement of the oxygen along the a-b axis as this was the shortest route. The next movement along this route is the movement of an oxygen atom from the O4 site at the top of a bi-pyramid to a vacancy in an O3 site in an adjacent octahedron (see figure 48). In our calculation of this movement the vacancy in site 1 has been filled by another oxygen. In our calculations of each step we are actually following the mechanism of conductance in reverse. As a result this would be the penultimate step in a conductance mechanism where the vacancy started in the O1 position in an adjacent unit cell. This movement would correspond to the step indicated by the purple arrow in Figure 56 with the reverse movement correlating with the light blue arrow.

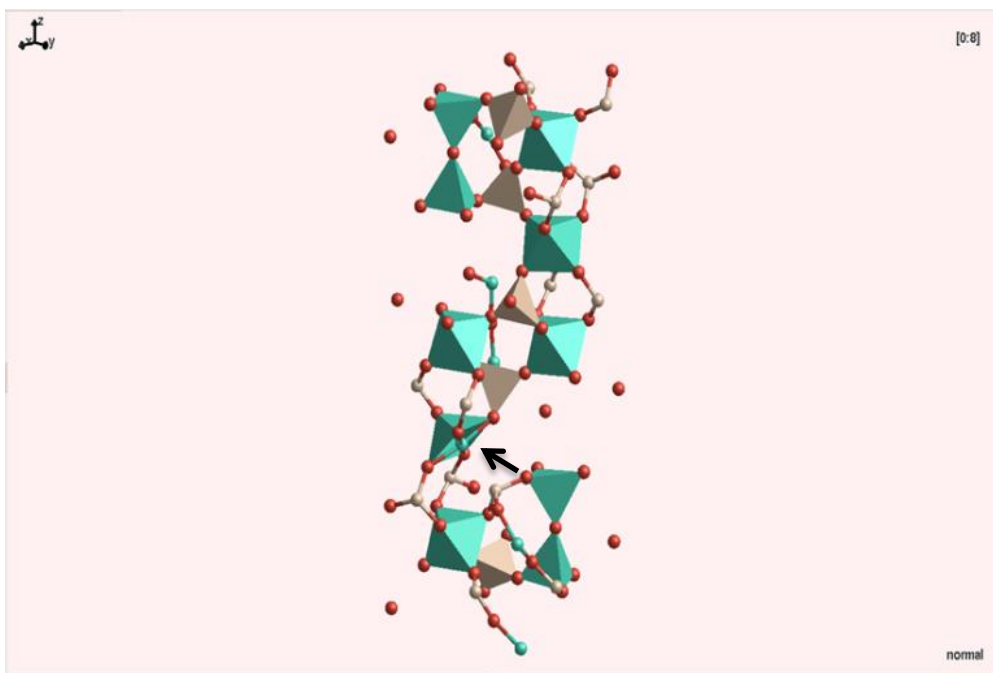


Figure 48. Movement of an oxygen atom from the O4 position to the O3 position.

The initial PBE CI-NEB results gave the following pathway structure:

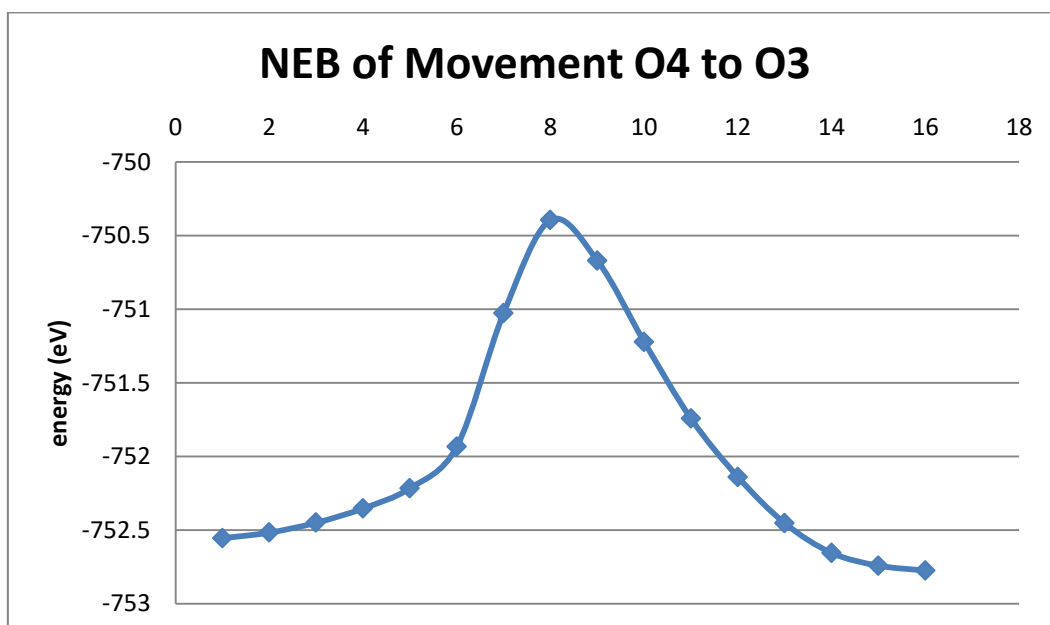


Figure 49. CI- NEB of this movement as calculated using the PBE functional.

In this 16 image pathway the maximum energy is found at point 8. From this pathway we show that when going from point 1 to point 16 the activation energy is 2.16 eV with the activation energy of the reverse reaction being 2.38 eV. Similarly to the movement of an oxygen from O1 to O4 this movement also forms part of the lowest energy pathway. The HSE single point calculations carried out on this pathway results in the activation energies being raised to 2.77 eV and 3.20 eV respectively.

2.5.2.3. Movement O3 to O3

In order to complete the movement of an oxygen along the a/b – axis a third movement type is needed. This third movement investigated is the movement of an oxygen atom from one O3 site within an octahedron to another adjacent O3 site within the same octahedron (see figure 50).

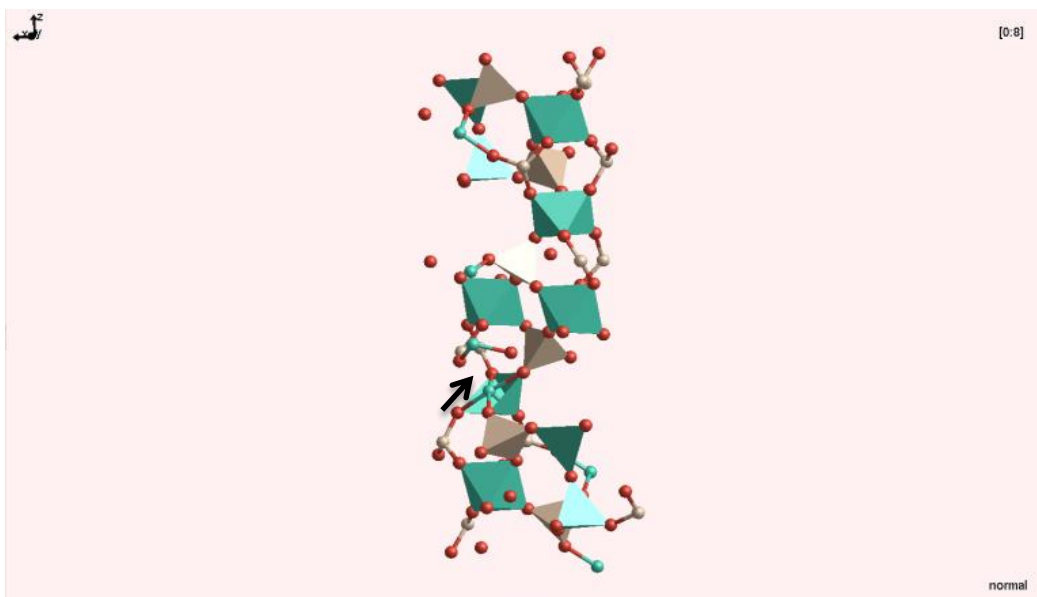


Figure 50. The movement of an oxygen atom from one O3 site to another O3 site within the same octahedron.

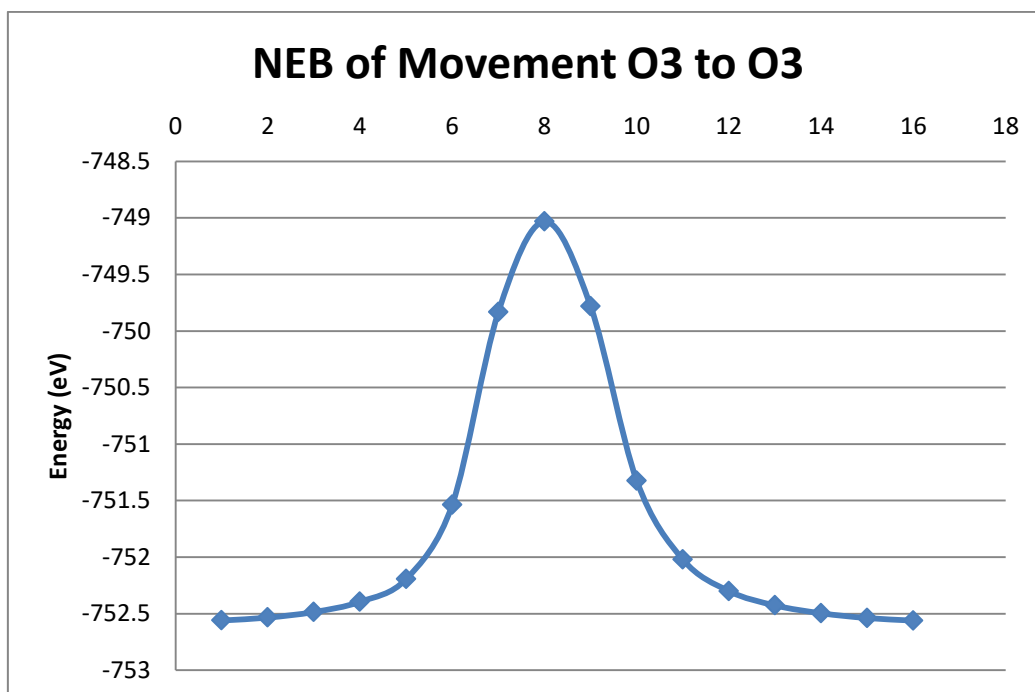


Figure 51. CI-NEB as calculated using the PBE functional.

Similarly to the first two movements in this pathway the energy maximum was found to occur at point 8 in the CI-NEB. This movement was found to have an activation energy of 3.53 eV. As this is the movement of an oxygen atom from one O3 site to another we would expect the energy of the reverse reaction to be the same as the activation energy seen for the forward reaction. It was found that the reverse energy does indeed follow this trend with its activation energy also being 3.53 eV. As this CI-NEB is part of the lowest energy pathway along with the previous two movements further HSE single point calculations were again carried out which increased the activation energy from 3.53 eV to 4.31 eV.

2.5.2.4. Movement O4 to O5

After studying all movements allowing a full diffusion along the A/B axis, the movement of oxygen along the C-Axis was examined. With the movement of an oxygen atom from an O1 site to an O4 site already examined, it was decided to next investigate the movement of an oxygen atom from the O4 site within a bi-pyramid to the O5 site of an octahedron above it through the interstitial space (see figure 52).

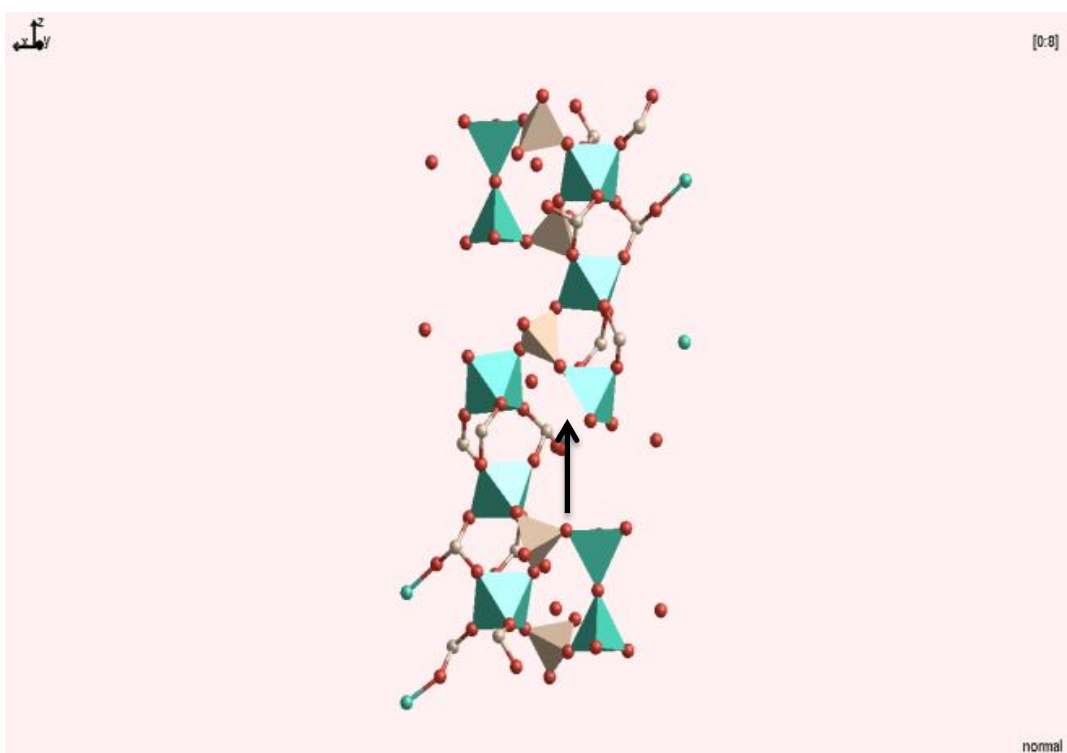


Figure 52. The movement of an oxygen atom from an O4 site to a vacant O5 site through the interstitial space.

The energy pathway seen in the CI-NEB of this movement differs from those seen previously. Unlike the previous NEBs this energy pathway has two different energy maxima at points 7 and 12. The energy of the maximum at point 7 is higher in energy than the maximum at point 12 by roughly 0.7 eV. As such the activation energies for

this reaction are controlled by the maximum at point 7. The forward reaction is shown to have an activation energy 6.45 eV with the reverse reaction having an activation energy of 6.61 eV.

It can be seen that when calculated using the PBE functional the activation energy of this movement is higher than the maximum activation energy of the pathway along the a/b-axis by 2.79 eV. Due to this energy difference, it is clear that this movement is not part of the lowest energy mechanism, and as such no HSE single point calculations were carried out, as it was felt that the computational cost of such calculations were too high for them to be carried out on movements that are not part of the lowest energy pathway.

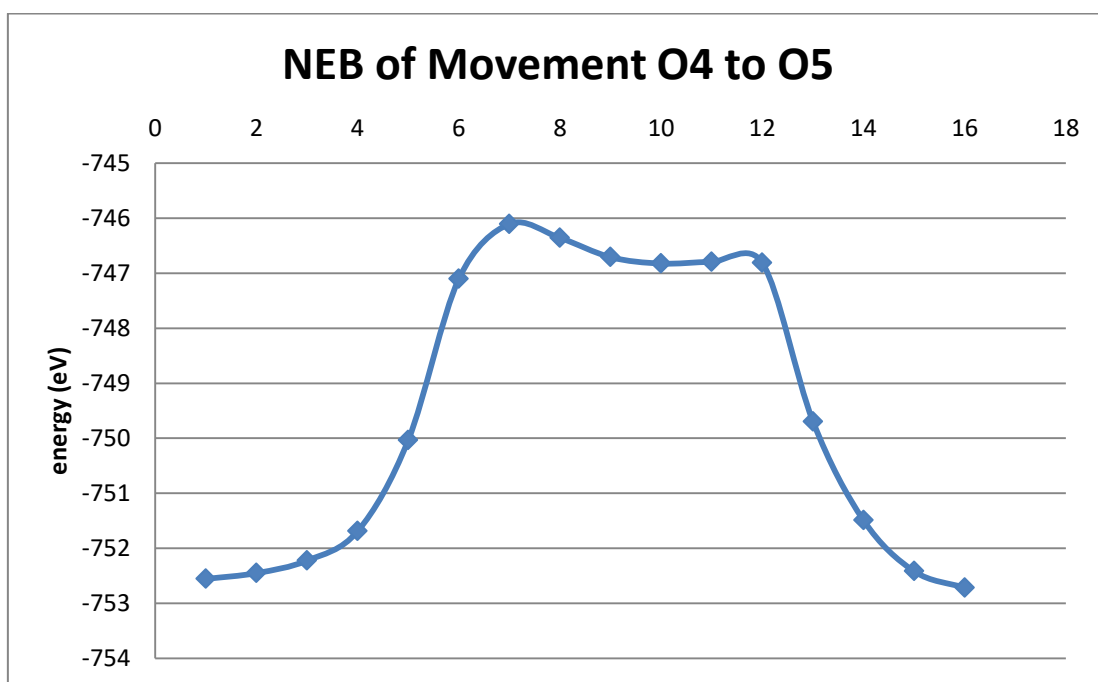


Figure 53. CI-NEB of the movement as calculated using the PBE functional.

2.5.2.5. Movement O2 to O3

Even with the movement of an oxygen atom up through the interstitial space above the bi-pyramid ruled out, there is still the possibility of the oxygen atom moving along the c-axis, via the interstitial movement of an oxygen atom from one octahedron to the next. In this movement an oxygen atom moves from an O2 site through a PO_4 group to an O3 site on the adjacent octahedron (See figure 54).

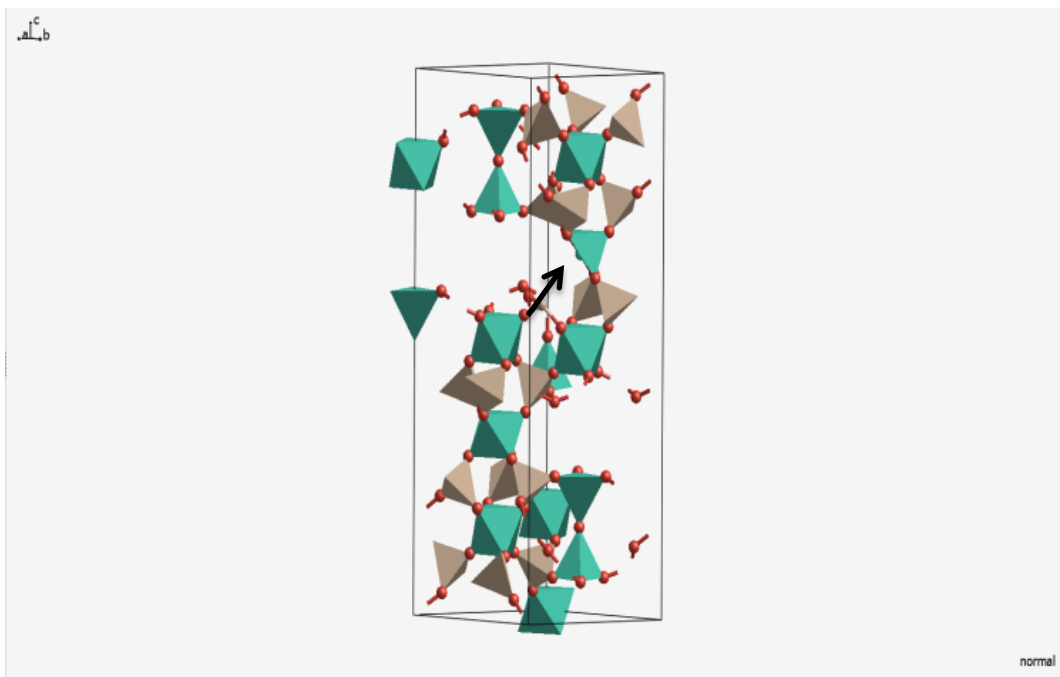


Figure 54. The movement of an atom from an O2 site to an O3 site present on an adjacent octahedron

The initial CI-NEB results gave the following pathway structure:

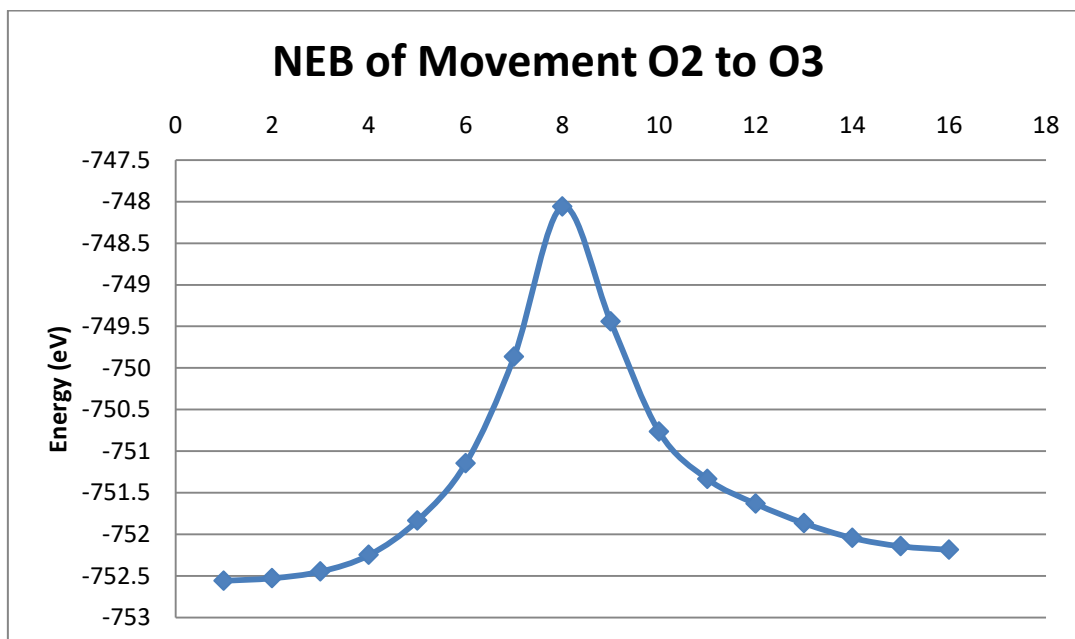


Figure 55. The CI-NEB as calculated using the PBE functional.

This NEB has an energy pathway that is similar to the NEBs for the movements across the a/b- axis with a single maximum located at point 8. The activation energy for this movement was calculated to be 4.50 eV with the reverse activation energy being 4.12 eV. While these activation energies are lower than the ones for the movement between an O4 and an O5 site they are still higher than any of the activation energies for the movements along the a/b-axis. As this movement is not part of the lowest energy pathway we have again opted not to carry any HSE single point calculations.

2.5.2.6. Lowest Energy Full Movement

By comparing all of the different movement types it can be determined that the lowest energy pathway through the cell will use movements O1-O4, O4-O3 and O3-O3. By merging these movements together we can produce a movement through the A/B axis of the unit cell (See figure 56).

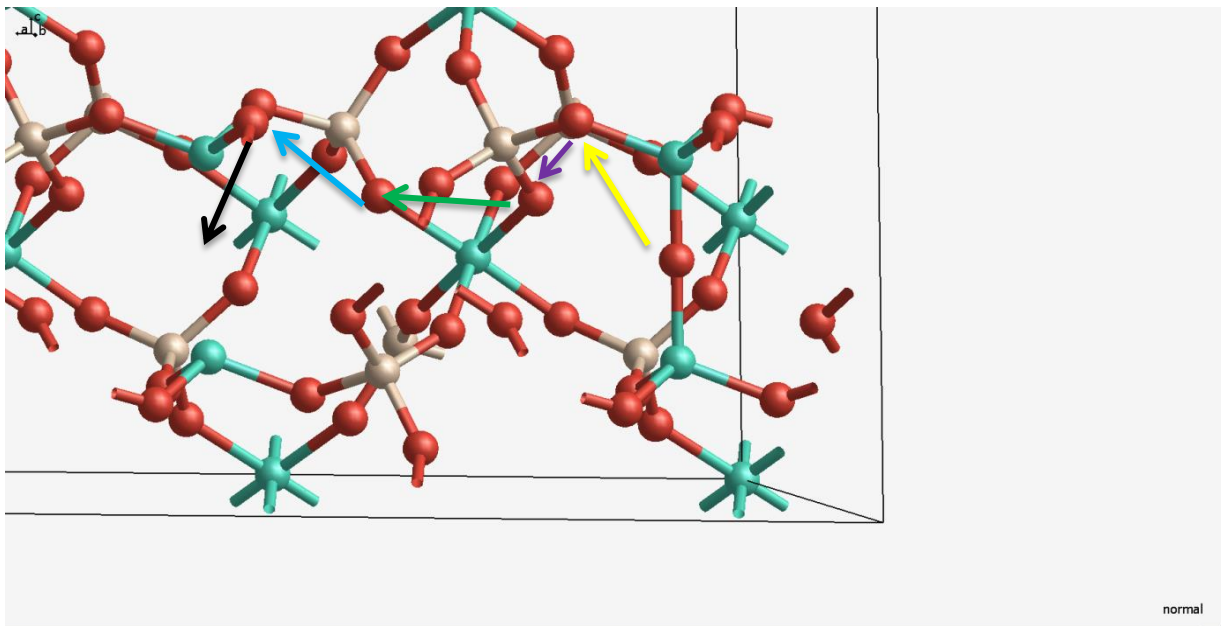


Figure 56. The full mechanism for movement along the a/b axis using a vacancy mechanism.

By combining the appropriate NEBs the following energy profile for the vacancy mechanism can be produced:

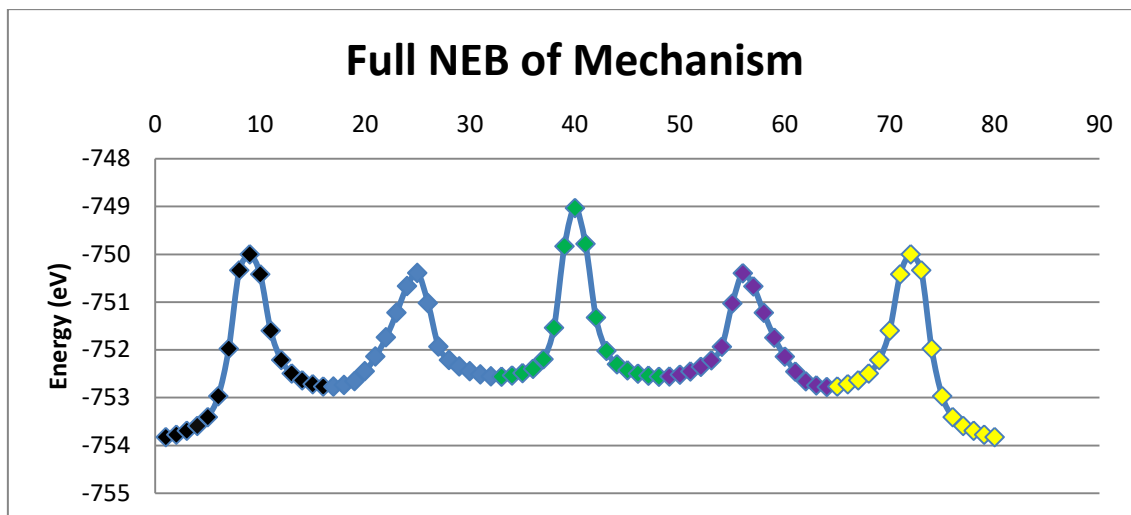


Figure 57. The CI-NEB as calculated using the PBE functional. The colours represent the regions of the NEB related to the different movements shown in figure 56.

This profile shows the results from the PBE based NEB calculations and has a total activation energy of 4.80 eV. When we take the results from the HSE single point calculations this is increased to 5.84 eV.

This activation energy is again higher than the experimentally determined activation energy of 0.3 eV as determined by Tham⁷ by a factor of 19. As a result it is clear that a vacancy only mechanism is not responsible for the activation energy seen during oxygen migration.

2.5.3. Interstitialcy Mechanism

Based upon the results of the vacancy study it can be concluded that the lowest energy pathway traverses the a/b planes of the unit cell. Using this information as well as experimental data showing oxygen sites around the O1 position, we decided to test for the possibility an interstitialcy mechanism where an additional oxygen atom is located in an interstitial site beside the O1 atom and moves through a knock-on mechanism, starting by replacing the oxygen along the a/b axis to start a mechanism similar to the minimum energy pathway seen in the vacancy study. This mechanism can be seen in figure 58.

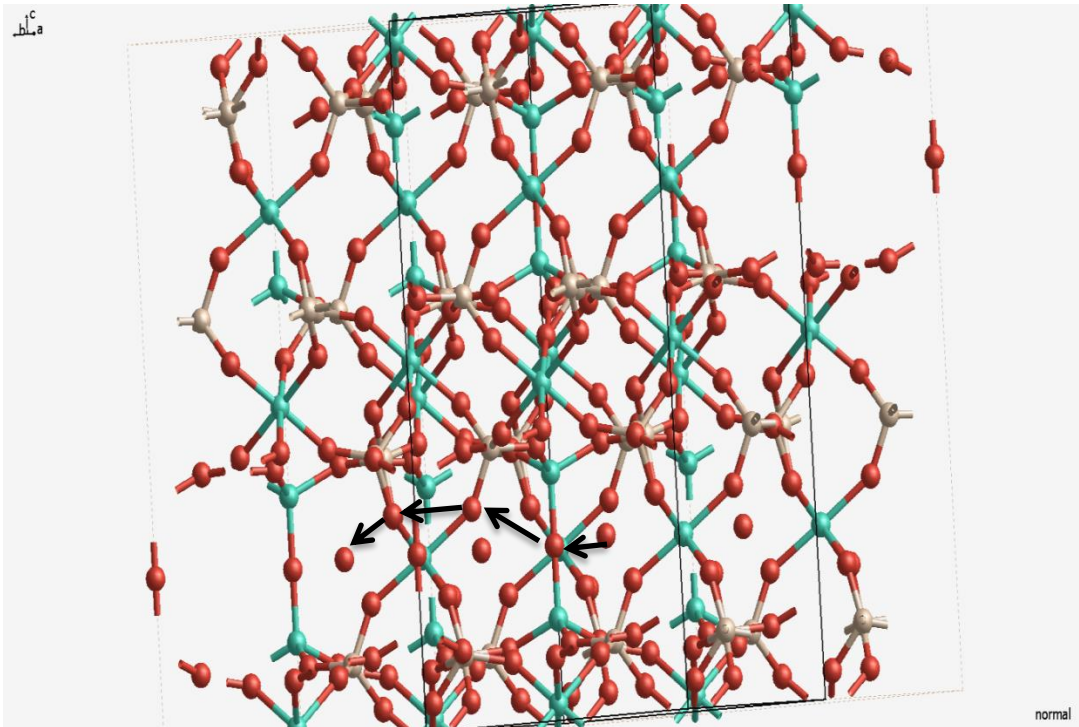


Figure 58. Pathway of the full mechanism for movement along the a/b axis using an interstitialcy mechanism.

In the NEB of the full vacancy mechanism 80 points were used, spread amongst five different calculations that made up the full movements. As we are carrying out this

interstitial NEB in one full calculation the decision was made to decrease the number of points in the NEB to 32 due to computational constraints.

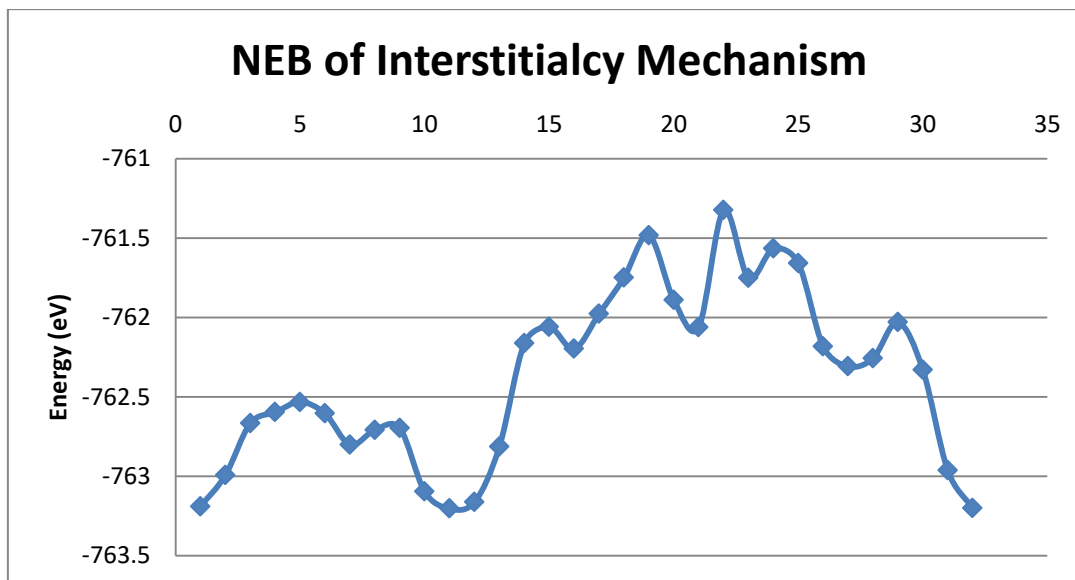


Figure 59. The CI-NEB as calculated using the PBE functional.

In this 32 image pathway the maximum energy is found at point 22 and it can be seen that the minimum energy for the forward reaction occurs at point 11 which is roughly 0.01 eV lower in energy than the starting structure. From this pathway it can be shown that the activation energy for this mechanism is 1.88 eV with the reverse energy also being 1.88 eV. As this is the lowest energy pathway in this category we again carried out HSE single point calculations which caused the activation energy to increase from 1.88 eV to 2.03 eV.

This mechanism is the lowest energy mechanism found for the regular $\text{Ge}_5\text{O}(\text{PO}_4)_6$ structure and is roughly 1.7 eV higher than the activation as found experimentally.

As no pathway through the normal structure can be found in which the activation equalled the one found via experiment, we started to investigate the alternative structure

found within the material in order to determine if its presence could be a factor in the migration mechanism.

4.6. Investigation of Mechanism within Structure II

2.6.1. Rotation of Tetrahedron

Similarly to the structure I, we first looked at the rotation of the tetrahedron at the top of the bi-pyramid (see figure 60).

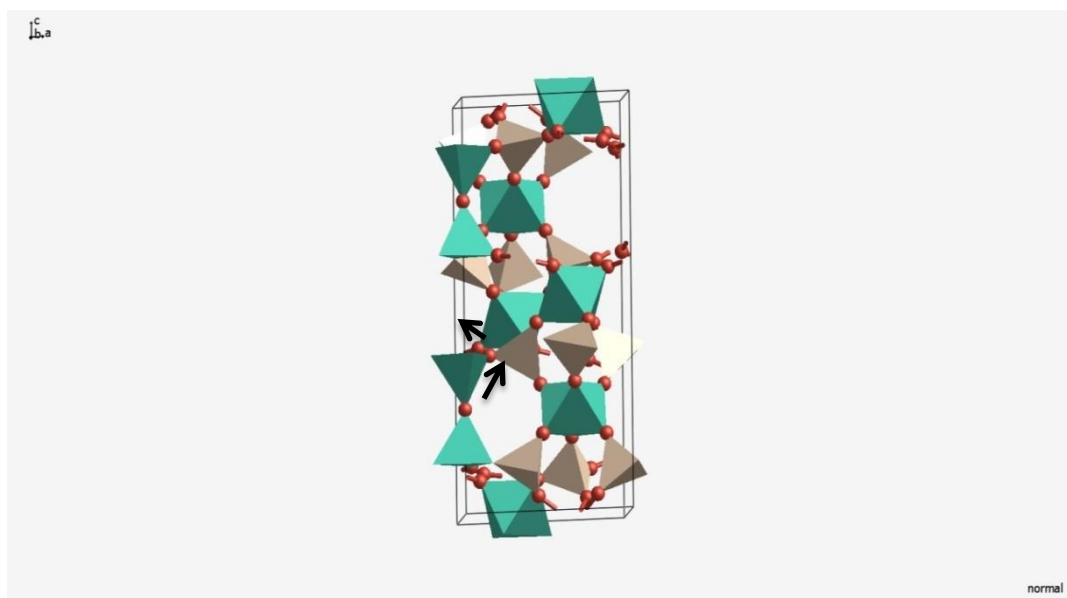


Figure 60. Movement of the oxygen atoms during the rotation.

The maximum for this pathway occurs at point 10, while the maximum in the original structure occurred at point 8. The activation energy for this pathway is 5.28 eV with a reverse activation energy of 2.31 eV. When HSE single point calculations are carried out on this pathway the activation energies increase from 5.28 eV and 2.31 eV to 6.76 eV and 3.19 eV respectively.

It was found that these activation energies are even higher than those of the same mechanism within structure I, being 1.14 eV and 1.62 eV higher respectively. The

increase in energy of this movement could be linked to changes in the atomic positions of the other atoms in the cell. The changes in the position of these atoms causes the lattice structure within the rest of the cell to become distorted in relation to the normal lattice structure. This results in a higher energy relative to the starting structure.

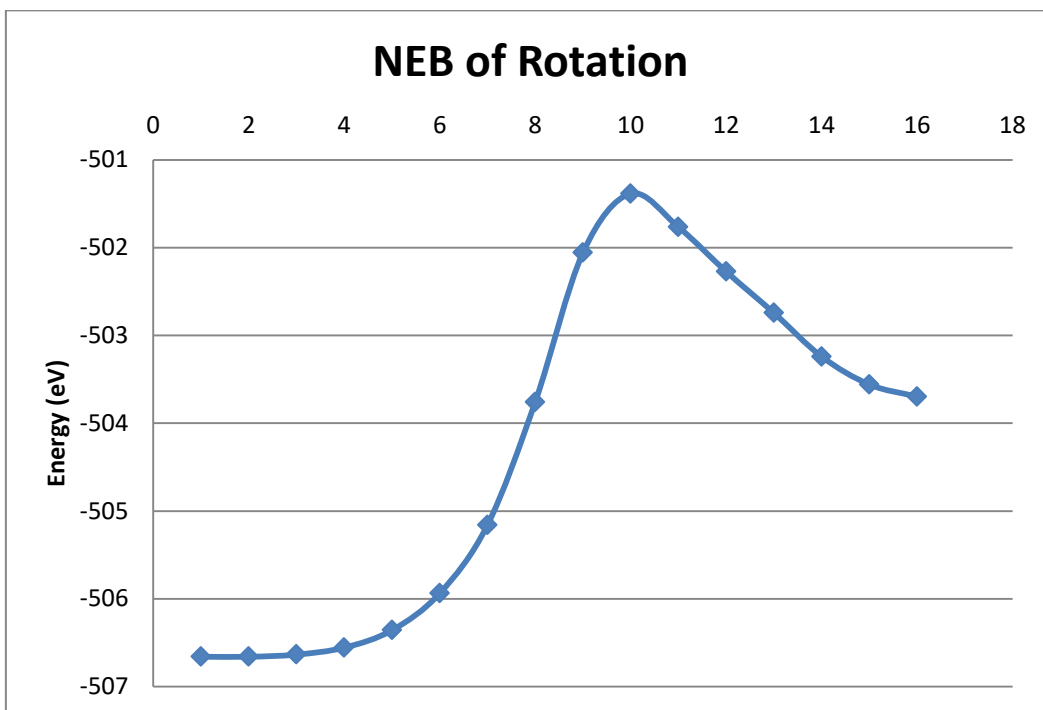


Figure 61. The CI-NEB as calculated using the PBE functional.

2.6.2. Vacancy Mechanism

After investigating the twisting motion we then investigated possible vacancy mechanisms for the movement of oxygen in the same way as we did in the normal structure. As stated before, due to the similarities in the structure between structure I and structure II, these single atom movements will be the same as the movements investigated during our investigation of structure I. As these movements are the same

as in structure I all of the CI-NEBs' carried out will contain the same number of images as those carried out for structure I.

2.6.2.1. Movement O1 to O4

The first vacancy movement investigated was the transfer of an oxygen atom from an O1 site to a vacancy in in an O4 site (figure 62). This describes an oxygen atom moving from the oxygen site in the middle of a bi-pyramid to an oxygen site at the top.

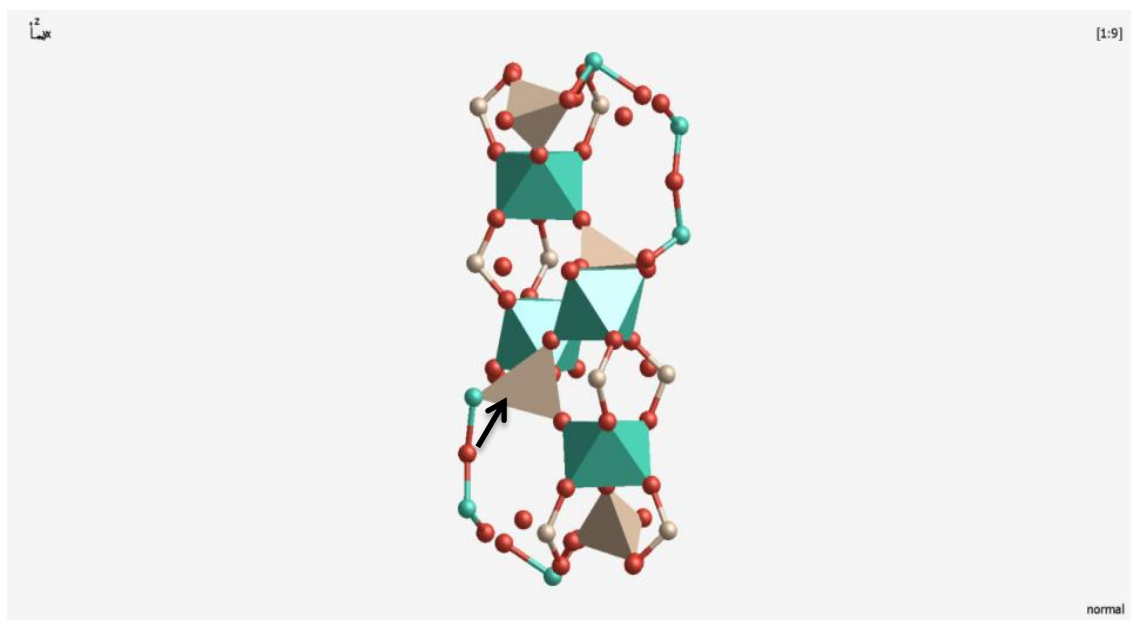


Figure 62. The movement of an atom in the O1 position to a vacancy in the O4 position

:

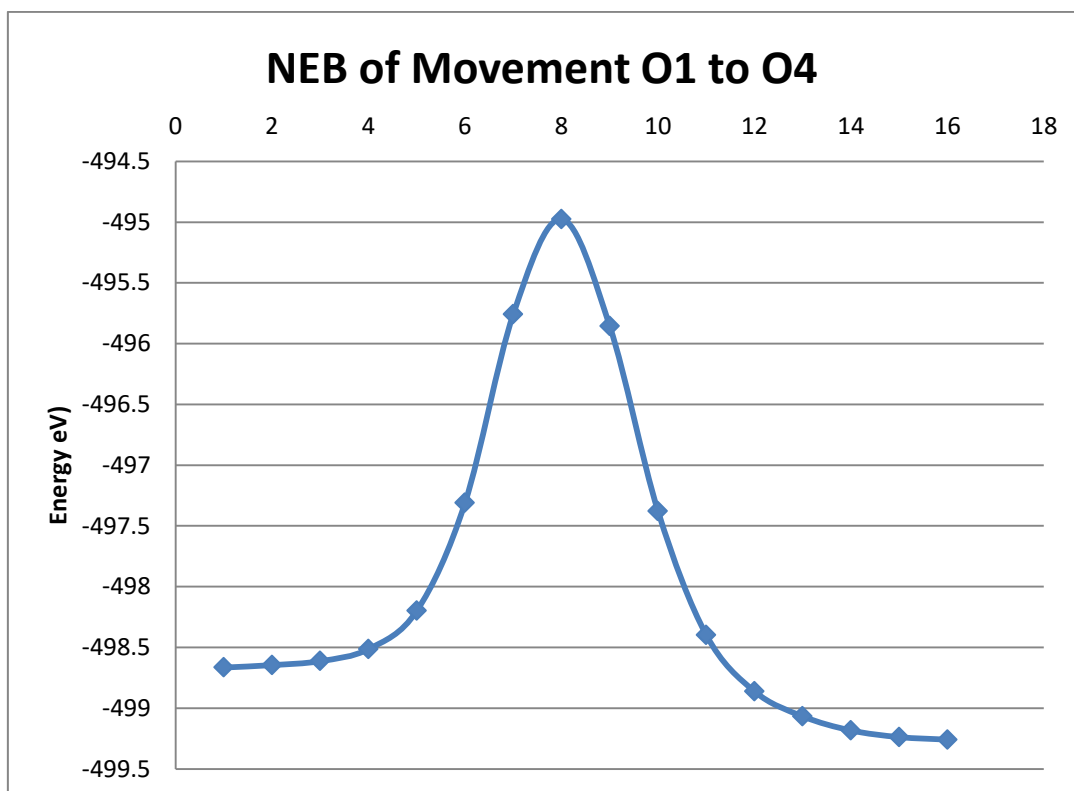


Figure 63. The CI-NEB of the movement of the O1 atom to vacant O4 position as calculated using the PBE functional.

It can be shown that the maximum for the pathway occurs at point 8 the same as in the pathway for the normal structure. This pathway was found to have a higher activation energy than its counterpart in the normal structure with an activation energy of 3.69 eV instead of the 2.77 eV activation energy found in the normal structure. After the calculation of HSE single points the activation energy rises to 4.64 eV which is again higher than the 3.80 eV found in the regular structure. When looking at the reverse activation energy we find that it is originally 4.28 eV which rises to 5.21 eV after the single point calculations. This is again a larger activation energy than its counterpart in structure I.

2.6.2.2. Movement O4 to O3

In a similar way to our calculations regarding the structure I we first investigated movements that would allow for a mechanism through the a/b axis of the unit cell. This led to the next movement being investigated to be the movement of an atom from an O4 position in a bi-pyramid to a vacancy in an Octahedron (O3) (See figure 64).

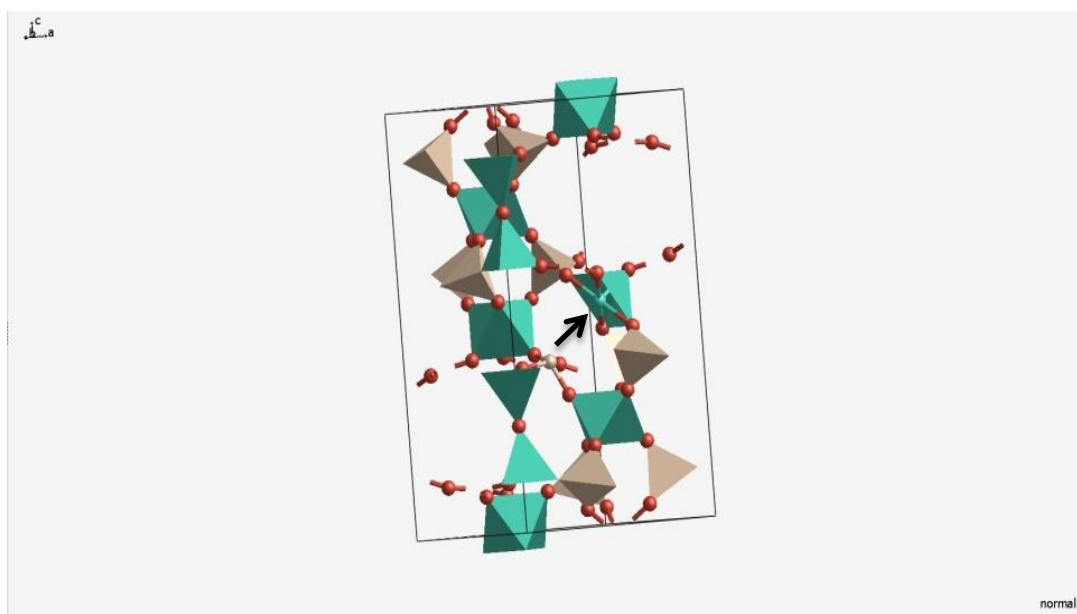


Figure 64. The movement of an atom from the O4 position to the O3 position.

In this pathway the maximum energy occurs at point 8 of the pathway. This leads to an activation energy of 2.12 eV with the activation energy of the reverse reaction being 2.51 eV. Unlike the previous movement, this mechanism actually has a lower activation barrier for the forward reaction in structure II than when compared to the mechanism in the structure I. The activation energy has decreased by 0.04 eV for the forward reaction while increasing by 0.13 for the reverse reaction. After HSE single point calculations were conducted the forward and reverse activation energies increase in energy to 2.76 eV and 3.34 eV respectively. We find that this does not significantly change the

relationship between the energies of structure I and structure II significantly as the forward reaction is 0.1 eV lower in energy while the reverse reaction is 0.14 eV higher in energy when compared to the structure I.

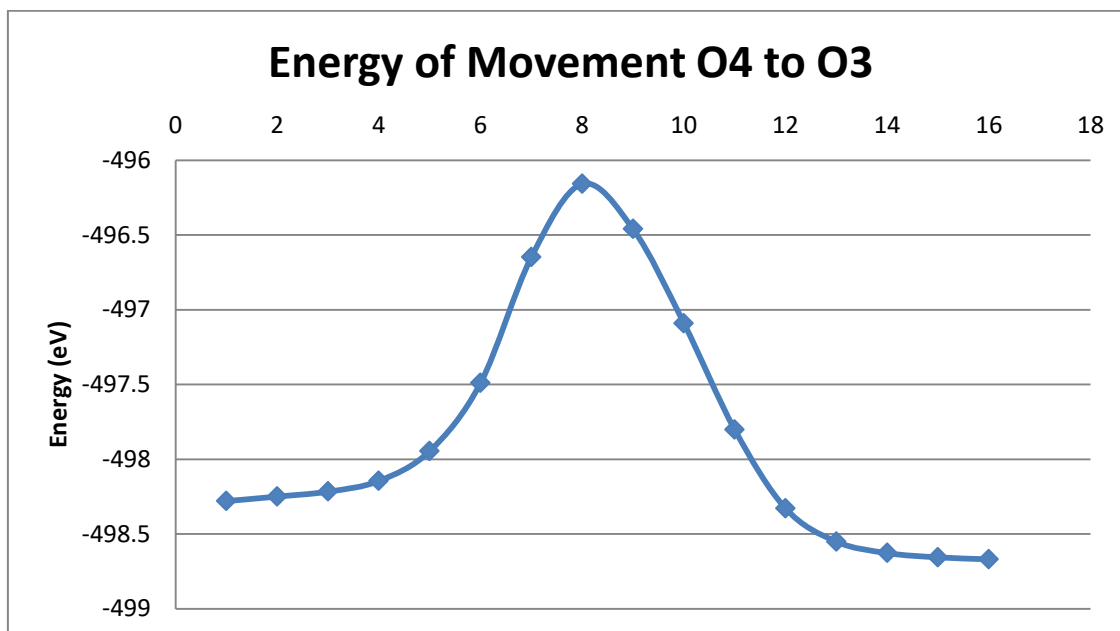


Figure 65. The NEB of the movement of an atom from the O4 position to the O3 position.

2.6.2.3. Movement O3 to O3

The next movement investigated was an intra-molecular movement of an oxygen atom within an octahedron (O3 to O3) which when combined with the movements of an oxygen from the O1 to the O4 position and the O4 to the O3 position allows for a full mechanism through the a/b – axis (See figure 66).

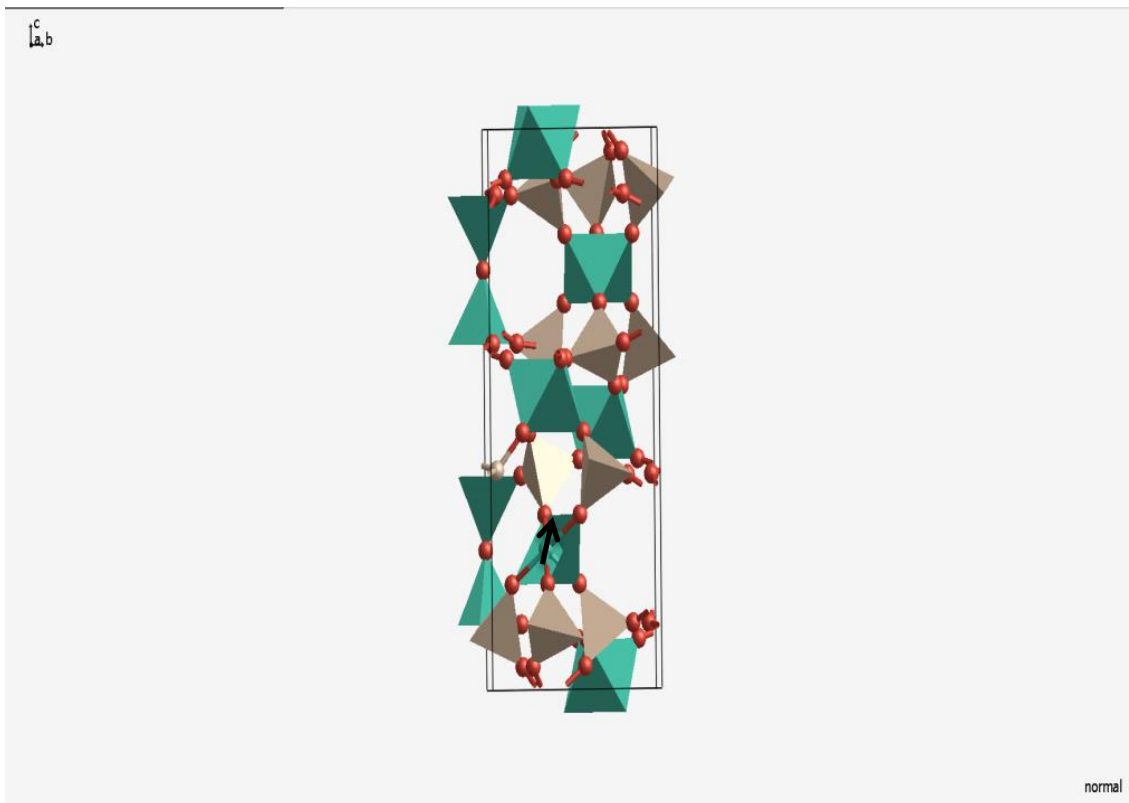


Figure 66. The movement of an oxygen atom from one O3 site to another O3 site within the same octahedron.

The initial results of the NEB calculated using the PBE functional results in the following energy pathway:

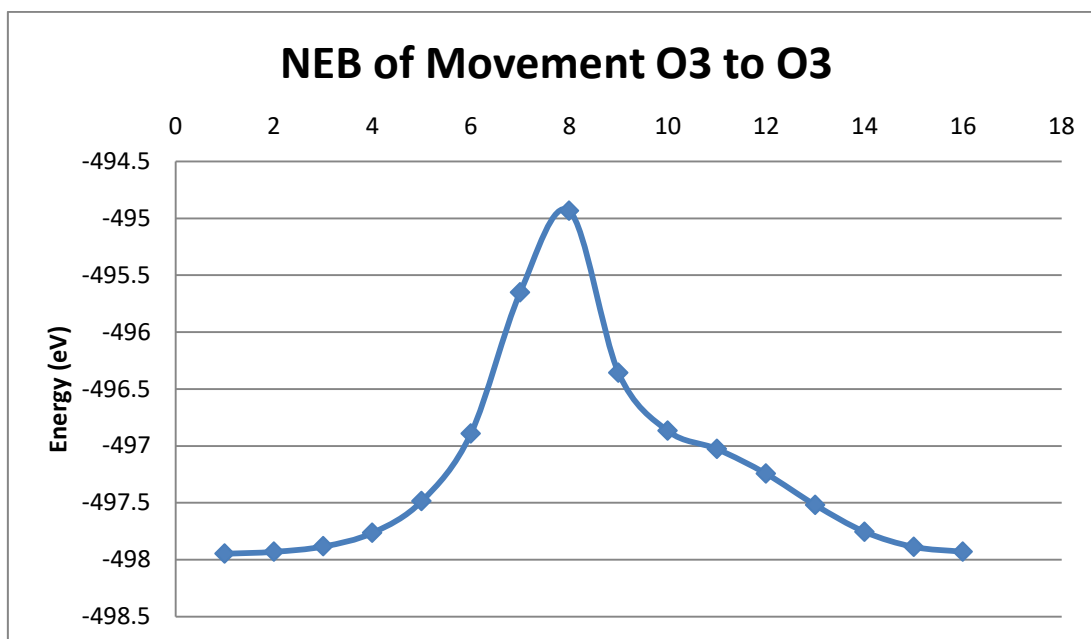


Figure 67. The NEB of the movement of an oxygen from one O3 site to another O3 site within the same octahedron.

In this pathway point 8 is again the energy maximum. The activation energy for this movement is found to be 3.01 eV with the reverse activation energy being 3.00 eV. We would normally expect the forward and reverse energy to be exactly equal to each other as we see in the normal structure due to the fact that this movement is between two equivalent O3 sites. This slight change in energy could be explained by a local energy minima being located very close to the energy minima of the O3 site. This activation energy is roughly 0.52 eV lower in energy than its equivalent in structure I. After the completion of an HSE single point calculation the activation energy increases to 3.70 eV and 3.72 eV respectively for the forward and reverse reactions. This is roughly 0.61-0.62 eV lower than the HSE calculated activation energy of the original pathway.

2.6.2.4. Movement O4 to O5

After studying at all movements allowing movement along the A/B axis, the movement from the bi-pyramid to the octahedron above it through the interstitial space was then investigated (See figure 68).

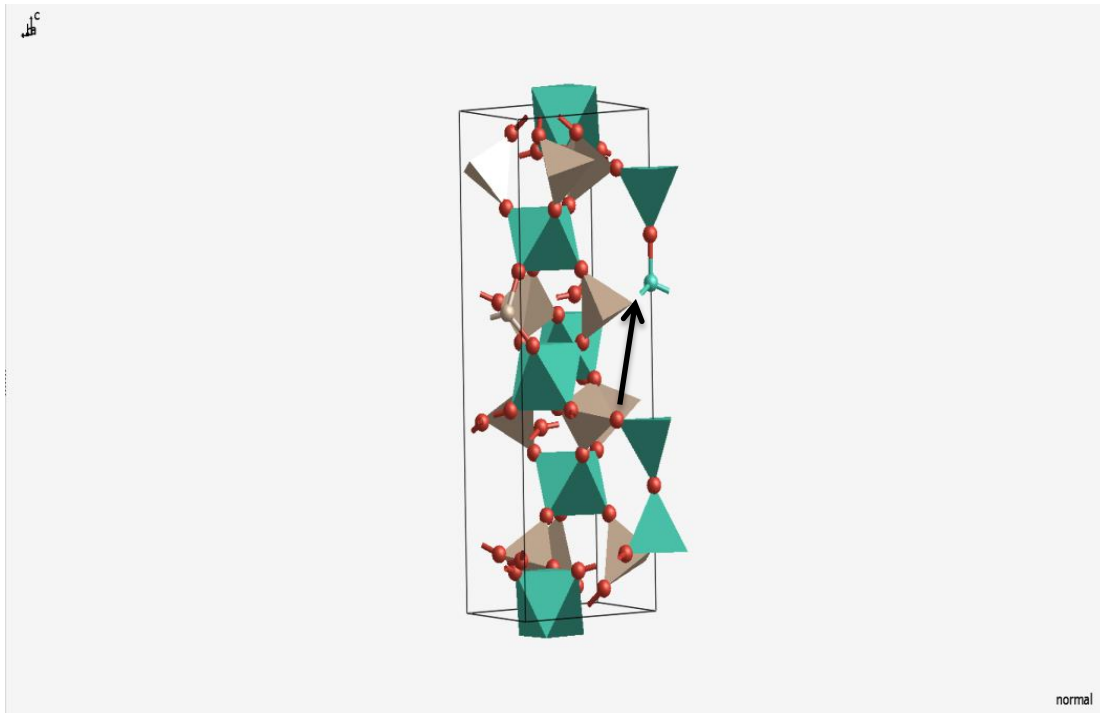


Figure 68. The movement of an oxygen from an O4 site to a vacant O5 site through the interstitial space

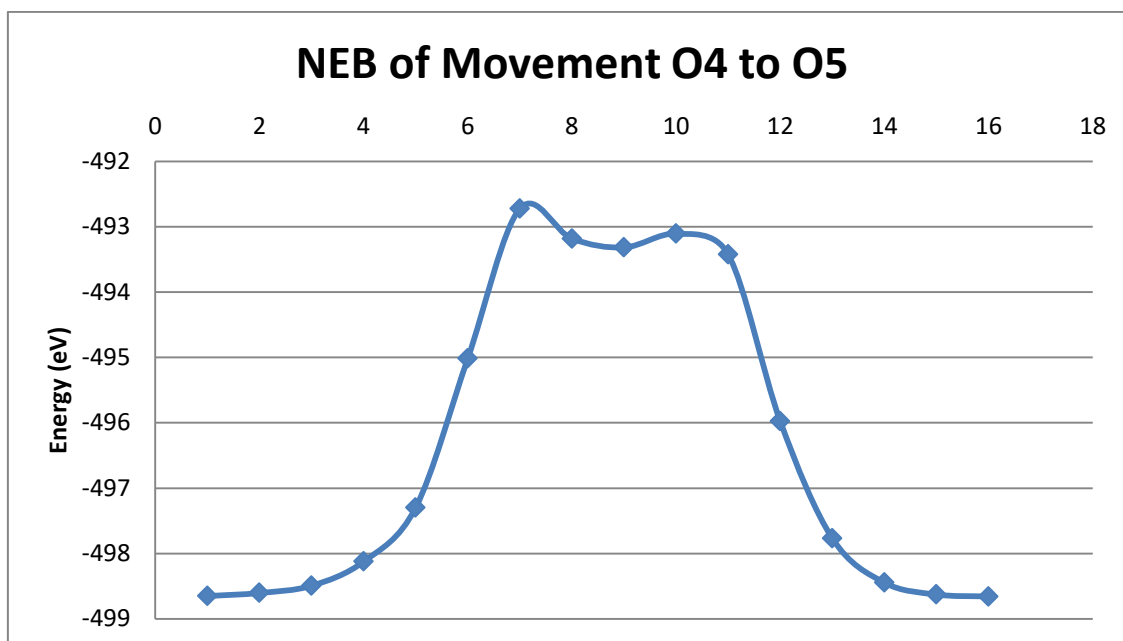


Figure 69. The CI-NEB of the movement of an oxygen atom from an O4 site to a vacant O5 site through the interstitial space as calculated using the PBE functional.

It is found that similar to its counterpart in structure I, this movement contains two energy maxima, this time at points 7 and 10, of which point 7 is the overall energy maximum. The activation energy of the forward reaction is found to be 5.93 eV with the activation energy of the reverse reaction being 5.94 eV. As this movement has a higher energy than any movement belonging to the mechanism for the migration of oxygen through a/b-axis no HSE single point calculations are carried out due to their computational cost.

2.6.2.5. Movement O2 to O3

The last movement investigated as part of this mechanism was the movement of an oxygen atom between two octahedra connected via a PO4 group (See figure 70).

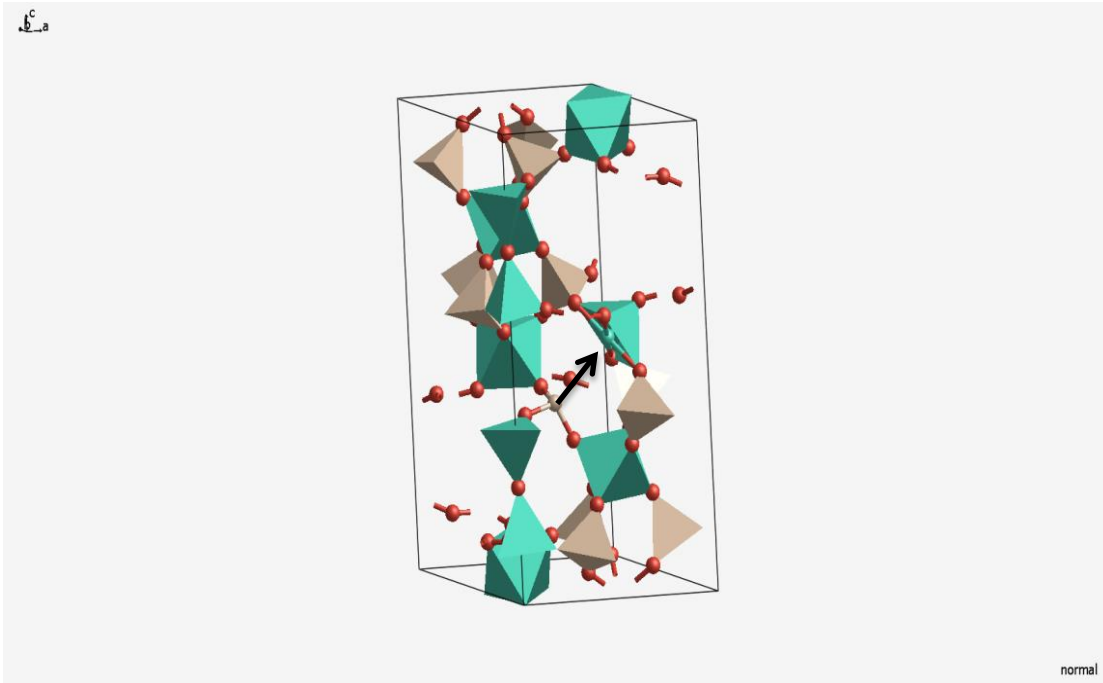


Figure 70. The movement of an atom from an O2 site to an O3 site present on an adjacent octahedron

The initial NEB results gave the following pathway structure:

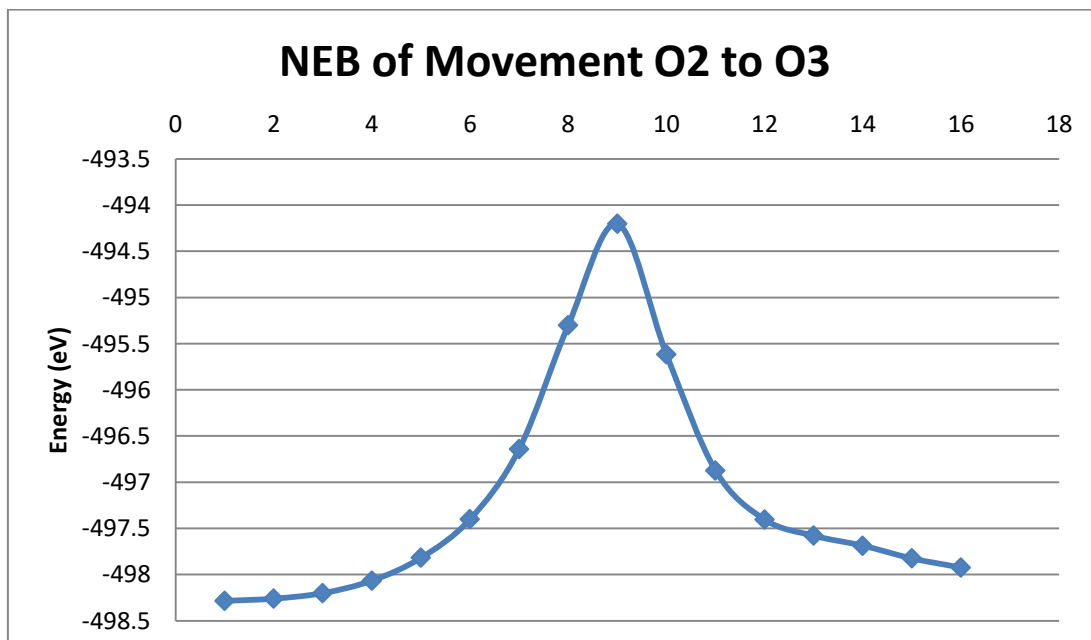


Figure 71. The NEB of the movement of an atom from an O2 site to an O3 site present on an adjacent octahedron.

This movement is yet again found not to be part of the lowest energy mechanism for the transport of oxygen, with an energy maximum at point 9. The activation energy of this movement was found to be 4.08 eV with the reverse activation energy being 3.72 eV. As this movement is not part of the lowest energy pathway no HSE calculations were undertaken.

2.6.2.6. Lowest Energy Full Movement

By comparing all of the different movement types we can determine that the lowest energy pathway through the cell will use movements O1-O4, O4-O3 and O3-O3. By combining these movements a migration pathway can be created along the a/b-axis of the unit cell (See figure 72).

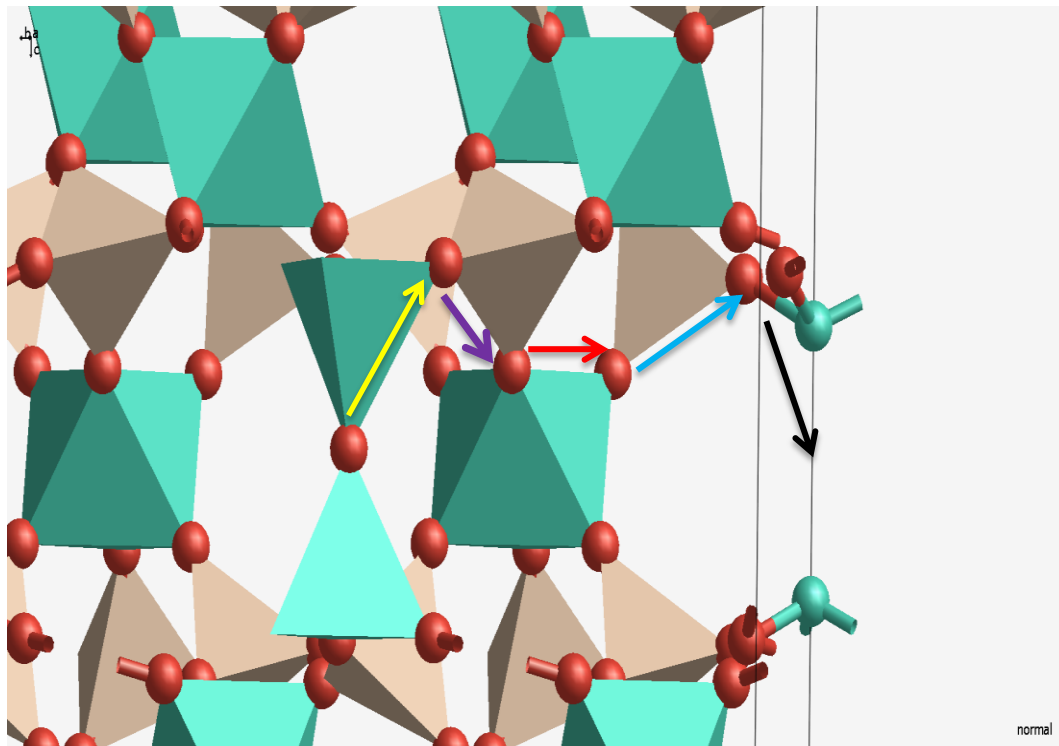


Figure 72. The full vacancy mechanism through the a/b axis of the cell.

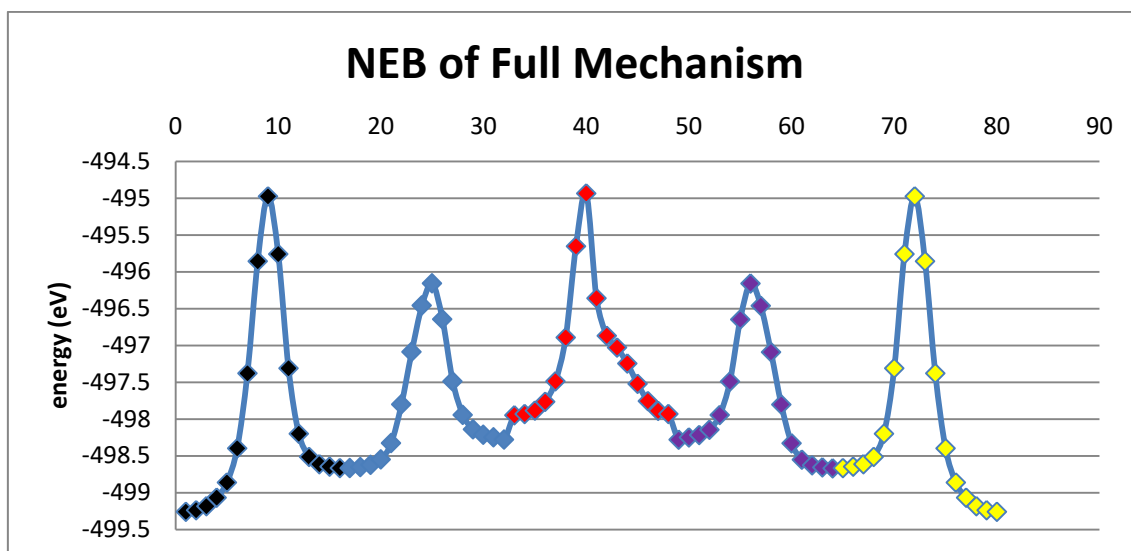


Figure 73. The NEB of the full vacancy mechanism. The colours represent the regions of the NEB related to the different movements shown in figure 70.

This profile shows the results from the PBE based NEB calculations and has an activation energy of 4.32 eV. When the results from the HSE single point calculations are used this is increased to 5.32 eV.

Even though it uses the same movements, this pathway is 0.52 eV lower than the vacancy pathway calculated for structure I. However this pathway also has an activation which is still over an order of magnitude larger than the experimentally determined energy.

2.6.2.7. Interstitialcy Mechanism

As is the case of structure I, the final mechanism investigated was an interstitially mechanism where an additional oxygen atom sits in an interstitial site beside the O1 atom and pushes it along the a/b axis to start a mechanism similar to the minimum energy pathway seen in the vacancy study. This pathway is the same pathway investigated during our tests of structure I (see figure 74).

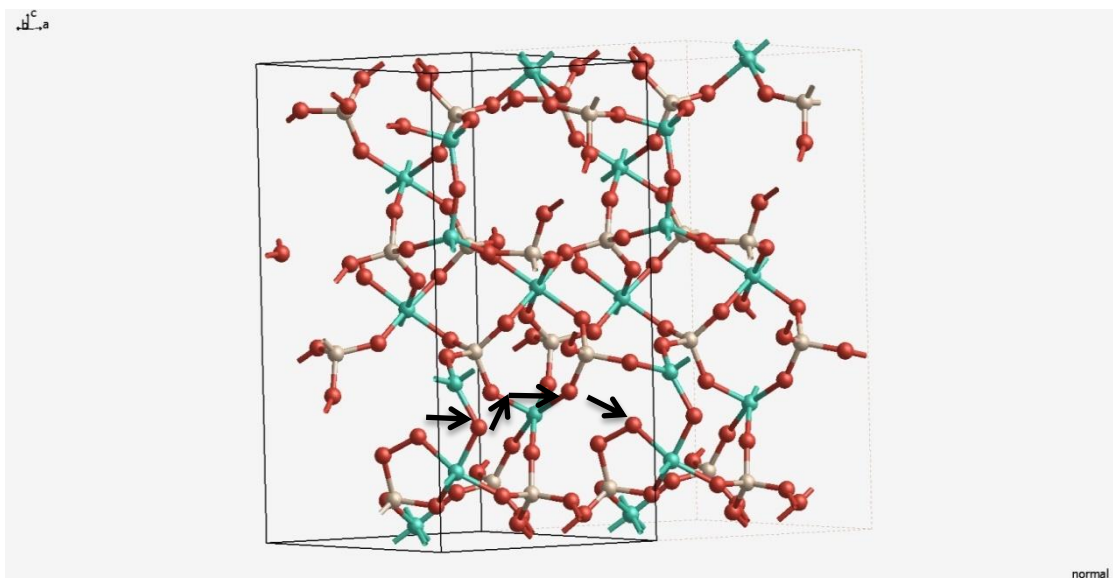


Figure 74. The full mechanism for movement along the a/b axis using an interstitialcy mechanism.

The initial NEB results gave the following pathway structure:

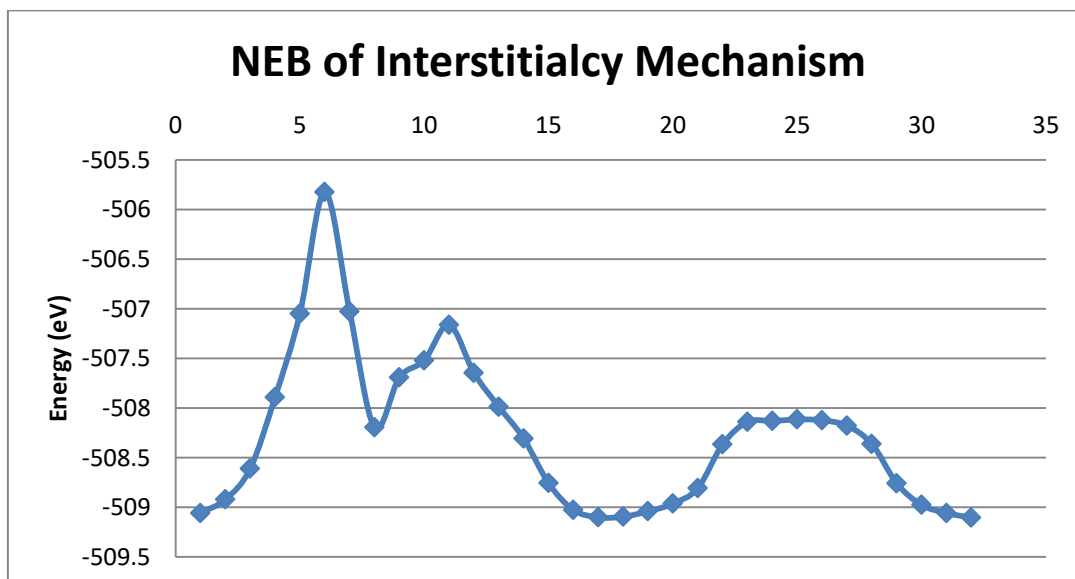


Figure 75. The CI-NEB as calculated using the PBE functional.

In this 32 image pathway we can see that the maximum energy is found at point 6. This graph shows that when going from point 11 to point 32 the activation energy is 3.23 eV,

with the reverse energy being 3.28 eV. After the HSE single point calculations were carried out the activation energies increase to 3.78 eV and 3.75 eV respectively.

We can see that the energy of this mechanism is significantly higher than its counterpart in structure I, being 1.72 eV higher. Similar to the structure I, this pathway is the lowest energy pathway seen in structure II.

2.6.3. Conclusion

It is clear from our results that further study is needed in order to determine the experimentally active migration pathway with the lowest pathway discovered being 1.7 eV (a factor of more than five) higher than the activation energy determined by the AC impedance experiments.

Mechanism type	Activation energy of mechanism in structure I (eV)	Activation energy of mechanism in structure II (eV)
Rotation of Tetrahedron	5.62	6.76
Vacancy Mechanism	5.84	5.32
Interstitialcy Mechanism	2.03	3.78

Table 7. The activation energies of the lowest energy vacancy and interstitialcy pathways in structure I and structure II. As well as the activation energy for the rotation of the tetrahedron.

We would suggest that this study focus on two areas that we were unable to look at within the given time frame. The first area of study would be the interface between structure I and structure II, as well as looking at the formation of structure II in order to determine if these interactions reduce the activation energy.

Chapter 5 – Conclusions and Future Work

The work in this thesis concentrated on the computational investigation of the materials copper doped ceria and $\text{Ge}_5\text{O}(\text{PO}_4)_6$.

In the case of our first project investigating copper doped ceria, first principles generated thermodynamic data, as well as pre-existing experimental data, was used to generate a thermodynamic database in order to investigate how differences in partial oxygen pressure, and temperature, changed both the ionic structure of the material, and the overall copper doping percentage.

The initial first principles study showed that the doped copper consisted of Cu^{1+} and Cu^{2+} ions, with Cu^{1+} being enthalpically more stable at 0 K. Using the full thermodynamic database we were able to show that Cu^{2+} was more stable at lower temperatures and higher oxygen partial pressures with Cu^{1+} becoming dominant at higher temperatures and lower partial pressures.

Using the thermodynamic database we also generated two phase diagrams which showed the phase composition of the Ce-Cu-O system under an oxygen partial pressure comparable to air as well as under a low oxygen partial pressure.

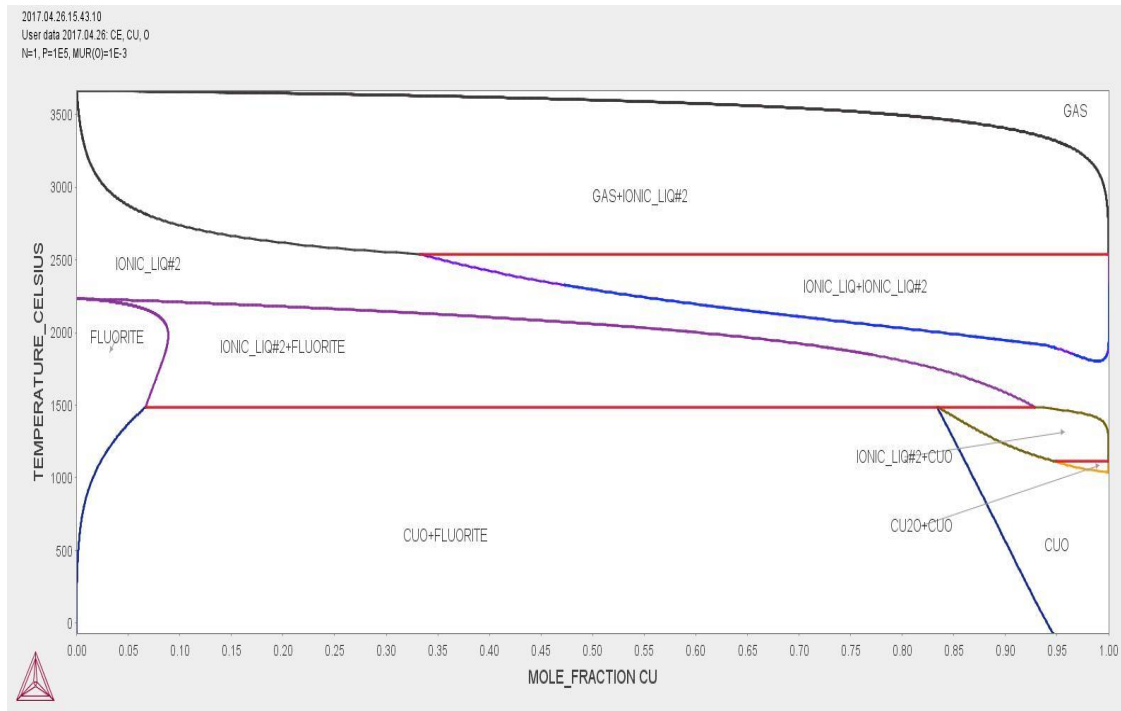


Figure 76. The phase diagram of the Ce-Cu-O system under Air (where the x-axis is cation fraction).

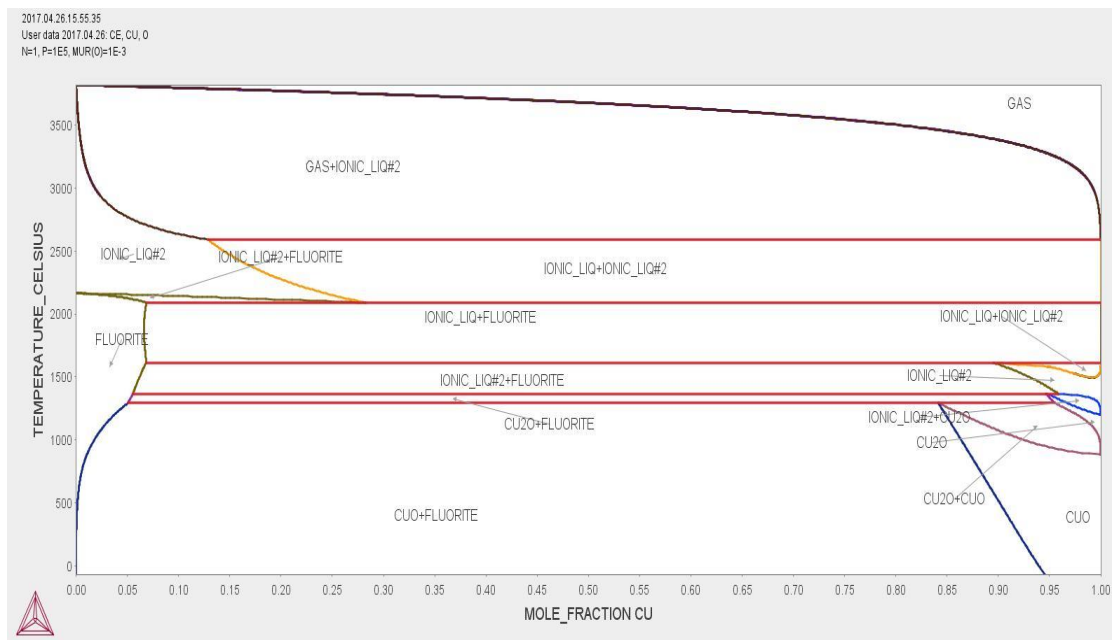


Figure 77. The phase diagram of the Ce-Cu-O system under 1% oxygen (where the x-axis is cation fraction).

From these phase diagrams, we can conclude that the ability of copper to be doped into ceria has a large sensitivity to both the oxygen partial pressure, as well as the temperature with higher doping percentages seen at high temperatures, as well as at higher oxygen partial pressures.

Whilst there are a number of reports of higher copper solubilities than we calculate in air, these probably reflect that the synthesised materials are actually metastable. High temperatures and reducing conditions should assist in dissolving Cu into the ceria lattice, Cu will tend to exsolve out of the structure when used as a catalyst. This is actually a beneficial characteristic of the material as it produces a larger active surface area allowing for copper doped ceria to act as a more effective catalyst.

These results show a potential weakness in our understanding of the phase boundary of the fluorite phase at lower oxygen partial pressure, as we see a decrease in copper solubility at lower oxygen partial pressures. We suggest that the next step in this project would be to investigate the kinetics of copper solubility in copper doped ceria and to compare these to the kinetics of the formation of the copper oxide phases. This would allow us to examine whether the decrease in solubility is due to competition for the copper ions from the copper oxides on the right hand side of the phase diagram.

In our second project, possible oxygen migration pathways in the electrolyte material $\text{Ge}_5\text{O}(\text{PO}_4)_6$ were investigated in order to find a pathway to explain the experimental action energy of oxygen migration of 0.3 eV.

We investigated vacancy, interstitial, and interstitialcy pathways in both $\text{Ge}_5\text{O}(\text{PO}_4)_6$, and a related structure based upon $\text{Ge}_3\text{P}_6\text{Si}_2\text{O}_{25}$. None of these pathways were found to have an activation energy low enough to explain the 0.3 eV experimental reading, with

the lowest energy pathway found to be an interstitialcy pathway through the a/b-axis of the unit cell which had an activation energy of 2.03 eV.

While not finding a path that agrees with experiment, we can rule out the originally proposed mechanism based on oxygen movement along the c-axis of the crystal structure.

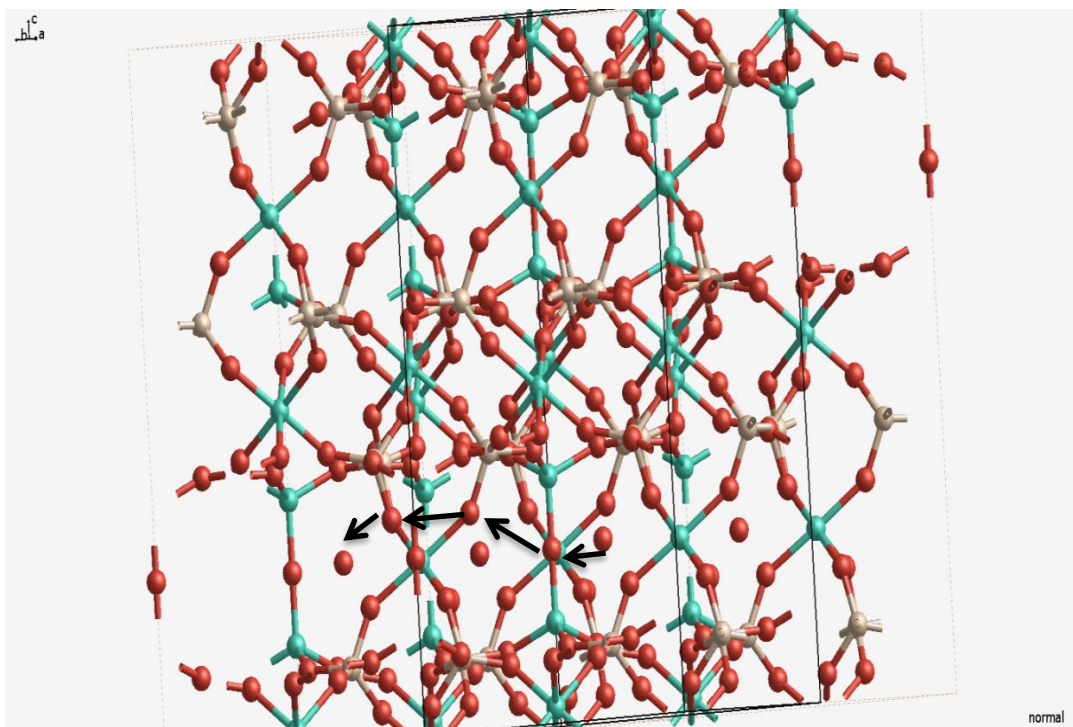


Figure 78. Showing the full mechanism for movement along the a/b axis using an interstitialcy mechanism

We suggest that future work on this project concentrate on the interface between both structural domains, to see whether a mechanism exists in this space that can explain the experimental results.

References

- 1 W. R. Grove, *Philos. Mag. Ser. 3*, 1839, **14**, 127–130.
- 2 B. C. Steele and A. Heinzl, *Nature*, 2001, **414**, 345–352.
- 3 Y. Zhao, C. Xia, L. Jia, Z. Wang, H. Li, J. Yu and Y. Li, *Int. J. Hydrogen Energy*, 2013, **38**, 16498–16517.
- 4 A. West, *Solid State Chemistry and its Applications, 2nd Edition, Student Edition*, Wiley, Chichester, 2014.
- 5 J. B. Goodenough, *Proc. R. Soc. London. Ser. A*, 1984, **393**, 215–234.
- 6 P. P. Kumar and S. Yashonath, *J. Chem. Sci.*, 2006, **37**, 135–154.
- 7 M. Tham, PhD thesis, University of St. Andrews, 2015.
- 8 H. Mehrer, *Diffusion in solids: fundamentals, methods, materials, diffusion-controlled processes*, Springer, Berlin, 2007.
- 9 J. B. Goodenough, *Annu. Rev. Mater. Res.*, 2003, **33**, 91–128.
- 10 P. Knauth and H. L. Tuller, *J. Am. Ceram. Soc.*, 2004, **85**, 1654–1680.
- 11 R. Ramamoorthy, P. K. Dutta and S. a Akbar, *J. Mater. Sci.*, 2003, **38**, 4271–4282.
- 12 J. A. Kilner, *Solid State Ionics*, 2000, **129**, 13–23.
- 13 L. Malavasi, C. A. J. Fisher and M. S. Islam, *Chem. Soc. Rev.*, 2010, **39**, 4370–4387.

- 14 J. C. Boivin and G. Mairesse, *Chem. Mater.*, 1998, **10**, 2870–2888.
- 15 T. H. Etsell and S. N. Flengas, *Chem. Rev.*, 1970, **70**, 339–376.
- 16 J. W. Fergus, *J. Power Sources*, 2006, **162**, 30–40.
- 17 V. V. Kharton, F. M. B. Marques and A. Atkinson, *Solid State Ionics*, 2004, 174, 135–149.
- 18 S. Hull, *Reports Prog. Phys.*, 2004, **67**, 1233–1314.
- 19 J. T. S. Irvine, J. W. L. Dobson, T. Politova, S. G. Martin and A. Shenouda, *Faraday Discuss.*, 2007, **134**, 41-49-118, 415–419.
- 20 R. D. Shannon, *Acta Crystallogr. Sect. A*, 1976, **32**, 751–767.
- 21 S. J. Skinner and J. A. Kilner, *Mater. Today*, 2003, **6**, 30–37.
- 22 S. Nakayama and M. Sakamoto, *J. Eur. Ceram. Soc.*, 1998, **18**, 1413–1418.
- 23 J. E. H. Sansom, D. Richings and P. R. Slater, *Solid State Ionics*, 2001, **139**, 205–210.
- 24 P. R. Slater, J. E. H. Sansom and J. R. Tolchard, *Chem. Rec.*, 2004, 4, 373–384.
- 25 J. R. Tolchard, M. S. Islam and P. R. Slater, *J. Mater. Chem.*, 2003, **13**, 1956–1961.
- 26 M. S. Islam, J. R. Tolchard and P. R. Slater, *Chem. Commun.*, 2003, 1486–1487.
- 27 H. Mayer and H. Völlenknecht, *Monatshefte für Chemie / Chem. Mon.*, 1972, **103**, 1560–1571.

- 28 I. Mal'shikov, A. E., Egorova, O. V. & Bondar and A., *Russ. J. Inorg. Chem.*, 1988, **33**, 722–726.
- 29 H. Mayer, *Monatshefte für Chemie / Chem. Mon.*, 1974, **105**, 46–54.
- 30 D. M. Poojary, R. B. Borade and A. Clearfield, *Inorg. Chim. Acta*, 1993, **208**, 23–29.
- 31 A. B. Kehoe, D. O. Scanlon and G. W. Watson, *Chem. Mater.*, 2011, **23**, 4464–4468.
- 32 F. Yang, J. Wei, W. Liu, J. Guo and Y. Yang, *J. Mater. Chem. A*, 2014, **2**, 5662.
- 33 Y. Li, Q. Fu and M. Flytzani-Stephanopoulos, *Appl. Catal. B Environ.*, 2000, **27**, 179–191.
- 34 R. Si, J. Raitano, N. Yi, L. Zhang, S.-W. Chan and M. Flytzani-Stephanopoulos, *Catal. Today*, 2012, **180**, 68–80.
- 35 J. S. Elias, M. Risch, L. Giordano, A. N. Mansour and Y. Shao-Horn, *J. Am. Chem. Soc.*, 2014, **136**, 17193–17200.
- 36 S. Li, N. Wang, Y. Yue, G. Wang, Z. Zu and Y. Zhang, *Chem. Sci.*, 2015, **6**, 2495–2500.
- 37 S. Brunauer, P. H. Emmett and E. Teller, *J. Am. Chem. Soc.*, 1938, **60**, 309–319.
- 38 W. Zhu, K. Tang, J. Li, W. Liu, X. Niu, G. Zhao, X. Ma, Z. Liu, H. Wei and Y. Yang, *RSC Adv.*, 2016, **6**, 46966–46971.
- 39 J. Giménez-Mañogil and A. García-García, *Appl. Catal. A Gen.*, 2017, **542**, 226–

- 239.
- 40 K. Rao, P. Venkataswamy and A. Reddy, *Ind.Eng.Chem.Res*, 2011, **50**, 11960–11969.
- 41 R. Dziembaj, M. Molenda, L. Chmielarz, M. M. Zaitz, Z. Piwowarska and A. Rafalska-Łasocha, *Catal. Today*, 2011, **169**, 112–117.
- 42 L. Kaufman and H. Bernstein, *Computer Calculation of Phase Diagrams with Special Reference to Refractory Metals*, Academic Press, New York, 1970.
- 43 L. Kaufman, *Calphad*, 2001, **25**, 141–161.
- 44 N. Saunders and A. P. Miodownik, *CALPHAD Calculation of Phase Diagrams - A Comprehensive Guide*, Pergamon, 1998, vol. 1.
- 45 L. Holroyd, PhD Thesis, University of St. Andrews, 2015.
- 46 M. Born and R. Oppenheimer, *Ann. Phys.*, 1927, **389**, 457–484.
- 47 C. J. Cramer, *Essentials of Computational Chemistry Theories and Models*, 2nd Ed., John Wiley and Sons, Chichester, 2004.
- 48 W. Hohenberg, P.; Kohn, *Phys. Rev.*, 1964, **136**, B864–B871.
- 49 T. K. Shires, *Arch. Biochem. Biophys.*, 1975, **171**, 695–707.
- 50 W. Kohn and L. J. Sham, *Phys. Rev.*, 1965, **140**.
- 51 J. Perdew, K. Burke and M. Ernzerhof, *Phys. Rev. Lett.*, 1996, **77**, 3865–3868.
- 52 Z. Yang, G. Luo, Z. Lu and K. Hermansson, *J. Chem. Phys.*, 2007, **127**.

- 53 I. Yeriskin and M. Nolan, *J. Phys. Condens. Matter*, 2010, **22**.
- 54 M. Huang and S. Fabris, *J. Phys. Chem. C*, 2008, **112**, 8643–8648.
- 55 J. Heyd, G. E. Scuseria and M. Ernzerhof, *J. Chem. Phys.*, 2006, **124**, 219906.
- 56 S. Grimme, *J. Comput. Chem.*, 2006, **27**, 1787–1799.
- 57 S. Grimme, J. Antony, S. Ehrlich and H. Krieg, *J. Chem. Phys.*, 2010, **132**.
- 58 G. Kresse and J. Hafner, *Phys. Rev. B*, 1993, **47**, 558–561.
- 59 G. Kresse and J. Hafner, *Phys. Rev. B*, 1994, **49**, 14251–14269.
- 60 G. Kresse and J. Furthmüller, *Comput. Mat. Sci.*, 1996, **6**, 15.
- 61 H. J. Graeme Henkelman , Gísli Jóhannesson, in *Progress on Theoretical Chemistry and Physics*, Kluwar Academic Publishers, 2000, pp. 269–300.
- 62 G. Henkelman, B. P. Uberuaga and H. Jónsson, *J. Chem. Phys.*, 2000, **113**, 9901–9904.
- 63 A. Togo and I. Tanaka, *Scr. Mater.*, 2015, **108**, 1–5.
- 64 P. J. Spencer, *Calphad Comput. Coupling Phase Diagrams Thermochem.*, 2008, **32**, 1–8.
- 65 J. O. Andersson, T. Helander, L. Höglund, P. Shi and B. Sundman, *Calphad Comput. Coupling Phase Diagrams Thermochem.*, 2002, **26**, 273–312.
- 66 O. Redlich and A. T. Kister, *Ind. Eng. Chem.*, 1948, **40**, 345–348.

- 67 M. Zinkevich, D. Djurovic and F. Aldinger, *Solid State Ionics*, 2006, **177**, 989–1001.
- 68 L. Schramm, G. Behr, W. Löser and K. Wetzig, *J. Phase Equilibria Diffus.*, 2005, **26**, 605–612.
- 69 M. Hillert, *J. Alloys Compd.*, 2001, **320**, 161–176.
- 70 G. Kresse and J. Hafner, *J. Phys. Condens. Matter*, 1994, **6**, 8245–8257.
- 71 L. Y. Issero and E. A. Carter, *Chem. Mater.*, 2013, **25**, 253–265.
- 72 M. Chase Jr., *J. Phys. Chem. Ref. Data*, 1998, 1952.
- 73 A. T. Dinsdale, *Calphad*, 1991, **15**, 317–425.
- 74 T. Jan, J. Iqbal, Q. Mansoor, M. Ismail and M. S. Haider, *J. Phys. D Appl. Phys.*, 2014, **355301**.
- 75 A. Sikora, E. Bukowska and R. Horyn, *ACTA Phys. Pol. A*, 2004, **106**, 727–731.
- 76 P. Aunbamrung and A. Wongkaew, *Adv. Chem. Eng. Sci.*, 2013, **2013**, 15–19.
- 77 A. Tschope, M. L. Trudeau and J. Y. Ying, *J. Physical Chem. B*, 1999, **103**, 8858–8863.
- 78 D. Gamarra, G. Munuera, A. B. Hungia, M. Ferna and A. Martí, *J. Phys. Chem. C*, 2007, **111**, 11026–11038.
- 79 A. Leclaire and B. Raveau, *J. Solid State Chem.*, 1988, **75**, 397–402.
- 80 D. Colleoni and A. Pasquarello, *J. Phys. Condens. Matter*, 2016, **28**, 495801.

- 81 D. A. Andersson, S. I. Simak, N. V. Skorodumova, I. A. Abrikosov and B. Johansson, *Proc. Natl. Acad. Sci.*, 2006, **103**, 3518–3521.
- 82 J. Faber, C. Geoffroy, A. Roux, A. Sylvestre and P. Abélard, *Appl. Phys. A Solids Surfaces*, 1989, **49**, 225–232.

Appendix A: Thermodynamic database of the Ce-Cu-O system

Database file used in the Thermocalc Program.

File has a .TCM file extension.

When opened in Thermocalc the file provides the program with the thermodynamic information of the Ce-Cu-O system in a format readable by the program.

```
@@ Setup file written 12/03/2015
```

```
@@ Database:USER
```

```
go gibbs
```

```
ent-el /- VA CE O CU
```

```
am_el_d /- ELECTRON_GAS      0.0000E+00 0.0000E+00 0.0000E+00 1
```

```
am_el_d VA VACUUM          0.0000E+00 0.0000E+00 0.0000E+00 1
```

```
am_el_d CE FCC_A1         1.4012E+02 0.0000E+00 1.6600E+01 2
```

```
am_el_d O 1/2_MOLE_O2(G)   1.5999E+01 0.0000E+00 2.4502E+01 2
```

```
am_el_d CU FCC_A1         6.3546E+01 5.0041E+03 3.3150E+01 1
```

```
enter-specie CE+2          CE1/+2
```

```
enter-specie CE+3          CE1/+3
```

```
enter-specie CE+4          CE1/+4
```

```
enter-specie CE2O3         CE2O3
```

```
enter-specie CEO           CE1O1
```

```
enter-specie CEO2          CE1O2
```

```
enter-specie CEO3/2        CE1O1.5
```

```
enter-specie CU2           CU2
```

enter-specie CUO CU1O1
 enter-specie CU2O CU2O1
 enter-specie O-2 O1/-2
 enter-specie O2 O2
 enter-specie O3 O3
 ENTER-SPECIES CU+1 CU/+1
 ENTER-SPECIES CU+2 CU/+2
 ENTER-SPECIES CU+3 CU/+3

@@ Warning: Functions may not be in correct order

@@ Move all "set-fix" to the end before create work

@@ Other constants or variables may need editing

@@ ++++++ Gibbs energy functions

@@ oxgen function, 1/2 Os (Dinsdale 1991)

ent-sym fun GHSEROO 298 -3480.87-25.503038*T-11.136*T*LN(T)
 -0.005098888*T**2+6.61846E-07*T**3-38365*T**(-1); 1000 Y
 -6568.763+12.65988*T-16.8138*T*LN(T)-5.95798E-04*T**2+6.781E-09*T**3
 +262905*T**(-1); 3300 Y
 -13986.728+31.259625*T-18.9536*T*LN(T)-4.25243E-04*T**2
 +1.0721E-08*T**3+4383200*T**(-1); 6000 N

@@ Cerium functions (Dinsdale 1991)

ent-sym fun GLIQCE 298 +4117.865-11.423898*T-7.5383948*T*LN(T)

$-.02936407 * T^{**2} + 4.827734E-06 * T^{**3} - 198834 * T^{**(-1)}$; 1000 Y
 $-6730.605 + 183.023193 * T - 37.6978 * T * \text{LN}(T)$; 4000 N
 ent-sym fun GBCCCE 298 $-1354.69 - 5.21501 * T - 7.7305867 * T * \text{LN}(T)$
 $-.029098402 * T^{**2} + 4.784299E-06 * T^{**3} - 196303 * T^{**(-1)}$; 1000 Y
 $-12101.106 + 187.449688 * T - 37.6142 * T * \text{LN}(T)$; 1072 Y
 $-11950.375 + 186.333811 * T - 37.4627992 * T * \text{LN}(T) - 5.7145E-05 * T^{**2}$
 $-25897 * T^{**(-1)} + 2.348E-09 * T^{**3}$; 4000 N
 ent-sym fun GHSERCE 298 $-7160.519 + 84.23022 * T - 22.3664 * T * \text{LN}(T) -$
 $.0067103 * T^{**2}$
 $-3.20773E-07 * T^{**3} - 18117 * T^{**(-1)}$; 1000 Y
 $-79678.506 + 659.4604 * T - 101.32248 * T * \text{LN}(T) + .026046487 * T^{**2}$
 $-1.930297E-06 * T^{**3} + 11531707 * T^{**(-1)}$; 2000 Y
 $-14198.639 + 190.370192 * T - 37.6978 * T * \text{LN}(T)$; 4000 N

@@ cerium oxide functions (Zinkevich)

ent-sym fun GCE2O3LQ 298.15 $+126654 - 54.497 * T + \text{GCE2O3}$; 6000 N

ent-sym fun GCEO2LQ 298.15 $+87177 - 29.059 * T + \text{GCEO2}$; 6000 N

ent-sym fun GCE2O3F 298.15 $-1804481 + 1067.043 * T - 175.3336 * T * \text{LN}(T)$

$-6.498627E-04 * T^{**2} + 546000 * T^{**(-1)}$; 6000 N

ent-sym fun GCEO2 298.15 $-1116518 + 434.8839 * T - 72.866 * T * \text{LN}(T) - .003992 * T^{**2}$

$+602000 * T^{**(-1)}$; 6000 N

ent-sym fun GCEO 298.15 $+.3333333 * \text{GCE2O3} + .3333333 * \text{GHSERCE}$; 6000 N

ent-sym fun GCE2O3 298.15 $-1832858 + 667.3306 * T - 119.855 * T * \text{LN}(T)$

$-.012155 * T^{**2} + 546000 * T^{**(-1)}$; 6000 N

ent-sym fun GCE2O3C 298.15 $+4390 + 7.232 * T + \text{GCE2O3}$; 6000 N

ent-sym fun GCEO2C 298.15 +9570+GCEO2 ; 6000 N

ent-sym fun GCE2O3H 298.15 +32699-13.986*T+GCE2O3 ; 6000 N

ent-sym fun GCE2O3X 298.15 +43724-18.555*T+GCE2O3 ; 6000 N

@@cerium and cerium oxide gas functions (SGTE-SSUB4)

ent-sym fun F5574T 298 +415522.823-162.335296*T-2.278004*T*LN(T)

-0.03027047*T**2+4.49130167E-06*T**3-235655.4*T**(-1); 800 Y

+394890.236+79.9289911*T-38.12366*T*LN(T)-.002449024*T**2

+4.15102E-07*T**3+1999448*T**(-1); 1500 Y

+390359.041+141.264497*T-47.09829*T*LN(T)+.0033852315*T**2

-2.141025E-07*T**3+1961344*T**(-1); 3200 Y

+435081.796-76.3952519*T-19.26359*T*LN(T)-.0038954345*T**2

+1.30156067E-07*T**3-10269705*T**(-1); 5900 Y

+209079.977+456.525021*T-81.18395*T*LN(T)+.00366283*T**2

-4.30937833E-08*T**3+1.449331E+08*T**(-1); 10000 N

ent-sym fun F5626T 298 -140721.775-55.35698*T-26.80191*T*LN(T)

-0.018793285*T**2+3.20697333E-06*T**3+78887.25*T**(-1); 800 Y

-156451.4+135.868596*T-55.26216*T*LN(T)+.004151018*T**2

-2.71056167E-07*T**3+1712598*T**(-1); 2800 Y

-145347.823+72.3320205*T-46.90508*T*LN(T)+.0014029315*T**2

-1.06263967E-07*T**3-1106602.5*T**(-1); 6000 N

ent-sym fun F12657T 298 +243206.494-20.8612582*T-21.01555*T*LN(T)

+1.2687055E-04*T**2-1.23131283E-08*T**3-42897.09*T**(-1); 2950 Y

+252301.423-52.0847281*T-17.21188*T*LN(T)-5.413565E-04*T**2

+7.64520667E-09*T**3-3973170.5*T**(-1); 6000 N

ent-sym fun F12999T 298 -6960.6927-51.1831467*T-22.25862*T*LN(T)

$-.01023867*T^{**2}+1.339947E-06*T^{**3}-76749.55*T^{**(-1)}$; 900 Y
 $-13136.0174+24.7432966*T-33.55726*T*LN(T)-.0012348985*T^{**2}$
 $+1.66943333E-08*T^{**3}+539886*T^{**(-1)}$; 3700 Y
 $+14154.6459-51.485458*T-24.47978*T*LN(T)-.002634759*T^{**2}$
 $+6.01544333E-08*T^{**3}-15120935*T^{**(-1)}$; 9600 Y
 $-314316.629+515.068037*T-87.56143*T*LN(T)+.0025787245*T^{**2}$
 $-1.878765E-08*T^{**3}+2.9052515E+08*T^{**(-1)}$; 18500 Y
 $-108797.175+288.483019*T-63.737*T*LN(T)+.0014375*T^{**2}-9E-09*T^{**3}$
 $+ .25153895*T^{**(-1)}$; 20000 N

ent-sym fun F13287T 298 +130696.944-37.9096643*T-27.58118*T*LN(T)

$-.02763076*T^{**2}+4.60539333E-06*T^{**3}+99530.45*T^{**(-1)}$; 700 Y
 $+114760.623+176.626737*T-60.10286*T*LN(T)+.00206456*T^{**2}$
 $-5.17486667E-07*T^{**3}+1572175*T^{**(-1)}$; 1300 Y
 $+49468.3956+710.09482*T-134.3696*T*LN(T)+.039707355*T^{**2}$
 $-4.10457667E-06*T^{**3}+12362250*T^{**(-1)}$; 2100 Y
 $+866367.075-3566.80563*T+421.2001*T*LN(T)-.1284109*T^{**2}$
 $+5.44768833E-06*T^{**3}-2.1304835E+08*T^{**(-1)}$; 2800 Y
 $+409416.383-1950.70834*T+223.4437*T*LN(T)-.0922361*T^{**2}$
 $+4.306855E-06*T^{**3}-21589870*T^{**(-1)}$; 3500 Y
 $-1866338.6+6101.13383*T-764.8435*T*LN(T)+.09852775*T^{**2}$
 $-2.59784667E-06*T^{**3}+9.610855E+08*T^{**(-1)}$; 4900 Y
 $+97590.043+890.798361*T-149.9608*T*LN(T)+.01283575*T^{**2}$
 $-3.555105E-07*T^{**3}-2.1699975E+08*T^{**(-1)}$; 6000 N

@@copper and copper oxide gas functions (SGTE-SSUB4)

ent-sym fun F8167T 2.98150E+02 +331712.276-25.5445936*T-21.044*T*LN(T)

$+2.776E-04*T^{**2}-4.9305E-08*T^{**3}+5295*T^{**(-1)}$; 1.60000E+03 Y
 $+336105.821-35.5441878*T-20.115*T*LN(T)+.00118285*T^{**2}$
 $-2.18138333E-07*T^{**3}-1572935*T^{**(-1)}$; 3.00000E+03 Y
 $+390707.537-303.115733*T+14.175*T*LN(T)-.0079804*T^{**2}$
 $+2.27558333E-07*T^{**3}-16772955*T^{**(-1)}$; 5.30000E+03 Y
 $+110975.664+452.719908*T-75.18201*T*LN(T)+.004605*T^{**2}$
 $-1.02516667E-07*T^{**3}+1.4589055E+08*T^{**(-1)}$; 8.40000E+03 Y
 $+918206.507-898.443069*T+75.05701*T*LN(T)-.0078504*T^{**2}$
 $+9.14616667E-08*T^{**3}-6.694665E+08*T^{**(-1)}$; 1.00000E+04 N
ent-sym fun F8249T 2.98150E+02 +298450.288+14.9263009*T-37.118*T*LN(T)
 $-2.52E-04*T^{**2}-4.76616667E-08*T^{**3}+69775*T^{**(-1)}$; 1.70000E+03 Y
 $+302943.477+4.41293792*T-36.086*T*LN(T)+4.1855E-04*T^{**2}$
 $-1.70581667E-07*T^{**3}-1637630*T^{**(-1)}$; 4.00000E+03 Y
 $+569254.092-858.223022*T+68.561*T*LN(T)-.0179964*T^{**2}$
 $+4.40853333E-07*T^{**3}-1.298339E+08*T^{**(-1)}$; 6.00000E+03 N
ent-sym fun F8299T 2.98150E+02 +462958.167+11.1478222*T-37.642*T*LN(T)
 $-1.1515E-04*T^{**2}-6.7015E-08*T^{**3}+51145*T^{**(-1)}$; 3.50000E+03 Y
 $+692156.122-643.599384*T+40.105*T*LN(T)-.01109485*T^{**2}$
 $+1.90893333E-07*T^{**3}-1.2151985E+08*T^{**(-1)}$; 5.50000E+03 Y
 $+1198333.43-1966.90368*T+195.893*T*LN(T)-.03229355*T^{**2}$
 $+7.29055E-07*T^{**3}-4.2822925E+08*T^{**(-1)}$; 6.00000E+03 N

@@ Copper functions (Dinsdale 1991)

ent-sym fun GHSERCU 2.98150E+02 -7770.458+130.485235*T-
24.112392*T*LN(T)
 $-.00265684*T^{**2}+1.29223E-07*T^{**3}+52478*T^{**(-1)}$; 1.35800E+03 Y

$-13542.026+183.803828*T-31.38*T*LN(T)+3.64167E+29*T**(-9);$
 3.20000E+03 N
 ent-sym fun GCUBCC 298.15 +4017.00-1.255*T+GHSERCU;
 6000 N
 ent-sym fun GCULIQ 298.15 +12964.735-9.511904*T
 $-5.849E-21*T**7 +GHSERCU; 1358 Y$
 $+13495.481-9.922344*T-3.64167E+29*T**(-9)+GHSERCU; 3200 N$

@@ copper oxide functions (Schramm)

ent-sym fun GCUCUO 298.15 -114945+307.98*T-67.71*T*LN(T); 6000 N
 ent-sym fun GCUCUO2 298.15 +1.333333*GCUCUO+16236-20*T; 6000 N
 ent-sym fun GCUCUO3 298.15 +1.666667*GCUCUO-33972.668
 $+25.917348*T; 6000 N$

@@ user functions

ent-sym fun GUSRCUO 2.98150E+02 -178002.39+275.159239*T
 $-44.965711*T*LN(T)-.010809208*T**2+1369987.3*T**(-1); 6.00000E+03 N$
 ent-sym fun GUSRCU2O 2.98150E+02 -193230+360.057*T-66.26*T*LN(T)
 $-.00796*T**2+374000*T**(-1); 6.00000E+03 N$
 ent-sym fun GN 2.98150E+02 +2*GUSRCUO+V1+V2*T; 6.00000E+03 N
 ent-sym fun GNB 2.98150E+02 +GUSRCU2O+V3+V4*T; 6.00000E+03 N
 ent-sym fun GREF 2.98150E+02 +GUSRCU2O+3*GHSEROO+v20; 6.00000E+03 N

@@ not assessed so far

ent-sym f UN_ASS 298.15 +0; 300 N

 ent-sym f GREFC 298.15 +GCEO2-2*GHSEROO+100000; 6000 N

ent-sym f GNC 298.15 +0.5*GCE2O3-5000-10.057*T-10*T; 6000 N

@@ *****Model descriptions of
phases*****

@@ Gas phases

ent-phase GAS G, 1

CE,CEO,CU,CUO,CU,CU2,O,O2,O3 ; N N

ent-param G(GAS,CE;0) 298.15 +F5574T+RTLNP; 6000 N

ent-param G(GAS,CEO;0) 298.15 +F5626T+RTLNP; 6000 N

ent-param G(GAS,CU;0) 2.98150E+02 +F8167T +R *T*LN(1E-05*P);
6.00000E+03 N

ent-param G(GAS,CUO;0) 2.98150E+02 +F8249T +R *T*LN(1E-05*P);
6.00000E+03 N

ent-param G(GAS,CU2;0) 2.98150E+02 +F8299T +R *T*LN(1E-05*P);
6.00000E+03 N

ent-param G(GAS,O;0) 298.15 +F12657T+RTLNP; 6000 N

ent-param G(GAS,O2;0) 298.15 +F12999T+RTLNP; 6000 N

ent-param G(GAS,O3;0) 298.15 +F13287T+RTLNP; 6000 N

ent-phase O2GAS , 1

O2 ; N N

ent-param G(O2GAS,O2;0) 298.15 +2*GHSEROO+RTLNP; 6000 N

@ @ Liquid phases

ent-phase IONIC_LIQ Y,

CE+3,CE+4,CU+1,CU+2,CU+3 ; O-2,VA ; N N

AMEND-PHASE ION COMP 2,,,,,,,,,

ent-param G(ION,CU+1:VA;0) 298.15 +GCULIQ;,,,

ent-param G(ION,CU+2:VA;0) 298.15 +3*GCULIQ+GCUCUO2
-2*GCUCUO;,,,

ent-param G(ION,CU+3:VA;0) 298.15 +6*GCULIQ+0.5*GCUCUO2
+GCUCUO3-4*GCUCUO;,,,

ent-param G(ION,CU+1:O-2;0) 298.15 +GCUCUO;,,,

ent-param G(ION,CU+2:O-2;0) 298.15 +GCUCUO2;,,,

ent-param G(ION,CU+3:O-2;0) 298.15 +GCUCUO3;,,,

ent-param G(ION,CU+1:O-2,VA;0) 298.15 +13287+11.82*T;,,,

ent-param G(ION,CU+1:O-2,VA;1) 298.15 -17125+11.52*T;,,,

ent-param G(ION,CU+1:O-2,VA;2) 298.15 +21762-10.15*T;,,,

ent-param G(ION,CU+1,CU+2:O-2;0) 298.15 -106048+70*T;,,,

ent-param G(IONIC_LIQ,CE+3:O-2;0) 298.15 +GCE2O3LQ; 6000 N

ent-param G(IONIC_LIQ,CE+4:O-2;0) 298.15 +2*GCEO2LQ; 6000 N

ent-param G(IONIC_LIQ,CE+3:VA;0) 298.15 +GLIQCE; 6000 N

ent-param G(IONIC_LIQ,CE+4:VA;0) 298.15 +2*GLIQCE+3*GCEO2LQ
-2*GCE2O3LQ; 6000 N

ent-param G(IONIC_LIQ,CE+3,CE+4:O-2;0) 298.15 -105398; 6000 N

ent-param G(IONIC_LIQ,CE+3,CE+4:O-2;1) 298.15 -35158; 6000 N

ent-param G(IONIC_LIQ,CE+3:O-2,VA;0) 298.15 +114250; 6000 N

@@ Metallic liquid

ent-phase met_liq , 1 1

CE,CU ; N N

ent-param G(met_liq,CE;0) 298.15 +GLIQCE; 6000 N

ent-param G(met_liq,CU;0) 298.15 +GCULIQ; 6000 N

ent-param G(met_liq,CE,CU;0) 298.15 -44488-0.398*T; 6000 N

ent-param G(met_liq,CE,CU;1) 298.15 +34088-6.247*T; 6000 N

ent-param G(met_liq,CE,CU;2) 298.15 -20951+10.387*T; 6000 N

@@ Alloy phases

ent-phase BCC_A2 , 2 1 1

CE ; O,VA ; N N

ent-param G(BCC_A2,CE:O;0) 298.15 -521242+67.7626*T

+GBCCCE+GHSEROO; 6000 N

ent-param G(BCC_A2,CE:VA;0) 298.15 +GBCCCE; 6000 N

ent-param L(BCC_A2,CE,CU:VA;0) 2.98150E+02 -8545; 6.00000E+03 N

ent-phase FCC_A1 , 2 1 1

CE,CU,O ; O,VA ; N N

ent-param G(FCC_A1,CE:O;0) 298.15 -525009+67.7626*T

+GHSERCCE+GHSEROO; 6000 N

ent-param G(FCC_A1,CE:VA;0) 298.15 +GHSERCE; 6000 N

ent-param G(FCC_A1,CU:VA;0) 2.98150E+02 +GHSERCU ; 3.20000E+03 N

ent-param G(FCC_A1,O:VA;0) 2.98150E+02 +1000000+GHSEROO ;
6.00000E+03 N

ent-param L(FCC_A1,CU,O:VA;0) 2.98150E+02 -1017730+29.6*T; 6.00000E+03
N

ent-param G(FCC_A1,CU:O;0) 2.98150E+02 +1000000+GHSERCU
+GHSEROO ; 3.20000E+03 N

ent-param G(FCC_A1,O:O;0) 2.98150E+02 +1000000+2*GHSEROO ;
6.00000E+03 N

ent-param L(FCC_A1,CE,CU:VA;0) 2.98150E+02 -13500; 6.00000E+03 N

ent-phase CU6CE , 2 0.857 0.143

CU ; CE ; N N

ent-param G(CU6CE,CU:CE;0) 298.15 -8964-2.05*T
+0.857*GHSERCU+0.143*GHSERCE; 6000 N

@@ solid oxides

@@ Ce-O (Zinkevich)

ent-phase M11O20 , 2 11 20

CE ; O ; N N

ent-param G(M11O20,CE:O;0) 298.15 +7*GCEO2+2*GCE2O3F-121419
-40.45*T; 6000 N

ent-phase M19O34 , 2 19 34
CE ; O ; N N

ent-param G(M19O34,CE:O;0) 298.15 +11*GCEO2+4*GCE2O3F-247150
-71*T; 6000 N

ent-phase M2O3A I, 3 2 2 1
CE+2,CE+3 ; O-2 ; O-2,VA ; N N

ent-param G(M2O3A,CE+2:O-2:O-2;0) 298.15 +2*GCEO+GHSEROO; 6000 N

ent-param G(M2O3A,CE+3:O-2:O-2;0) 298.15 +GCE2O3; 6000 N

ent-param G(M2O3A,CE+2:O-2:VA;0) 298.15 +2*GCEO; 6000 N

ent-param G(M2O3A,CE+3:O-2:VA;0) 298.15 +GCE2O3-GHSEROO; 6000 N

ent-param G(M2O3A,CE+2,CE+3:O-2:*;0) 298.15 +102206; 6000 N

ent-phase M2O3C I, 3 2 3 1
CE+3,CE+4 ; O-2 ; O-2,VA ; N N

ent-param G(M2O3C,CE+3:O-2:O-2;0) 298.15 +GCE2O3C+GHSEROO; 6000 N

ent-param G(M2O3C,CE+4:O-2:O-2;0) 298.15 +2*GCEO2C; 6000 N

ent-param G(M2O3C,CE+3:O-2:VA;0) 298.15 +GCE2O3C; 6000 N

ent-param G(M2O3C,CE+4:O-2:VA;0) 298.15 +2*GCEO2C-GHSEROO; 6000 N

ent-param G(M2O3C,CE+3,CE+4:O-2:*;0) 298.15 -7178-17.7264*T; 6000 N

ent-param G(M2O3C,CE+3,CE+4:O-2:*;1) 298.15 -25591+22.2801*T; 6000 N

ent-phase M2O3H I, 3 2 2 1

CE+2,CE+3 ; O-2 ; O-2,VA ; N N

ent-param G(M2O3H,CE+2:O-2:O-2;0) 298.15 +2*GCEO+GHSEROO; 6000 N

ent-param G(M2O3H,CE+3:O-2:O-2;0) 298.15 +GCE2O3H; 6000 N

ent-param G(M2O3H,CE+2:O-2:VA;0) 298.15 +2*GCEO; 6000 N

ent-param G(M2O3H,CE+3:O-2:VA;0) 298.15 +GCE2O3H-GHSEROO; 6000 N

ent-param G(M2O3H,CE+2,CE+3:O-2:*;0) 298.15 +102206; 6000 N

ent-phase M2O3X I, 3 2 2 1

CE+2,CE+3 ; O-2 ; O-2,VA ; N N

ent-param G(M2O3X,CE+2:O-2:O-2;0) 298.15 +2*GCEO+GHSEROO; 6000 N

ent-param G(M2O3X,CE+3:O-2:O-2;0) 298.15 +GCE2O3X; 6000 N

ent-param G(M2O3X,CE+2:O-2:VA;0) 298.15 +2*GCEO; 6000 N

ent-param G(M2O3X,CE+3:O-2:VA;0) 298.15 +GCE2O3X-GHSEROO; 6000 N

ent-param G(M2O3X,CE+2,CE+3:O-2:*;0) 298.15 +102206; 6000 N

ent-phase M40O72 , 2 40 72

CE ; O ; N N

ent-param G(M40O72,CE:O;0) 298.15 +24*GCEO2+8*GCE2O3F-488650

-155*T; 6000 N

ent-phase M62O112 , 2 62 112

CE ; O ; N N

ent-param G(M62O112,CE:O;0) 298.15 +38*GCEO2+12*GCE2O3F-730900
-237.3*T; 6000 N

ent-phase M7O12 , 2 7 12

CE ; O ; N N

ent-param G(M7O12,CE:O;0) 298.15 +3*GCEO2+2*GCE2O3F-133719
-11.0961*T; 6000 N

ent-phase M9O16 , 2 9 16

CE ; O ; N N

ent-param G(M9O16,CE:O;0) 298.15 +5*GCEO2+2*GCE2O3F-125351
-31.333*T; 6000 N

@@ Cu-O (Schramm)

ent-phase CU2O , 2 2 1

CE+3,CU+1,VA ; O-2 ; N N

ent-param G(CU2O,CU+1:O-2;0) 2.98150E+02 GUSRCU2O; 6.00000E+03 N

ent-param G(CU2O,CE+3:O-2;0) 2.98150E+02 GUSRCU2O-500000;
6.00000E+03 N

ent-param G(CU2O,VA:O-2;0) 2.98150E+02 GHSEROO+50000; 6.00000E+03
N

ent-param L(CU2O,CE+3,CU+1:O-2;0) 2.98150E+02 -1050000; 6.00000E+03 N

ent-param L(CU2O,CE+3,VA:O-2;0) 2.98150E+02 -600000; 6.00000E+03 N

ent-param L(CU2O,CE+3,CU+1,VA:O-2;0) 2.98150E+02 -600000; 6.00000E+03
N

ent-phase CUO , 2 1 1

CE+3,CU+2,VA ; O-2 ; N N

ent-param G(CUO,CU+2:O-2;0) 2.98150E+02 -178002.39+275.159239*T
-44.965711*T*LN(T)-.010809208*T**2+1369987.3*T**(-1); 6.00000E+03 N

ent-param G(CUO,CE+3:O-2;0) 2.98150E+02 -178002.39+275.159239*T
-44.965711*T*LN(T)-.010809208*T**2+1369987.3*T**(-1)+v30; 6.00000E+03 N

ent-param L(CUO,CE+3,VA:O-2;0) 2.98150E+02 +v31; 6.00000E+03 N

ent-param L(CUO,CE+3,CU+2:O-2;0) 2.98150E+02 +v32; 6.00000E+03 N

ent-param G(CUO,VA:O-2;0) 2.98150E+02 +GHSEROO+50000; 6.00000E+03
N

@@ Fluorite phase (Zinkevich, Ce-O) including metastable binary Cu-O

@@ and ternary extension (McInnes&Povoden-Karadeniz)

ent-phase FLUORITE I, 2 2 4

CE+3,CE+4,CU+2,CU+1 ; O-2,VA ; N N

ent-param G(FLUORITE,CE+3:O-2;0) 2.98150E+02 2*GNC-0.166666*GREFC
+0.1666*GCEO2; 6.00000E+03 N

ent-param G(FLUORITE,CE+4:O-2;0) 2.98150E+02 +2*GCEO2; 6.00000E+03
N

ent-param G(FLUORITE,CE+3:VA;0) 2.98150E+02 2*GNC+1.5*GREFC
-1.5*GCEO2; 6.00000E+03 N

ent-param G(FLUORITE,CE+4:VA;0) 2.98150E+02 2*GREFC;
6.00000E+03 N

ent-param G(FLUORITE,CE+3,CE+4:*;0) 2.98150E+02 -150000+15*T;
6.00000E+03 N

ent-param G(FLUORITE,CE+3,CE+4:*;1) 2.98150E+02 +100000-50*T;
6.00000E+03 N

ent-param G(FLUORITE,CU+2:O-2;0) 298.15 GN-0.66667*GNB+0.66667*GREF;,,,

ent-param G(FLUORITE,CU+2:VA;0) 298.15 GN+0.66667*GNB-
0.66667*GREF;,,,

ent-param G(FLUORITE,CU+1:O-2;0) 298.15 GREF;,,,

ent-param G(FLUORITE,CU+1:VA;0) 298.15 1.33333*GNB-0.33333*GREF;,,,

ent-param G(FLUORITE,CE+4,CU+2:O-2;0) 298.15 v5+v6*T; 6000 N

ent-param G(FLUORITE,CE+4,CU+1:O-2;0) 298.15 v7+v60*T; 6000 N

ent-param G(FLUORITE,CE+4,CU+2:VA;0) 298.15 v8+v9*T; 6000 N

ent-param G(FLUORITE,CE+4,CU+1:VA;0) 298.15 v10; 6000 N

ent-param G(FLUORITE,CE+3,CU+1:VA;0) 298.15 -25000; 6000 N

ent-param G(FLUORITE,CE+3,CU+1:O-2;0) 298.15 -25000; 6000 N

ent-param G(FLUORITE,CE+3,CU+2:VA;0) 298.15 -25000; 6000 N

ent-param G(FLUORITE,CE+3,CU+2:O-2;0) 298.15 -25000; 6000 N

go parrot

@@ move "set-fix" lines here

s-o-v 1 +100000

s-f-v 2 +5

s-f-v 3 +70000

s-f-v 4 +5

s-f-v 5 -80000

s-f-v 6 30

s-f-v 7 -80000

s-f-v 8 -50000

s-f-v 9 0.0001

s-f-v 10 +1e-8

s-f-v 20 +85000

s-f-v 30 -300000

s-f-v 31 -300000

s-f-v 32 -730000

s-f-v 60 30

create work

set-interactive

Appendix B: Optimized unit cell information

All unit cell information is in VASP POSCAR format

Unit cell information for copper doped ceria project:

CeO₂ unit cell: Energy = -129.0 eV

```
1.0000000000000000
 5.3938885070263893 0.0000000000000000 0.0000000000000000
 0.0000000000000000 5.3938885070263893 0.0000000000000000
 0.0000000000000000 0.0000000000000000 5.3938885070263893
Ce O
 4 8
Selective dynamics
Direct
0.7500000000000000 0.7500000000000000 0.2500000000000000 T T T
0.7500000000000000 0.2500000000000000 0.7500000000000000 T T T
0.2500000000000000 0.7500000000000000 0.7500000000000000 T T T
0.2500000000000000 0.2500000000000000 0.2500000000000000 T T T
0.0000000000000000 0.5000000000000000 0.0000000000000000 T T T
0.5000000000000000 0.5000000000000000 0.0000000000000000 T T T
0.5000000000000000 0.0000000000000000 0.5000000000000000 T T T
0.0000000000000000 0.0000000000000000 0.0000000000000000 T T T
0.0000000000000000 0.5000000000000000 0.5000000000000000 T T T
0.5000000000000000 0.5000000000000000 0.5000000000000000 T T T
0.5000000000000000 0.0000000000000000 0.0000000000000000 T T T
0.0000000000000000 0.0000000000000000 0.5000000000000000 T T T
```

Cu¹⁺ neutral structure: Energy = -31.8 eV

```
1.0000000000000000
 4.2666333605828832 0.0000000000000000 0.0000000000000000
 0.0000000000000000 4.2666333605828832 0.0000000000000000
 0.0000000000000000 0.0000000000000000 4.2666333605828832
Cu O
 4 2
Selective dynamics
Direct
0.7499999995365130 0.7499999995365130 0.2500000004634870 T T T
0.7499999995365130 0.2500000004634870 0.7499999995365130 T T T
0.2500000004634870 0.7499999995365130 0.7499999995365130 T T T
0.2500000004634870 0.2500000004634870 0.2500000004634870 T T T
0.0000000000000000 0.0000000000000000 0.0000000000000000 T T T
0.4999999990730259 0.4999999990730259 0.4999999990730259 T T T
```

Cu²⁺ neutral structure: Energy = -45.4 eV

```
1.0000000000000000
 4.5376088276054567 0.0000000000000000 0.0000000000000000
 0.0000000000000000 4.5376088276054567 0.0000000000000000
 0.0000000000000000 0.0000000000000000 4.5376088276054567
Cu O
 4 4
Selective dynamics
Direct
0.7499999995365130 0.7499999995365130 0.2500000004634870 T T T
0.7499999995365130 0.2500000004634870 0.7499999995365130 T T T
0.2500000004634870 0.7499999995365130 0.7499999995365130 T T T
```

0.2500000004634870	0.2500000004634870	0.2500000004634870	T	T	T
0.0000000000000000	0.499999990730259	0.0000000000000000	T	T	T
0.499999990730259	0.499999990730259	0.499999990730259	T	T	T
0.499999990730259	0.0000000000000000	0.0000000000000000	T	T	T
0.0000000000000000	0.0000000000000000	0.499999990730259	T	T	T

Cu³⁺ neutral structure: Energy = -57.13 eV

1.0000000000000000					
4.6807146163280811	0.0000000000000000	0.0000000000000000			
0.0000000000000000	4.6807146163280811	0.0000000000000000			
0.0000000000000000	0.0000000000000000	4.6807146163280811			

Cu O
4 6

Selective dynamics
Direct

0.749999995365130	0.749999995365130	0.250000004634870	T	T	T
0.749999995365130	0.250000004634870	0.749999995365130	T	T	T
0.250000004634870	0.749999995365130	0.749999995365130	T	T	T
0.250000004634870	0.250000004634870	0.250000004634870	T	T	T
0.0000000000000000	0.499999990730259	0.0000000000000000	T	T	T
0.499999990730259	0.499999990730259	0.0000000000000000	T	T	T
0.499999990730259	0.0000000000000000	0.499999990730259	T	T	T
0.0000000000000000	0.499999990730259	0.499999990730259	T	T	T
0.499999990730259	0.0000000000000000	0.0000000000000000	T	T	T
0.0000000000000000	0.0000000000000000	0.499999990730259	T	T	T

25% Cu²⁺ doped ceria: Energy= -84.4 eV

1.0000000000000000					
5.3496091926442988	0.0000000000000000	0.0000000000000000			
0.0000000000000000	5.3496091926442988	0.0000000000000000			
0.0000000000000000	0.0000000000000000	5.3496091926442988			

Ce Cu O
3 1 7

Selective dynamics
Direct

0.749999995365130	0.749999995365130	0.250000004634870	T	T	T
0.749999995365130	0.250000004634870	0.749999995365130	T	T	T
0.250000004634870	0.749999995365130	0.749999995365130	T	T	T
0.250000004634870	0.250000004634870	0.250000004634870	T	T	T
0.499999990730259	0.499999990730259	0.0000000000000000	T	T	T
0.499999990730259	0.0000000000000000	0.499999990730259	T	T	T
0.0000000000000000	0.0000000000000000	0.0000000000000000	T	T	T
0.0000000000000000	0.499999990730259	0.499999990730259	T	T	T
0.499999990730259	0.499999990730259	0.499999990730259	T	T	T
0.499999990730259	0.0000000000000000	0.0000000000000000	T	T	T
0.0000000000000000	0.0000000000000000	0.499999990730259	T	T	T

50% Cu²⁺ doped ceria: Energy= -66.4 eV

1.0000000000000000					
5.2041046567110181	0.0000000000000000	0.0000000000000000			
0.0000000000000000	5.2041046567110181	0.0000000000000000			
0.0000000000000000	0.0000000000000000	5.2041046567110181			

Ce Cu O
2 2 6

Selective dynamics
Direct

0.749999995365130	0.749999995365130	0.250000004634870	T	T	T
0.250000004634870	0.749999995365130	0.749999995365130	T	T	T
0.749999995365130	0.250000004634870	0.749999995365130	T	T	T
0.250000004634870	0.250000004634870	0.250000004634870	T	T	T

0.4999999990730259	0.4999999990730259	0.0000000000000000	T	T	T
0.0000000000000000	0.0000000000000000	0.0000000000000000	T	T	T
0.0000000000000000	0.4999999990730259	0.4999999990730259	T	T	T
0.4999999990730259	0.4999999990730259	0.4999999990730259	T	T	T
0.4999999990730259	0.0000000000000000	0.0000000000000000	T	T	T
0.0000000000000000	0.0000000000000000	0.4999999990730259	T	T	T

75% Cu²⁺ doped ceria: Energy= -50.55 eV

1.0000000000000000					
4.9466879734765676	0.0000000000000000	0.0000000000000000			
0.0000000000000000	4.9466879734765676	0.0000000000000000			
0.0000000000000000	0.0000000000000000	4.9466879734765676			
Cu	Ce	O			
3	1	5			

Selective dynamics
Direct

0.7499999995365130	0.7499999995365130	0.2500000004634870	T	T	T
0.7499999995365130	0.2500000004634870	0.7499999995365130	T	T	T
0.2500000004634870	0.2500000004634870	0.2500000004634870	T	T	T
0.2500000004634870	0.7499999995365130	0.7499999995365130	T	T	T
0.0000000000000000	0.4999999990730259	0.0000000000000000	T	T	T
0.4999999990730259	0.0000000000000000	0.4999999990730259	T	T	T
0.0000000000000000	0.4999999990730259	0.4999999990730259	T	T	T
0.4999999990730259	0.4999999990730259	0.4999999990730259	T	T	T
0.4999999990730259	0.0000000000000000	0.0000000000000000	T	T	T

25 % Cu¹⁺ doped ceria: Energy= -114.5 eV

1.0000000000000000					
10.0822772312408997	0.0000000000000000	0.0000000000000000			
0.0000000000000000	5.0411386156204498	0.0000000000000000			
0.0000000000000000	0.0000000000000000	5.0411386156204498			
Ce	Cu	O			
6	2	13			

Selective dynamics
Direct

0.3750000000000000	0.7500000000000000	0.2500000000000000	T	T	T
0.3750000000000000	0.2500000000000000	0.7500000000000000	T	T	T
0.1250000000000000	0.7500000000000000	0.7500000000000000	T	T	T
0.8750000000000000	0.7500000000000000	0.2500000000000000	T	T	T
0.8750000000000000	0.2500000000000000	0.7500000000000000	T	T	T
0.6250000000000000	0.7500000000000000	0.7500000000000000	T	T	T
0.1250000000000000	0.2500000000000000	0.2500000000000000	T	T	T
0.6250000000000000	0.2500000000000000	0.2500000000000000	T	T	T
0.0000000000000000	0.499999989988666	0.0000000000000000	T	T	T
0.2500000000000000	0.499999989988666	0.0000000000000000	T	T	T
0.2500000000000000	0.0000000000000000	0.499999989988666	T	T	T
0.0000000000000000	0.499999989988666	0.499999989988666	T	T	T
0.2500000000000000	0.499999989988666	0.499999989988666	T	T	T
0.2500000000000000	0.0000000000000000	0.0000000000000000	T	T	T
0.0000000000000000	0.0000000000000000	0.499999989988666	T	T	T
0.7500000000000000	0.499999989988666	0.0000000000000000	T	T	T
0.7500000000000000	0.0000000000000000	0.499999989988666	T	T	T
0.5000000000000000	0.0000000000000000	0.0000000000000000	T	T	T
0.5000000000000000	0.499999989988666	0.499999989988666	T	T	T
0.7500000000000000	0.499999989988666	0.499999989988666	T	T	T
0.7500000000000000	0.0000000000000000	0.0000000000000000	T	T	T

50 % Cu¹⁺ doped ceria: Energy= -59.8 eV

1.0000000000000000					
5.1499237382700844	0.0000000000000000	0.0000000000000000			
0.0000000000000000	5.1499237382700844	0.0000000000000000			
0.0000000000000000	0.0000000000000000	5.1499237382700844			
Cu	Ce	O			

```

      2      2      5
Selective dynamics
Direct
0.7499999995365130 0.7499999995365130 0.2500000004634870 T T T
0.2500000004634870 0.2500000004634870 0.2500000004634870 T T T
0.7499999995365130 0.2500000004634870 0.7499999995365130 T T T
0.2500000004634870 0.7499999995365130 0.7499999995365130 T T T
0.4999999990730259 0.4999999990730259 0.0000000000000000 T T T
0.0000000000000000 0.4999999990730259 0.4999999990730259 T T T
0.4999999990730259 0.4999999990730259 0.4999999990730259 T T T
0.4999999990730259 0.0000000000000000 0.0000000000000000 T T T
0.0000000000000000 0.0000000000000000 0.4999999990730259 T T T

```

Unit cell information for Ge₅O(PO₄)₆ project:

Structure I: Energy= -157.0 eV

```

1.0000000000000000
7.9939999999999998 0.0000000000000000 0.0000000000000000
-3.9969999999999999 6.9230070799999996 0.0000000000000000
0.0000000000000000 0.0000000000000000 24.8700000000000010
Ge P O
15 18 75
Selective dynamics
Direct
0.0000000000000000 0.0000000000000000 0.0000000000000000 T T T
0.0000000000000000 0.0000000000000000 0.1752412654646361 T T T
0.0000000000000000 0.0000000000000000 0.4311560294842887 T T T
0.6666666661851792 0.3333333323703584 0.3333333329312396 T T T
0.6666666661851792 0.3333333323703584 0.5085745987979647 T T T
0.6666666661851792 0.3333333323703584 0.7644893624155353 T T T
0.0000000000000000 0.0000000000000000 0.8247587345353639 T T T
0.0000000000000000 0.0000000000000000 0.5688439705157113 T T T
0.6666666661851792 0.3333333323703584 0.1580920674666106 T T T
0.6666666661851792 0.3333333323703584 0.9021773034469509 T T T
0.3333333330925896 0.6666666661851792 0.4914254012020353 T T T
0.3333333330925896 0.6666666661851792 0.2355106375844647 T T T
0.3333333330925896 0.6666666661851792 0.6666666670687604 T T T
0.3333333330925896 0.6666666661851792 0.8419079325333895 T T T
0.3333333330925896 0.6666666661851792 0.0978226965530491 T T T
0.2928284661764649 0.2683198169843938 0.0906550762048452 T T T
0.6261617999912857 0.9349864846140282 0.7573217432736057 T T T
0.9594951343348143 0.6016531507992146 0.4239884091360919 T T T
0.7316801825823528 0.0245086492132240 0.0906550762048452 T T T
0.0650135156749424 0.6911753153984032 0.7573217432736057 T T T
0.3983468500184709 0.3578419815835895 0.4239884091360919 T T T
0.0245086500097566 0.2928284661976178 0.9093449237951547 T T T
0.3578419825736385 0.9594951338272594 0.5760115908639081 T T T
0.6911753161949358 0.6261617985679763 0.2426782567263944 T T T
0.7071715338235350 0.7316801830156062 0.9093449237951547 T T T
0.0405048656651858 0.3983468492007854 0.5760115908639081 T T T
0.3738382000087143 0.0650135153859718 0.2426782567263944 T T T
0.2683198174176472 0.9754913507867761 0.9093449237951547 T T T
0.6016531499815291 0.6421580184164105 0.5760115908639081 T T T
0.9349864843325076 0.3088246846015968 0.2426782567263944 T T T
0.9754913499902435 0.7071715338023822 0.0906550762048452 T T T
0.3088246830828330 0.3738381999875615 0.7573217432736057 T T T
0.6421580174263616 0.0405048661727407 0.4239884091360919 T T T
0.1319799246693760 0.2272248536386692 0.1319795772243166 T T T
0.2251277475227088 0.1415189958123119 0.0406374023157640 T T T
0.3753460182529672 0.4857196379982550 0.0717044334818688 T T T
0.4522964233480758 0.2400883429155863 0.1139157458262167 T T T
0.3333333330925896 0.6666666661851792 0.1666666670687604 T T T
0.4653132565110267 0.8938915198238484 0.7986462442930699 T T T
0.5584610813375295 0.8081856634419535 0.7073040693845244 T T T
0.7086793520677881 0.1523863056278894 0.7383711001485331 T T T
0.7856297564406726 0.9067550091007656 0.7805824128949700 T T T
0.7986465908545552 0.5605581860090347 0.4653129101555562 T T T
0.8917944144301191 0.4748523296271327 0.3739707352470106 T T T
0.0420126864113165 0.8190529718130757 0.4050377664131084 T T T
0.1189630895332622 0.5734216752859448 0.4472490791595453 T T T
0.7727751473865090 0.9047550715067918 0.1319795772243166 T T T

```

0.8584810048131077	0.0836087527743777	0.0406374023157640	T	T	T
0.5142803606017343	0.8896263799669993	0.0717044334818688	T	T	T
0.7599116580250586	0.2122080807013660	0.1139157458262167	T	T	T
0.1061084792281597	0.5714217376919710	0.7986462442930699	T	T	T
0.1918143366547585	0.7502754189595570	0.7073040693845244	T	T	T
0.8476136944165551	0.5562930475966409	0.7383711001485331	T	T	T
0.0932449911176552	0.8788747468865452	0.7805824128949700	T	T	T
0.4394418135716882	0.2380884038771502	0.4653129101555562	T	T	T
0.5251476709982870	0.4169420851447361	0.3739707352470106	T	T	T
0.1809470267869135	0.2229597123373649	0.4050377664131084	T	T	T
0.4265783242102448	0.5455414130717244	0.4472490791595453	T	T	T
0.9047550700827149	0.1319799237009986	0.8680204227756835	T	T	T
0.0836087510848776	0.2251277485866968	0.9593625976842360	T	T	T
0.8896263808278716	0.3753460194097166	0.9282955665181312	T	T	T
0.2122080806509103	0.4522964221724900	0.8860842541737833	T	T	T
0.2380884031753046	0.7986465898861779	0.5346870898444439	T	T	T
0.4169420841774672	0.8917944147718759	0.6260292647529894	T	T	T
0.2229597139204612	0.0420126855948958	0.5949622335868916	T	T	T
0.66666666661851792	0.3333333323703584	0.8333333329312396	T	T	T
0.5714217375188331	0.4653132560713642	0.2013537557069301	T	T	T
0.7502754185209958	0.5584610809570552	0.2926959306154756	T	T	T
0.5562930470130508	0.7086793517800751	0.2616288998514669	T	T	T
0.8788747468360896	0.7856297545428484	0.2194175871050300	T	T	T
0.8680200753306240	0.7727751463613308	0.8680204227756835	T	T	T
0.7748722524772913	0.8584810041876880	0.9593625976842360	T	T	T
0.6246539810248015	0.5142803605572899	0.9282955665181312	T	T	T
0.5477035766519242	0.7599116570844137	0.8860842541737833	T	T	T
0.2013534084232136	0.4394418125465100	0.5346870898444439	T	T	T
0.1082055855698809	0.5251476703728672	0.6260292647529894	T	T	T
0.9579873135886834	0.1809470281869243	0.5949622335868916	T	T	T
0.8810369104667378	0.4265783247140552	0.5527509208404547	T	T	T
0.5346867427667421	0.1061084787316893	0.2013537557069301	T	T	T
0.4415389186624705	0.1918143365580465	0.2926959306154756	T	T	T
0.2913206479322120	0.8476136943721106	0.2616288998514669	T	T	T
0.2143702435593345	0.0932449908992344	0.2194175871050300	T	T	T
0.2272248526134910	0.0952449284932082	0.8680204227756835	T	T	T
0.1415189951868922	0.9163912472256223	0.9593625976842360	T	T	T
0.4857196393982657	0.1103736200330007	0.9282955665181312	T	T	T
0.2400883419749414	0.7877919192986340	0.8860842541737833	T	T	T
0.5605581864283118	0.7619115961228498	0.5346870898444439	T	T	T
0.4748523290017130	0.5830579148552638	0.6260292647529894	T	T	T
0.8190529724908553	0.7770402862181799	0.5949622335868916	T	T	T
0.5734216757897551	0.4544585869282756	0.5527509208404547	T	T	T
0.8938915207718403	0.4285782623080290	0.2013537557069301	T	T	T
0.8081856633452416	0.2497245810404430	0.2926959306154756	T	T	T
0.1523863055834449	0.4437069524033591	0.2616288998514669	T	T	T
0.9067550088823518	0.1211252531134548	0.2194175871050300	T	T	T
0.0952449299172851	0.8680200762990014	0.1319795772243166	T	T	T
0.9163912489151224	0.7748722514133033	0.0406374023157640	T	T	T
0.1103736191721284	0.6246539805902833	0.0717044334818688	T	T	T
0.7877919193490897	0.5477035778275100	0.1139157458262167	T	T	T
0.4285782624811669	0.5346867439286358	0.7986462442930699	T	T	T
0.2497245814790042	0.4415389190429448	0.7073040693845244	T	T	T
0.4437069529869492	0.2913206482199250	0.7383711001485331	T	T	T
0.1211252531639104	0.2143702454571515	0.7805824128949700	T	T	T
0.7619115968246954	0.2013534101138221	0.4653129101555562	T	T	T
0.5830579158225327	0.1082055852281240	0.3739707352470106	T	T	T
0.7770402860795388	0.9579873144051041	0.4050377664131084	T	T	T
0.454458585342689	0.8810369101978685	0.4472490791595453	T	T	T
0.5455414137435000	0.1189630883576692	0.5527509208404547	T	T	T
0.0000000000000000	0.0000000000000000	0.5000000000000000	T	T	T

Structure 2: Energy= -503.8 eV

1.0000000000000000		
7.9939999999999998	0.0000000000000000	0.0000000000000000
-3.9969999999999999	6.9230070779000004	0.0000000000000000
0.0000000000000000	0.0000000000000000	16.5130000000000017
Ge	P	O
10	12	50

Selective dynamics

Direct

0.3333331687526631	0.6666665653454541	0.0243951597211740	T	T	T
0.6666664115361450	0.3333332569807955	0.2499999955169968	T	T	T
-0.0000003942393423	-0.0000001796152087	0.1470525886515333	T	T	T
0.3333332551148435	0.6666665698972332	0.4756048527429129	T	T	T
-0.0000001142645583	-0.000000109772704	0.3529476407984768	T	T	T
0.6666666109468782	0.3333333017564369	0.9756048575408554	T	T	T
0.3333335144736108	0.6666665013587283	0.7499999753400607	T	T	T
0.0000000945733311	0.0000000111847904	0.8529475938565851	T	T	T
0.6666665690884074	0.3333331417671377	0.5243951814718754	T	T	T
-0.0000001596392009	-0.0000003375503733	0.6470525482621542	T	T	T
0.6562360413552305	0.0448825306218813	0.3931250307385419	T	T	T
0.6562358588839183	0.6113532006729041	0.1068749392065878	T	T	T
0.9551168438714180	0.3437637743116488	0.1068749488932148	T	T	T
0.6113532824163551	0.6562359811723800	0.6068749082155201	T	T	T
0.0448827976986610	0.3886465403340755	0.6068749339132012	T	T	T
0.3437637969155818	0.9551167917909000	0.6068749745970856	T	T	T
0.6113536397636069	0.9551172131356472	0.8931250549243394	T	T	T
0.3437634854310584	0.3886462397833083	0.8931250411143248	T	T	T
0.0448827043280039	0.6562361854038623	0.8931250197339247	T	T	T
0.3886461311325548	0.3437634054273832	0.3931250773758579	T	T	T
0.9551170120105041	0.6113534626849304	0.3931250421380477	T	T	T
0.3886464698047003	0.0448828126335435	0.1068749479112010	T	T	T
0.4409977747224299	0.8890233354807849	0.0895715195911273	T	T	T
0.2007885189406157	0.7572750293405196	0.9583959112081155	T	T	T
0.6705333111188195	0.1347014407543135	0.3100471855456737	T	T	T
0.0000001238652950	-0.0000001847149901	0.2500001101619804	T	T	T
0.0692919423641915	0.2297070112955774	0.1100280599748974	T	T	T
0.4409978024083798	0.5519742966466027	0.4104284691836860	T	T	T
0.2007884775848198	0.4435132836502687	0.5416040881139959	T	T	T
0.6705334596079381	0.5358318868711714	0.1899527907561254	T	T	T
0.0692916720281248	0.8395851288579673	0.3899719460614008	T	T	T
0.1109762069289020	0.5590017930019139	0.4104284700848939	T	T	T
0.2427248635620006	0.7992108724742510	0.5416041994530048	T	T	T
0.8652982597982984	0.3294663368101198	0.1899528667653769	T	T	T
0.7702929946021865	0.9307078571729154	0.3899717890654081	T	T	T
0.5519743752226764	0.4409979521971651	0.9104284905968821	T	T	T
0.4435134368398443	0.2007886244007516	0.0416041300573459	T	T	T
0.5358323369346730	0.6705337468033211	0.6899528194132305	T	T	T
-0.0000003529410876	0.0000002144153142	0.7500000625138569	T	T	T
0.8395853238366415	0.0692918198140094	0.8899719938703828	T	T	T
0.8890233933919338	0.4480253808087216	0.9104285270100475	T	T	T
0.7572748806955237	0.5564865291354335	0.0416041072444720	T	T	T
0.1347018629851378	0.4641679542511501	0.6899527545283171	T	T	T
0.2297067716450414	0.1604145812240124	0.8899718544770421	T	T	T
0.55900193735955187	0.1109764497017387	0.9104284376341772	T	T	T
0.7992108700002311	0.2427249350218083	0.0416041810503146	T	T	T
0.3294665051741801	0.8652982435141534	0.6899528817273016	T	T	T
0.9307079797175982	0.7702930651632569	0.8899716142282290	T	T	T
0.5519745215404495	0.1109763054854673	0.5895714885194419	T	T	T
0.4435132344055261	0.2427246769164835	0.4583959691241763	T	T	T
0.5358322187855042	0.8652982778468511	0.8100471864268083	T	T	T
0.8395852202370344	0.7702925625754971	0.6100279100354165	T	T	T
0.5590019481433035	0.4480251413874985	0.5895715575781618	T	T	T
0.7992108996888135	0.5564858939540338	0.4583958614778240	T	T	T
0.3294663741166144	0.4641678063167718	0.8100471519223212	T	T	T
0.9307077368718168	0.1604146668159706	0.6100280100742129	T	T	T
0.8890232630605430	0.4409977821693064	0.5895714874049525	T	T	T
0.7572748048476939	0.2007885636820888	0.4583958548855387	T	T	T
0.1347018293808909	0.6705332746299346	0.8100472493597209	T	T	T
0.2297071394092554	0.0692919829658747	0.6100281313528041	T	T	T
0.4480250853877320	0.5590019396207597	0.0895714950049872	T	T	T
0.5564860401295413	0.7992111644089720	0.9583959034784669	T	T	T
0.4641678911314100	0.3294660899470676	0.3100472560833793	T	T	T
0.1604145942310597	0.9307077599797953	0.1100280325451880	T	T	T
0.1109763347158292	0.5519745033114842	0.0895714924530305	T	T	T
0.2427247877838890	0.4435136373134148	0.9583958458231330	T	T	T
0.8652981719274143	0.5358319433914128	0.3100471573770358	T	T	T
0.7702924080266818	0.8395850934575517	0.1100280992234458	T	T	T
0.4480252267241084	0.8890232528676664	0.4104285150296689	T	T	T
0.5564862402344317	0.7572747686676961	0.5416040969453535	T	T	T
0.4641678069733362	0.1347016679804419	0.1899528229688700	T	T	T
0.1604144735596106	0.2297067018890613	0.3899718519243053	T	T	T

